Thermal Conductivity of Nanostructure-Enhanced Phase Change Materials: Measurements for Solid Eicosane-Based Copper Oxide and Carbon Nanotube Colloids and Numerical Modeling of Anomalous Measurements near Phase Transition

by

Mahdi Nabil

A thesis submitted to the Graduate Faculty of
Auburn University
in partial fulfillment of the
requirements for the Degree of
Master of Science

Auburn, Alabama
August 3, 2013

Keywords: Phase Change Materials, Nanoparticle Colloids, Transient Plane Source Method, Thermal Conductivity Measurement, Transient Hot Wire Method, Melting

Approved by

Jay M. Khodadadi, Chair, Alumni Professor of Mechanical Engineering
Daniel K. Harris, Associate Professor of Mechanical Engineering
Roy W. Knight, Assistant Professor of Mechanical Engineering

Abstract

In this thesis, thermal conductivity of eicosane-based nanostructure-enhanced phase change materials (NePCM) and modeling of the effectiveness of the widely-used transient hot wire (THW) apparatus near the liquid-solid phase transition temperature are investigated using experimental and numerical approaches.

Eicosane ($C_{20}H_{42}$) with a melting point of 37 °C was selected as the base PCM. Multi-walled carbon nano-tubes (MWCNT) and copper (II) oxide (CuO) nanoparticles stabilized by sodium oleate acid ($C_{18}H_{33}O_2Na$) were selected as nano-scale thermal conductivity enhancers. Three distinct batches of solid eicosane-CuO samples with the same mass fraction of nanoparticles were obtained under ice-water bath, ambient temperature and oven solidification schemes. Thermal conductivity of solid NePCM composites with eight different loadings of CuO nanoparticles and a constant concentration of MWCNTs were measured experimentally at various temperatures using the transient plane source (TPS) technique. Using a controllable temperature bath, measurements were conducted at various temperatures between 10 and 35 °C for the solid samples. Thermal conductivity measurements of the composites were found to be independent of the measurement temperature for a given particle loading regardless of the solidification procedure. The ice-water bath solidification route eicosane-CuO samples consistently exhibited lowest values of thermal conductivity, whereas the samples of oven solidification scheme corresponded to the highest values. Considering eicosane-CuO samples, for mass fractions greater than 2 wt%, a non-monotonic relation between the thermal

conductivity and the mass fraction, independent of the temperature range studied, was exhibited. Although no functionalization was performed on the purchased MWCNT powders, the amount of thermal conductivity enhancement for the 0.27 wt% eicosane-MWCNTs solid samples (~25-35%) was much higher than that of the 1 wt% eicosane-CuO solid disks (~1-4%).

A 1-D transient heat conduction problem was formulated and solved over a finite cylindrical domain with and without phase transition using ANSYS® FLUENT and MATLAB. The objective was to model the behavior of a THW apparatus near the melting temperature of the medium. The defined FLUENT model was first successfully verified against an ideal mathematical transient hot wire theory for a perfect conductor with a 0.01% error for the monitored temperature values. Another benchmarking was performed against an exact solution for a similar melting problem to verify the adopted enthalpy method and the error for the monitored temperature values was less than 0.5%. Focusing on the FLUENT model, thermal conductivity predictions in both liquid and solid phases were individually performed in the absence of phase change. The difference between the extracted thermal conductivity and the initially-assigned value based on the literature was less than 1% and 0.81% for solid and liquid phases, respectively. The effect of the initial solid state temperature on the predicted thermal conductivity values under the presence of melting was explored. Five different initial temperatures were studied. The aim was to observe if any sharp rise in thermal conductivity values will occur near the melting point of the PCM. It was shown and concluded that there is no abrupt behavior as temperature approaches the melting point of PCM and all the predicted thermal conductivity values are between the assigned values of the liquid and solid states.

Acknowledgements

I would like to gratefully thank Dr. Jay M. Khodadadi, who served as my adviser, for his insightful supervision, understanding, and paternal support during the whole period of my M.Sc. studies at Auburn University. In addition, I would like to thank all of my current and previous research group members at the Fluid Mechanics Research Laboratory (FMRL), Hasan Babaei, Yousef El-Hasadi, Dr. Liwu Fan and Mahmoud Moeini Sedeh, for sharing their valuable experiences and providing a friendly and instructive research environment.

I appreciate a college/departmental fellowship award by the Samuel Ginn College of Engineering and Department of Mechanical Engineering at Auburn University that supported my research for two consecutive years.

I would also like to thank Dr. German Mills of the Department of Chemistry and Biochemistry and his current and former research group members, Dr. Dan Clary, Jason Darvin and Mohammad Sharif Hossain for providing the functionalized nano-particles, their instructions and timely assistance in the process of NePCM colloids' preparation.

I would like to thank Dr. Roy W. Knight and Dr. Daniel K. Harris of the Department of Mechanical Engineering, for serving as the committee members and also for the informative graduate courses I have taken with them during the past two years.

I am deeply grateful to my lovely family for their ever-lasting support and patience over my absence every single day.

This thesis is based upon the work partially funded by the United States Department of Energy under the Award Number DE-SC0002470. This report was prepared as an account of work sponsored by an agency of the United States Government. Neither the United States Government nor any agency thereof, nor any of their employees, makes any warranty, express or implied, or assumes any legal liability or responsibility for the accuracy, completeness, or usefulness of any information, apparatus, product, or process disclosed, or represents that its use would not infringe privately owned rights. References herein to any specific commercial product, process, or service-water by trade name, trademark, manufacturer, or otherwise does not necessarily constitute or imply its endorsement, recommendation, or favoring by the United States Government or any agency thereof. The views and opinions of authors expressed herein do not necessarily state or reflect those of the United States Government or any agency thereof.

Table of Contents

List of Tables

List of Figures

List of Abbreviations

AFM	atomic force microscopy
ALN	aluminum nitride (AlN)
CFD	computational fluid dynamics
CMC	carboxyl methyl cellulose (-CH_2-COOH)
CNF	carbon nanofibers
CNT	carbon nanotubes
DLS	dynamic light scattering
DSC	differential scanning calorimetry
DTA	differential thermal analysis
FE-SEM	field-emission scanning electron microscopy
FTIR	Fourier transform infrared spectroscopy
GNF	graphite nanofibers
GNP	graphene nanoplatelets
ITC	infrared thermal camera
LHS	latent heat storage
MG	Maxwell-Garnet model
MT	melting temperature
MWCNT	multi-walled carbon nanotubes
NePCM	nanostructure-enhanced phase change materials
NFA	nanoflash analyzer
OM	optical microscopy

PA	palmitic acid ($C_{16}H_{32}O_2$)
PCM	phase change materials
PEB	precision electronic balance
POM	polarizing optical microscopy
PSA	particle size analyzer
RM	rheometer
RTD	resistance temperature detector
RV	rotational viscometer
SAT	sodium acetate trihydrate ($CH_3COONa \cdot 3H_2O$)
SDBS	sodium dodecylbenzene sulfonate ($C_{18}H_{29}NaO_3S$)
SEM	scanning electron microscopy
SHS	sensible heat storage
SM	source meter
SOA	sodium oleate acid ($C_{18}H_{33}NaO_2$)
SWCNT	single-walled carbon nanotubes
TC	thermocouple
TEM	transmission electron microscopy
TES	thermal energy storage
TGA	thermal gravimetric analysis
TG-DTA	thermogravimetric/differential thermal analyzer
THW	transient hot wire method
TIM	thermal interface material
TPS	transient plane source method
XPS	X-ray photon spectroscopy
XRD	X-ray diffraction

List of Symbols

Nomenclature

a	radius of wire, mm
b	radius of cylindrical block, mm
C_p	specific heat, J/kgK
H	total enthalpy, J/kg
k	thermal conductivity, W/mK
L	latent heat of fusion, J/kg
q	strength of line heat source, W/m
r	radial coordinate, mm
s	position of the liquid-solid interface, mm
t	time, s
T	temperature, K or ℃

Greek Symbols

α	thermal diffusivity, m^2/s
ε_T	temperature difference, ℃
γ	Euler's constant, dimensionless
λ	parameter, introduced in Eq. (4.13), or constant of a transcendental equation
μ	dynamic viscosity, kg/ms
ρ	density, kg/m^3

Subscripts

i	initial value or index, introduced in Eq. (4.8), time-related discretized values
l	liquid
m	melting
s	solid
vol	volume fraction
w	wire
wt	weight or mass fraction

Superscripts

n	index introduced in Eq. (4.8) related to space-related discretized values

Chapter 1 Introduction

Greater push for utilization of renewable sources of energy is seriously hampered by the bottleneck of energy storage. In contributing to improved effectiveness of thermal energy storage systems, the work reported in this thesis is concerned with exploring the thermal conductivity of eicosane-based nanostructure-enhanced phase change material (NePCM). In addition, modeling of the effectiveness of a commonly-used transient hot wire (THW) apparatus for measuring thermal conductivity of materials near their liquid-solid transition point is reported. The motivation and background of the research in this thesis are discussed first. Then, the objectives and methodology are listed in an itemized fashion. At the end, a brief overview of the contents of following chapters is presented.

1.1 Motivation and Background

Realizing the negative impacts of using fossil fuels on the environment besides the unpredictable price fluctuations and limited resources, the mankind is looking for reliable and cost-effective alternative sources of energy. Despite the fact that renewable sources of energy currently provide a small portion of worldwide total energy demand, they have been found to be promising, reliable, sustainable and clean. However, effective technologies need to be adopted in order to address the unreliability of supply issue that is common to all renewable energy systems.

Thermal energy is a form of energy that is abundant in nature, e.g. solar energy, waste heat from building and industrial processes, etc. This form of energy can be stored temporarily at low or high temperatures within a medium to recover the waste heat of energy devices. Thermal energy storage (TES) can also play a key role in energy conservation and cost-effectiveness by deducting the incongruity between the rates of energy demand and supply. In this way, the performance and reliability of energy systems will be enhanced. Today, there is a wide range of applications for thermal energy storage systems from domestic water heaters and transport vehicles to electronics and spacecrafts.

There are three main strategies to store thermal energy, namely sensible, latent heat and chemical storage methods. Sensible heat storage (SHS) is a method in which thermal energy is stored by changing the temperature of the storage medium. On the other hand, thermal energy can also be stored by changing the phase of a storage material (phase change material) at a nearly constant temperature which is called the latent heat storage (LHS) method. Various chemical groups of phase change materials are classified in Figure 1.1. Solid-liquid phase change materials include both organic and inorganic substances. Organic materials are not corrosive and therefore are compatible with metal containers. They are also thermally and chemically stable. On the other hand, inorganic materials possess greater phase change enthalpy per unit volume and cover a wider temperature range. Corrosion, supercooling effect and phase separation, however, are the main disadvantage of inorganic substances. Paraffins, linear alkanes with the chemical formula C_nH_{2n+2}, are the most commercially used organic PCM. They possess high storage capacity with nearly no supercooling during phase change. In this thesis, eicosane ($C_{20}H_{42}$) which is an alkane is selected as the base PCM.

Regardless of the storage method, in order to retrieve the stored heat/cold when it is needed, the process should be reversed. The storage capacity of the LHS method compared to SHS is considerably higher in the applications in which temperature of the working instrument remains relatively constant. For example, storage of ice as a PCM in large scales for industrial and buildings cooling applications is currently common all over the world. For decades, phase change materials (PCM) have been widely recognized for their beneficial role in storing sizeable amount of thermal energy over a narrow temperature range through thawing/freezing. Latent heat of fusion per unit mass vs. the melting point of water and three main groups of PCM (paraffins, fatty acids, and salt hydrates) is presented in Figure 1.2. Water possesses the greatest latent heat of fusion per unit mass (330 J/g) and the paraffin family on average exhibit the lowest values. Furthermore, paraffins are only applicable on a modestly narrow temperature range (20~60 °C), whereas fatty acids and salt hydrates cover a wider range of melting temperatures (0~120 °C). Regardless of the latent storage capacity and operating temperature, PCM in general possess low thermal conductivity values that limit their performance during charge/discharge of thermal storage systems. Simple techniques for improvement of the thermal conductivity of PCM that involve introducing high-conductivity materials such as metallic fins, shavings, etc. have long been practiced (Fan and Khodadadi, 2011). A far more novel solution to overcome this shortcoming has been to develop nanostructure-enhanced PCM (NePCM) to improve the thermal conductivity of PCM. Utilization of nanostructures to modify the functionalities of phase change materials is a novel undertaking that has gained greater momentum in recent years. A review of work on NePCM through July 2011 has recently been published (Khodadadi, Fan and Babaei, 2013). A number of overlooked articles published from 2009 to 2011 and recent research articles (Gao et al., 2009, Ai et al., 2010, Wang et al., 2011, Hu et al., 2011, Sanusi et

al., 2011, Zheng et al., 2011, Teng et al., 2011, Bayramoglu, 2011, Kalaiselvam et al., 2012, Jesumathy et al., 2012, Mare et al., 2012, Wu et al., 2012, Kumaresan et al., 2012, Harikrishnan and Kalaiselvam, 2012, Zeng et al., 2012, He et al., 2012, Teng et al., 2013, Shi et al., 2013, Yu et al., 2013) that have studied candidate NePCM, their stability issues, thermophysical properties and heat transfer behavior are reviewed and reported in this thesis. In general, it has been concluded (Khodadadi et al., 2013) that carbon-based nanostructures (e.g. graphite and graphene) and carbon nanotubes (CNT) exhibit far greater enhancement of thermal conductivity in comparison to metallic/metal oxide nanoparticles.

1.2 Objectives and Methodology

To investigate the thermophysical properties of NePCM as candidates for application in thermal energy storage systems and to address the current shortcomings in measuring their thermal conductivity, the present thesis was aimed:

1) to prepare homogenous solid NePCM composite samples through different methods of solidification from stable NePCM colloids,

2) to design and fabricate a stable support set-up for the solid sample pairs in order to exclude the probable effects of vibration of a constant-temperature bath unit on the thermal conductivity measurements. In effect, the experiments were performed at a constant temperature of interest, and

3) to explore the possible reason(s) behind the experimental observations by many researchers, including the author, who have observed a sharp rise in thermal conductivity values as the temperature approaches the melting point of the PCM.

The adopted numerical and experimental methodologies to reach the aforementioned goals can be listed as:

1) a state-of-the-art transient plane source (TPS) apparatus to measure the thermal conductivity of NePCM composites in both liquid and solid phases, besides using a constant-temperature bath/circulator system to adjust the temperature of the samples accurately,

2) an exact method to solve the one-dimensional (1-D) heat conduction equations for melting and solidification of an infinite medium with a center-located wire heat source/sink using MATLAB coding, and

3) a 1-D transient axisymmetric computational model for a typical THW apparatus with the aid of a phase change enthalpy model using the ANSYS® FLUENT software.

1.3 Outline of the Thesis

The rest of the thesis includes four chapters. In Chapter 2, a review of recent studies on improving thermal conductivity of PCM due to introduction of different nanostructures for thermal energy storage is discussed. In Chapter 3, the effective thermal conductivity of solid composite disks made of eicosane as the base PCM plus copper oxide nanoparticles and multi-walled CNT (MWCNT) is experimentally studied using the transient plane source technique.

Adopting an exact solution, a numerical analysis is performed in Chapter 4 in order to solve the 1-D transient heat conduction equation for melting/solidification of a PCM with a center-located wire heat source/sink via MATLAB. With the aid of ANSYS® FLUENT, a 1-D transient axisymmetric model of a commonly-used THW apparatus is also formulated and solved using a phase change enthalpy model to verify the MATLAB code results. At the end, conclusions are outlined in Chapter 5.

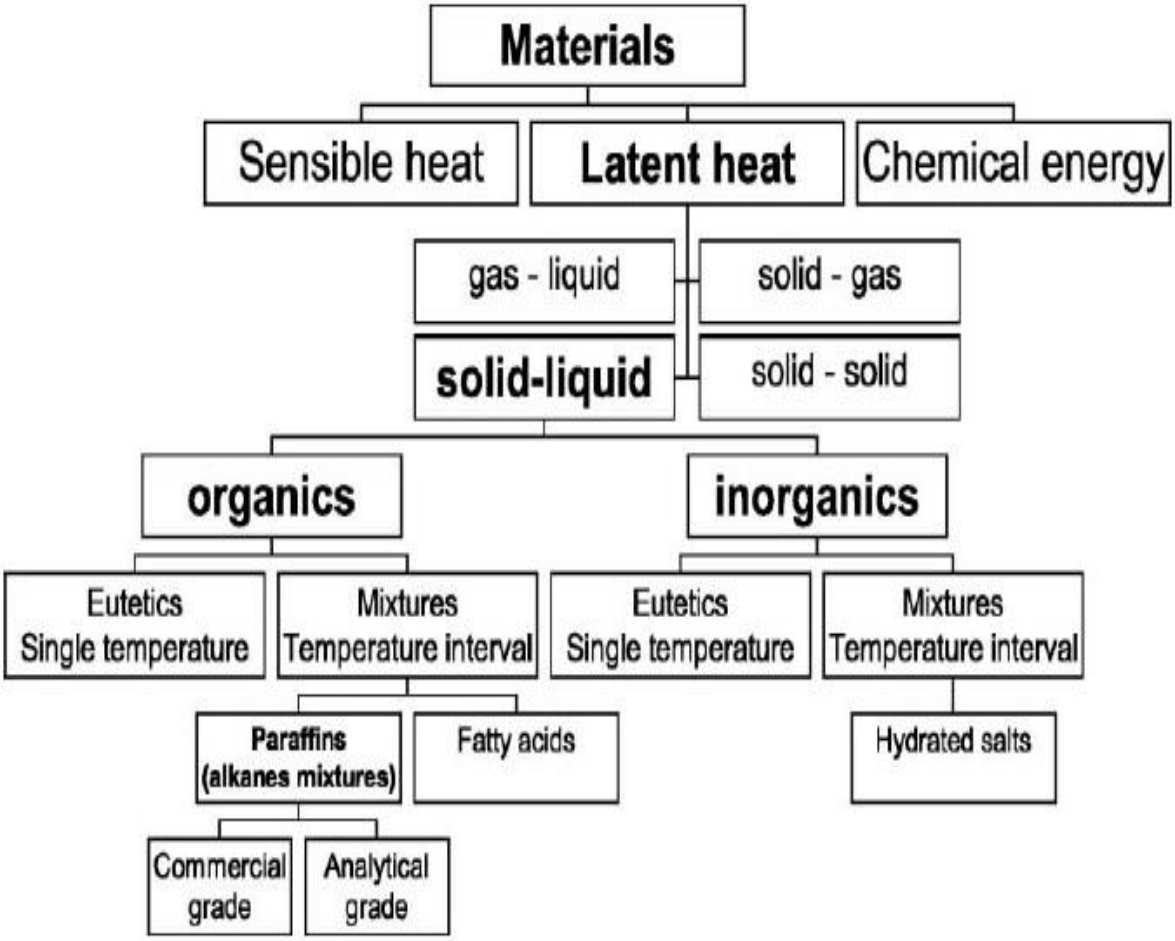

Figure 1.1 Classification chart of phase change materials for latent heat storage (taken from Zalba et al., 2003)

Water

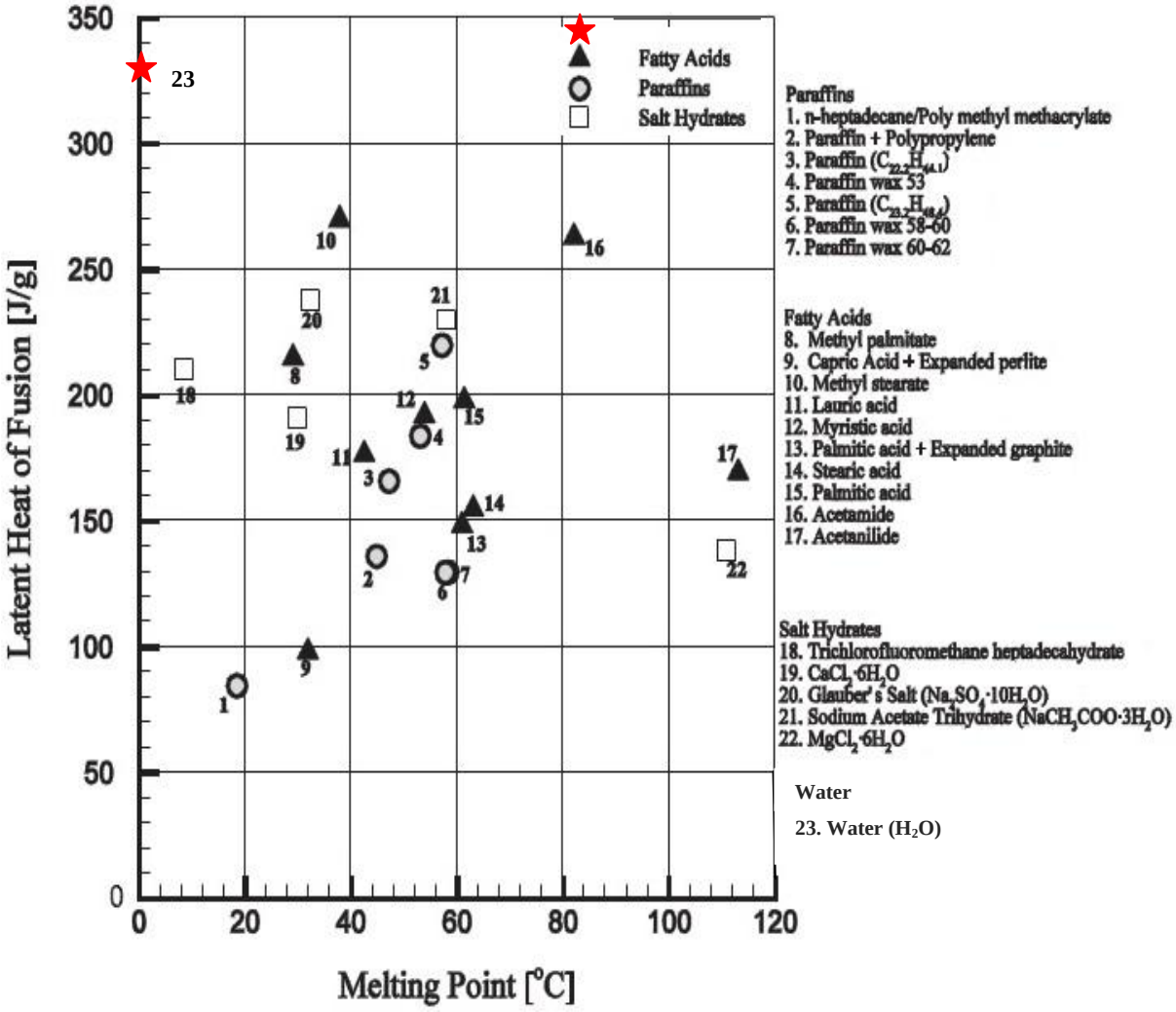

Figure 1.2 Latent heat of fusion per unit mass vs. melting point of different fatty acids, paraffins, salt hydrates and water (reproduced from Rathod and Banerjee, 2013)

Chapter 2 Literature Survey

Utilization of nanostructures to modify the functionalities of phase change materials is a recent undertaking that has gained greater momentum in recent years. In this chapter, a review of recent studies that focused on enhancing the thermal conductivity due to introduction of nanostructures into phase change materials for thermal energy storage is presented. Emphasis of the work has been placed on the dependence of the enhanced thermal conductivity on mass fraction of the nanostructures and temperature for both liquid and solid phases. In general, carbon-based nanostructures and carbon nanotubes exhibit far greater enhancement of thermal conductivity in comparison to metallic/metal oxide nanoparticle. All the figures (except Figure 2.1) in this manuscript are taken from the reviewed papers.

2.1 Introduction

Covering the period of 2001 to mid-2013, the number of published papers on phase change materials along with their publication year is summarized in Figure 2.1. Prior to 2005, on average 34 papers per year were published. However, a new surge of interest on research of PCM has been witnessed. A recent review of studies that focused on enhancing thermal conductivity due to introduction of nanostructures in phase change materials for thermal energy

storage was presented by Khodadadi et al. (2013) that documented a steady rise of research activity on thermal conductivity enhancement of PCM through utilizing nanostructure enhancers. These emerging materials have only been studied since 2005 and they constitute a clear departure from previous/existing practices of utilizing fixed, stationary high conductivity inserts/structures into PCM (Fan and Khodadadi, 2011). Carbon-based nanostructures (nanofibers, nanoplatelets and graphene flakes), carbon nanotubes, both metallic (Ag, Al, C/Cu and Cu) and metal oxide (Al_2O_3, CuO, MgO and TiO_2) nanoparticles and silver nanowires have been explored as the materials of the thermal conductivity promoters. The studies have emphasized exploring the dependence of the enhanced thermal conductivity on both the nanostructures' loading mass fraction and the temperature in liquid and solid phases, however issues related to modifications of the degree of supercooling, melting temperature, viscosity, heat of fusion, etc. are also reported. Carbon-based nanostructures and carbon nanotubes generally exhibit far greater thermal conductivity enhancement in comparison to metallic/metal oxide nanoparticles.

Research on nanostructure-enhanced PCM (NePCM) has continued and a summary of work that has appeared since completion of the recent review paper by Khodadadi et al. (2013) or studies that might have been overlooked are reviewed in this chapter. The relevant details of the reviewed papers are summarized in two elaborate Tables 2.1 and 2.2. The specific materials and their properties (both PCM and nanostructures) along with the size information and mass/volume fractions of the thermal conductivity enhancers are given in Table 2.1. Preparation techniques for the colloidal dispersions that are generally achieved by mixing followed by possible use of sonication and utilization of surfactants or lack of it for realizing stable dispersions are summarized in Table 2.2. As for the characterization techniques, specific

attention is given to the employed method(s) for measuring thermal conductivity and the extent of its measurement (one or multiple temperatures and for which phases). Moreover, any stability concerns expressed by the authors and some details of any phase change heat transfer tests are summarized in Table 2.2.

2.2 Review of Recent Studies on NePCM

Research activities focusing on NePCM have intensified since preparation of the original review paper by Khodadadi et al. (2013). Thus, it is appropriate to discuss the recent developments and trends in this chapter.

Gao et al. (2009) conducted thermal conductivity measurements in both solid and liquid phases using the transient hot wire (THW) method. Within the solid state, Brownian motion is not present, whereas control of the clustering (aggregation) mechanism was afforded via using different matrix materials. Alumina nanoparticles (70 nm mean diameter and polydispersity of 0.124 validated by Dynamic Light Scattering (DLS) were dispersed in n-hexadecane (99.5% purity, melting temperature (MT) of 18 ^{o}C) and hog fat. Whereas n-hexadecane is a linear alkane, hog fat is a mixture of saturated and unsaturated fatty acids and exhibits a MT in the 25-30 ^{o}C range. Once frozen, hog fat is amorphous, whereas hexadecane is polycrystalline. The nanofluids (0.5, 1 and 2 vol%) were prepared following a two-step method of dispersing alumina within 30 mL of the host liquids that were fully mixed with two droplets of Span 80 (Fluka) stabilizer. In order to form a stable suspension, high-energy ultrasound was applied. Thermal

conductivity measurements were performed during the heat-up and cool-down steps between 5 and 52 °C. The samples were heated using a thermal bath with 1 ^{o}C accuracy, whereas a mixture of water and ice was utilized during the cool-down step, however the order and frequency of the steps were not discussed. Measured thermal conductivity values at a given temperature were the same within 0.2% during these steps and the average values of thermal conductivity enhancement were reported (Figure 2.2) along with the predictions of the Maxwell-Garnet (1873), denoted as the MG model. The maximum difference between the measured and MG-predicted thermal conductivity values in both phases for the hog fat samples was about 0.5% and the thermal conductivities of the solids samples were slightly below the liquid sample data. On the other hand, measured thermal conductivities of the hexadecane-based solid samples were consistently higher than liquid sample data and the maximum difference between the measured and MG-predicted thermal conductivity values in both phases was about 3.3%. The observed different trends were explained by the microstructures of the particles in the two states. Transmission electron microscopy (TEM) images of the hog fat samples drawn from both phases did not exhibit noticeable difference of nanoparticle aggregation upon freezing due to its amorphous state in solid phase. Well-dispersed alumina nanoparticles in liquid phase of hexadecane-based colloids seen in the TEM image shown in Figure 2.3a, however, agglomeration of particles in an oriented pattern within the hexadecane crystal structure upon freezing was observed (Figure 2.3b). The nanoparticle aggregates were two types of clusters. Spherical clusters were formed by larger diameter particles, whereas randomly-oriented "backbone" structures were composed of small diameter nanoparticles. The high aspect ratio of the backbone chainlike clusters plays the key role in the thermal conductivity enhancement of the solid phase that is greater than the value predicted by the model of homogeneously-dispersed

spherical nanoparticles. Upon remelting, the continuous clusters broke into short clusters and the measured value of thermal conductivity was very close to that of the original liquid sample. These observations on clustering in hexadecane-based solids and lack of it for hog fat rules out the marked effect of the Brownian motion-induced mechanism of thermal conductivity enhancement. This was further supported by the independence of the measured thermal conductivity values from temperature for both phases of hog fat/alumina colloids (Figure 2.2a). Due to limitations of the experimental set-up, the authors provided solid phase thermal conductivity data for hexadecane colloids at one temperature only. The authors proceeded to discuss that the effective medium theory cannot explain the enhanced thermal conductivity of the solid phase due to the spherical clusters only and thus focused on models that account for rod-like clusters.

Shaikh and Lafdi (2010) experimentally studied different composite PCM systems for thermal control (TC) of electronics under uniform and transient power heat loads. Paraffin wax, carbon nanotubes (CNTs), and carbon-carbon (C/C) composites were used to make 2 different testing samples. Multi-walled carbon nanotubes (MWCNTs) were embedded within the base PCM to enhance their effective thermal conductivity and latent heat. C/C sheets were used as a casing enclosure of the PCM samples in order to hasten the rate of heat transfer through the composite PCM. The first testing sample consisted of a series of three PCM, i.e. shell wax 100, paraffin wax, and EPAL paraffin wax, with different melting temperature in a column design as it appears in Figure 2.4. The three PCM layers were positioned from top to bottom based on decreasing order of their melting temperature. The main aim of this configuration was to further increase the rate of melting of the PCM system. The second sample was made of similar PCM with the same melting points within the same configuration as the first sample. The size of each

sample was 70×50×50 mm. A pre-designed test-rig was also fabricated to apply different heating loads regimes to the composite samples. The setup was made to collect the temperature distribution history of the composite systems at different locations. It was done through reading the thermocouples outputs using ExceLINX software and then converting them to temperature. The whole test-rig was also placed into a vacuum chamber to exclude the possible heat loss via natural convection to the environment. The two different samples described above were tested for three separate cases. The case-1 consisted of the base PCM composites without any nano-particle loading. For the case-2, 1 vol% of single-walled carbon nanotube (SWCNT) was added into the PCM. The case-3 was similar to case-2 except adding two 1 mm thickness sheets of MWCNT as TIM at two interfaces. Two types of heat loads, i.e. uniform and pulsed power, were individually applied to the samples to analyze their thermal performance. Under both conditions, the case-2 showed a bigger reduction in the maximum junction temperature comparing to case-1. However, the case-3 exhibited the greatest decrease in both heater and junction temperatures compared to the other cases. Furthermore, the first testing sample with different PCM revealed greater energy storage capacity and higher heat dissipation rate in comparison with the 1-PCM composite sample. It was finally concluded that using CNTs as both nano-additives and TIM within the paraffin wax will result in improving the thermal performance of a TC system. This protection is especially of great importance against pulsed heat loads in electronic applications.

Ai et al. (2010) investigated ZrO_2 (zirconia) nanopowders with mean diameter of 26 nm (verified by X-ray diffraction (XRD) and TEM) that were mixed with stearic acid powders (MT of ~66.5^{o}C) phase change materials by high-speed milling. Carbon tetrachloride and chloroform were also used as dispersants by adding 100 mL during milling and the sampled were identified as CT and CF, respectively. Another dispersant solution composed of an amido macromolecule

polymer was used to modify the surface of the nanopowders initially and those samples were identified as CTP and CFP. For the four samples, the stearic acid content was maintained at 23 wt%. The bulk thermal properties of the samples identified as the heat capacity factor (HCF that is inversely related to the derivative of temperature with respect to time) were evaluated by analyzing the data of a differential thermal analysis (DTA) test over a 4-sec testing period. During this period, the sample temperature ranged from about 20 to 150 ^{o}C. The CF samples exhibited the greatest HCF value among all samples suggesting the better performance of untreated zirconia nanopowders dispersed in chloroform as PCM.

Wang et al. (2011) investigated grafting (chemical functionalization) of tethers to multi-walled carbon nanotubes (CNT) and combining the functionalized CNTs with palmitic acid (PA) and paraffin wax (PW) to modify the thermal properties. Pristine CNTs (P-CNT) were 95% pure (average diameter, average length and specific surface area of 30 nm, 50 μm and 60 m^2/g, respectively). Palmitic acid (98% pure) with a MT of 62.5-64 ^{o}C, density of 853 kg/m^3 and latent heat of 209.2 J/g, and industrial-grade paraffin wax (PW) with a MT of 48.2 ^{o}C and latent heat of 142.2 J/g . Prior to grafting of the P-CNTs with straight carbon chains, i.e. oleylamine ($C_{18}H_{37}N$) and octanol ($C_8H_{18}O$), the P-CNTs were modified to create –COOH groups on its surface. This was achieved through a lengthy treatment process of (1) boiling and refluxing in a concentrated mixture of nitric/sulfuric acids, (2) dilution by distilled water, filtration and washing to eliminate traces of acid treatment followed by drying, (3) boiling in $SOCl_2$ that contained dimethylformamide (DMF) to change the –COOH groups to –COCl to accommodate easier reacting with grafting chains and (4) washing with anhydrous tetrahydrofuran 3 times before drying in a vacuum to remove DMF, $SOCl_2$ and the outgrowth. The treated CNTs were then stirred with oleylamine and octanol at 70 and 50 ^{o}C for 120 hours, respectively. Upon

removing the organic solvent, the samples were dried under vacuum at room temperature. The grafted CNTs by oleylamine and octanol were named G18-CNTs and G8-CNTs, respectively. P-CNTs and grafted CNTs were then introduced into molten PA and the mixture was sonicated intensively to promote dispersion and homogeneity. Similarly, P-CNTs and grafted CNTs were combined with PW through whisking and intensive sonication. For both PA- and PW-based samples, the weight fractions of the CNTs were 0.005. Traces of grafted organic membranes on the CNTs were observed in the TEM images and this was further verified by XRD spectra measurements. The samples were also subjected to the Fourier transformation infrared (FTIR) technique. The samples were subjected to repeated cycles of 12 h heating at 70 ^{o}C in an oven followed by 2 h of cool-down at room temperature. Even though P-CNT/PA samples were delaminated after one cycle, the grafted samples exhibited stability even after 80 heat-up/cool-down cycles. Polarizing optical microscopy (POM) images of the stability-tested samples are shown in Figure 2.5. The grafted samples (Figs. 2.5c and 2.5d) are observed to be homogeneous after 80 cycles of heat-up/cool-down. The measured value of heat of fusion (obtained by differential scanning calorimetry (DSC)) of G18-CNT/PW was higher than the value for PW, whereas the values for G8-CNT/PW and P-CNT/PW were lower than PW. In comparison, for all PA-based colloids, the values of heat of fusion were lower than pure PA. Melting temperature and solid-solid phase change temperature and heat of fusion values were also reported. The average values of three thermal conductivity measurements that were obtained using the THW method for each sample are given in Figures 2.6a-b for PW and PA based colloids. The measurements were obtained over a wide range of temperature covering both liquid and solid states. Disregarding the P-CNT/PW samples in Figure 2.6a, the G18-CNT and G8-CNT grafted samples exhibit progressive improvements of thermal conductivity when

compared to pure PW at each measured temperature for both phases. Moreover, the thermal conductivity values generally decay as the sample temperature is raised and a sharp decline near the MT (~48.2 ^{o}C) is not observed. Whereas P-CNT/PW solid samples exhibit the highest measured thermal conductivity values, their thermal conductivity values in the liquid phase is nearly equal to the value of PW, suggesting that sedimentation of pristine untreated CNTs might be responsible for this behavior. Whereas the three PA-based colloids have thermal conductivities higher that pure PA regardless of measurement temperature and phase (Fig. 2.6b), the lowest and highest enhanced thermal conductivity values are consistently exhibited by P-CNT/PA and G8-CNT/PA (e.g. 20.6% at 45 ^{o}C). The PA-based thermal conductivity values for each phase are less dependent on measurement temperature when compared to the PW-based samples.

Hu et al. (2011) introduced aluminum nitride (AIN) nanoparticles as a nucleating agent into sodium acetate trihydrate (SAT) phase change material to resolve its supercooling issue during solidification. SAT (purity> 99%) was selected as the PCM due to its high energy storage density and high thermal conductivity. Carboxyl methyl cellulose (CMC) was also used as a thickener for SAT to prevent both undesirable phase segregation of the PCM and sedimentation of dispersed AIN nanoparticles. The supplier company provided AIN nanoparticles (purity> 99%) with the average size of 50 nm. After weighing, AIN nanoparticles with the range of 3 to 5 wt% and 4 wt% of CMC were added to SAT and mixed together. The final well ground samples were then poured into stainless steel test tubes. Agilent 34970A data acquisition equipment along with T-type thermocouples (with an accuracy of 0.1 °C) were used for temperature readings. To examine the stability of the NePCM, the most concentrated sample (i.e. 5 wt% of AIN and 4 wt% of CMC) was frozen and melted for 50 cycles. As the result, no phase segregation and

supercooling were observed. Furthermore, the data show that by loading 3-5 wt% of AIN nanoparticles into the thickened SAT the supercooling was deducted by 0-2.4 °C. Based on TG-DTA results, the addition of nanoparticles plus CMC can also improve the dehydration temperature of SAT. On the other hand, DSC tests revealed that the latent heat and phase change temperature of NePCM were a bit lowered compared to pure SAT. To evaluate the aggregation status of AIN nanoparticles dispersed in SAT, environmental scanning electron microscopy (ESEM) along with a particle size analyzer apparatus was used. The size of AIN was ranged from 95 to 300 nm which suggest good dispersion of nanoparticles into SAT with some aggregation. Finally, by using an optical microscope, the crystal size of NePCM was observed to be much smaller than pure SAT crystals. This observation proves the ability of added CMC to prevent phase segregation.

Emphasizing thermal management of electronics and particularly the application of PCM to operating conditions involving pulsed power profiles, Sanusi et al. (2011) explored graphite nanofibers as fillers. An alkane, n-tricosane ($C_{23}H_{48}$), with MT of 54-58 ^{o}C, heat of fusion of 220 kJ/kg and solid phase thermal conductivity of 0.2 W/mK (temperature not specified) was utilized. Three types of graphite nanofibers (GNF) identified as platelet, ribbon and herringbone with diameters of 2-100 nm and lengths of up to 100 micron were prepared by catalytic deposition of hydrocarbons and CO on an iron catalyzer. Based on prior experience with PCM/GNF composites in relation to melting, only herringbone type of nanofibers was investigated in this study that was focused on effectiveness of PCM/GNF during solidification. Samples of PCM/GNF (10 weight %) were prepared by mixing of GNF and liquid n-tricosane followed by sonication for over four hours, leading to a shape-stabilized composite. Rectangular aluminum box modules (3 mm thick walls) with an open top side that were heated from bottom

using a heater block hosting 2 cartridge heaters (100-1,000 W) were filled with the composite and were used for solidification experiments. A cold top surface kept at 5 ^{o}C by a circulating 50/50 ethylene glycol/deionized water mixture was utilized. The modules were also instrumented with five (5) stainless steel sheathed type T thermocouples. The molten samples were poured gently into the modules and allowed to cool to ambient temperature. The entire system was insulated using mica slabs and then wrapped in mineral wool insulation. With the cold plate operational, the heater is set at a power loading and the solid PCM is heated. Upon reaching steady state based on thermocouple readings at various heights within the module or upon significant super heat of PCM occurs (PCM temperature > 90-115 ^{o}C), the heater and circulating cold plate are shut down. In effect, a melting period of a thermally-stable column of PCM is followed by its cool-down/solidification. The heat transfer data for the GNF/PCM-based units indicated that there was substantial reduction of the solidification time when compared to the pure PCM.

Promoting colloids in general and those with nano-scale additives in particular, as materials accommodating reversible regulation/tuning of electrical and thermal conductivity in response to first-order phase transitions, Zheng et al. (2011) prepared suspensions of graphite/hexadecane (0.2, 0.5, 0.8 and 1 vol%). Natural graphite that was subjected to intercalation using sulphuric acid, microwave expansion and ultrasonic dispersion transformed into exfoliated graphite flakes that had an average diameter of several microns with a thickness in the range of several nanometers to several tens of nanometers (scanning electron micrograph (SEM) image shown in Fig. 2.7a). Graphite flakes that were observed to be bent or even rolled up (TEM images also showing ~30 atomic layers with an interplanar distance of 0.335 nm) were then mixed with hexadecane ($C_{16}H_{34}$, MT of about 18 ^{o}C). An optical microscope image of a 0.2

vol% suspension is shown in Fig. 2.7b. A photo of a 50 ml stable suspension sample (0.2 vol%) after 3 months on the shelf is also shown as an inset. Measured mobility of graphite flakes in hexadecane was ~0.03 $cm^2 V^{-1} s^{-1}$ which indicates that the flaked were charged. Based on X-ray photon spectroscopy (XPS) analysis, ~8% oxygen atoms were sensed on the surface of the flakes that were attributed to hydroxyl, epoxide and carboxyl functional groups, which in turn play a marked role in the stability of graphite suspensions. The evolution of the microstructure of a dilute (0.05 vol%) colloid during phase change was imaged using an optical microscope. The charged attracting graphite flakes formed clusters in the liquid phase (Fig. 2.7c), however upon freezing the flakes were moved to the grain boundaries due to the non-isotropic needle-like crystallization of hexadecane with a signature 3-dimensional percolation network (Fig. 2.7d). Once the frozen colloid was re-melted, the percolation network remained, whereas a small portion of the flakes were observed as suspensions (Fig. 2.7e). The measured thermal conductivity of the samples (0.2-1 vol%) at various temperatures for both liquid and solid phases that were obtained using the transient hot wire technique are shown in Figure 2.8. In the liquid phase, the thermal conductivity is independent of temperature for a given volume percentage, however its value rose as the loading of graphite was increased. As the colloid froze, the thermal conductivity rose abruptly. For the 0.8 vol% sample, the contrast ratio of thermal conductivity (ratio of thermal conductivity between the solid and liquid phases) was equal to 3.2, the highest among all the samples (shown as inset in Figure 2.8). The 0.8 vol% sample was cycled through freezing and melting processes and the associated thermal conductivity measurements at 3 ^oC and 25 ^oC are shown in Figure 2.9. The highest contrast between the measured solid and liquid thermal conductivity values was observed for the first cycle (data of Figure 2.9), whereas cycle-to-cycle variations of the thermal conductivity diminished as more cycles were processed. This

signified the permanency of the percolation network. The strategy was extended to other stable colloids of 1 vol% graphite/water and CNT/hexadecane that exhibited enhancement of electrical conductivity upon solidification. However, insensitivity of electrical conductivity of a 0.4 vol% graphite/polyethylene glycol 400 colloid upon phase change highlighted the important requirement for a crystalline forming base liquid.

Teng et al. (2011) utilized a homogenizer, electromagnetic agitation and ultrasonic vibration to disperse and alumina (Al_2O_3) nanoparticles, in liquid paraffin wax. For both additives, the weight percentages were 1, 2 and 3 wt%. Samples were then placed into test tubes that were then subjected to charge/discharge of thermal energy experiments while placed in isothermal baths. Temperature vs. time variations of the samples were then recorded and the improved charge/discharge characteristics of the improved PCM were observed.

Bayramoglu (2011) prepared 5 g colloids with weight fractions of 1.25, 2.5, 5 and 10 by combining pure n-octadecane (MT of 28 ^oC, density of 782.2 kg/m^3 and latent heat of 239.9 J/g) with 95% purity MWCNTs (3-20 nm outer diameter, 1-3 nm inner diameter and 0.1-10 microns in length). MWCNTs were added to molten n-octadecane held at 30 ^oC and the mixture was ultrasonicated for 5 minutes at 40 ^oC. To prepare the colloids for DSC (operated from 0 to 50 ^oC at 10 ^oC/min) and thermogravimetric analysis (TGA), the samples were melted and then sonicated for 5 minutes while held at 40 ^oC. The samples were also subjected to TEM and optical microscopy. Thermal stability of the samples was studied by performing 1440 repetitive melting/freezing cycles between 19 and 35 ^oC, followed by DSC and TGA analyses. Images of crystallized pure and colloidal samples obtained using optical microscopy provided qualitative information about the composites. The reported increase of the latent heat for the 1.25 wt% sample did not follow the mixture rule for this property.

Kalaiselvam et al. (2012) performed experimental studies of melting and solidification of six PCMs that were contained within spherical capsules. The PCMs were 60% n-tetradecane/40% n-hexadecane, capric/lauric acid, $CaCl_2$-$6H_2O$, n-octadecane, n-hexadecane and n-eicosane that hosted aluminum and alumina nanoparticles at a volume fraction of 0.07. No information on the thermophysical properties of the PCM/nanoparticles was provided and details of the preparation schemes of the colloids were lacking. The measured interface positions followed the trends of the predictions of a one-dimensional transient model of phase change.

Jesumathy et al. (2012) focused on the enhanced heat transfer that can be achieved by increasing the thermal conductivity of the storage material of a PCM-based thermal energy storage system. Utilizing a paraffin wax (MT of 58.2 ^{o}C), CuO nanoparticles with a mean diameter of 40 nm (weight percentages of 2, 5 and 10) were dispersed in the liquid PCM maintained at 60 ^{o}C. The suspensions were not treated with any surfactant but were subjected to an ultrasonic vibrator (pulses of 100W at 36±3 kHz) for 6 hours. The samples were then held for 24 hours in a hot air oven at 70 ^{o}C and no precipitation was observed. Keeping the samples in a constant-temperature bath, the thermal conductivities of the samples were measured for both liquid and solid states using a commercial transient hot wire apparatus (KD2 Pro). The details of the order of measurements (liquid first followed by solid or the reverse) were not provided. The thermal conductivity data for both liquid and solid samples of various loadings that were obtained at different temperatures are given in Figure 2.10a. The thermal conductivity of the solid phase particle-free paraffin wax declined mildly as the temperature was raised followed by a sudden rise near the melting temperature, whereas the single data point in the liquid phase was the lowest value recorded. The colloid samples exhibited monotonic enhancement of thermal conductivity with loading of the nanoparticles for both phases with the liquid sample at 65^{o}C

registering 13.21% enhancement. The sudden rise of the thermal conductivity value near the melting temperature was observed for all the samples. Viscosity of the liquid samples that were measured using a cone and plate viscometer is shown in Figure 2.10b. At each measurement temperature, the viscosity value was enhanced monotonically as the particle concentration was increased further. DSC-based measurements revealed both solid-solid and solid-liquid phase transitions for the samples and little sensitivity of the melting temperature on the particle loading. The values of the latent heat of fusion for the pure wax and a 10 wt% colloid were 210 and 118.9 kJ/kg, respectively. The system-level performance of the thermal storage system was enhanced in response to utilization of thermal conductivity-enhanced PCM.

Freezing point of γ-Al_2O_3/water nanofluid was investigated by Mare et al. (2012) who dispersed alumina nanoparticles (30 nm diameter) in deionized water with a 1% (mass concentration) of unknown surfactant. The volume percentages of the samples were 1, 2, 3 and 4. Based on DLS experiments, it was established that the particles have agglomerated with an average diameter of 400 nm. Upon placing the samples originally at the room temperature into a cold room, the instantaneous temperature data were analyzed using the T-history method to extract the heat of fusion data. Moreover, the degree of supercooling was observed to decrease as the particle loading was increased.

Wu et al. (2012) utilized a two-step method to disperse 99.9% purity copper nanoparticles (average particle size of 25 nm) in 99.99% purity paraffin (MT of 58-60 ^{o}C). In one approach, Hitenol BC-10 was utilized as the surfactant. Based on experience with similar colloids, copper to Hitenol BC-10 weight ratio of 1:2.6 was used. In another approach, samples were prepared by ultrasonication. Pure paraffin, Cu/paraffin and thermally-cycled Cu/paraffin samples (100 times between 30 and 70^{o}C) were subjected to the FTIR technique and no distinct

difference among these were observed. A thermal constants analyzer (TPS) was used for measuring the thermal conductivity of the samples in both liquid and solid phases with an uncertainty of ±1%. This was achieved by dipping the Kapton-insulated probe into the molten samples at 70 ^{o}C or clamping the probe by two pieces of solid samples at 25 ^{o}C. The measured thermal conductivity values for both liquid and solid samples are shown in Figure 2.11. As the mass fraction of the Cu nanoparticles is increased, the thermal conductivity of both liquid and solid samples is enhanced with the solid samples exhibiting greater thermal conductivity values at a given loading. The colloidal samples contained in beakers were then placed in 30 and 68 ^{o}C constant-temperature baths to observe the freezing and melting processes, respectively. An infrared imaging instrument was utilized to monitor the surface of the samples qualitatively. The infrared images of the samples consistently exhibited reduced freezing/melting time periods.

Kumaresan et al. (2012) utilized RT-20 paraffin (MT of 18-23 ^{o}C, freezing temperature of 19-22 ^{o}C, liquid/solid densities of 770/880 kg/m^3 at 25/15 ^{o}C, thermal conductivity of 0.2 W/mK and latent heat of 134 J/g) as the base PCM. MWCNT (average diameter, average length and specific surface area of 30-50 nm, 10-20 μm and 60 m^2/g, respectively) was used. The nanotubes were subjected to ultrasonication under dry conditions in order to untangle them. Using a two-step method without surfactants/dispersants, MWCNTs were dispersed in liquid paraffin (0.15, 0.3, 0.45 and 0.6 vol%) and then subjected to a magnetic stirrer for 60 minutes. This was followed by continuous sonication in an ultrasonic bath maintained at 30 ^{o}C for 30 minutes. The thermal conductivities of the samples for both liquid and solid states were measured using a commercial transient hot wire apparatus (KD2 Pro) while keeping the samples in a constant-temperature bath. The viscosity of the liquid samples at 30 ^{o}C was measured using a rheometer. The colloids were also tested using DSC operated from 0 to 30 ^{o}C at 1 to 3 ^{o}C/min.

Freezing of the samples were also studied by placing liquid samples (25 ^{o}C) in copper cylindrical containers (6.6 cm diameter) that were then placed in constant-temperature bath that was maintained at 13 ^{o}C. Five resistance temperature detector (RTD) probes were placed an equal distance apart at different radial positions on the mid-plane of the cylinder and the temperature readings were recorded during the solidification process. The measured thermal conductivity data for various loading of MWCNTs at various temperatures covering both the liquid and solid states are shown in Figure 2.12. It was implied that the measurements were obtained for the highest temperature first and then the temperature of the samples were lowered. The thermal conductivity data for the solid phase are consistently higher than that of the same sample in liquid phase. Moreover, at a given temperature, as the loading of the nanotubes was increased, the thermal conductivity increased monotonically. The greatest observed enhancements were of the order of 50-55 percent for the 0.6 vol% samples at 20 (solid) and 35 ^{o}C (liquid). The measured viscosity data exhibited shear-thinning (non-Newtonian) behavior for low values of applied shear stress. However, for higher values of the shear stress, constant viscosity values were observed and the viscosity values increased as the loading of the nanotubes was raised. DSC results showed that there was no marked change of the freezing/melting temperature and only a small change in the heat of fusion values was sensed. The degree of supercooling decreased with loading of the nanotubes and it attained its lowest value for the 0.15 vol% samples. Time-dependent temperature readings that were obtained at the center of the freezing cell (Figure 2.13) clearly exhibit that the samples with greater loading of nanotubes consistently freeze at a faster rate.

Harikrishnan and Kalaiselvam (2012) studied colloids of oleic acid (density of 887 kg/m^3, specific heat capacity of 2.043 kJ/kgK and heat of fusion of 140.2 kJ/kg) with dispersions

of CuO nanoparticles with sizes ranging from 1 to 80 nm. The copper oxide nanoparticles were prepared in-house following a precipitation method. Adopting a two-step method, ultrasonication was applied at 45 ^{o}C and was maintained for 30, 35, 40 and 45 minutes for 0.5, 1, 1.5 and 2 wt% samples, respectively. The samples were characterized utilizing TEM, XRD, TGA, DTA and DSC. Using the experimental set-up previously reported by Kalaiselvam et al. (2012), melting and solidification of samples were also investigated. Some samples were subjected to 150 freeze/thaw cycles. The measured phase change temperature and latent heat values that were evaluated during these cycles did not reveal marked changes. Thermal conductivity of the liquid samples were measured at 25 ^{o}C using the LFA 447 Nanoflash analyzer and are presented in Figure 2.14. Linear dependence of thermal conductivity on mass fraction is observed for low particle concentrations followed by a nonlinear dependence at higher loading and the greatest enhancement was 98.66% for the 2 wt% sample. Reduction of freezing/melting times for the 0.5, 1, 1.5 and 2 wt% samples were 10.71/7.14, 16.07/14.28, 19.64/25 and 27.67/28.57%, respectively.

High aspect ratio copper nanowires (Cu NWs) were introduced into tetradecanol (TD) as an organic phase change material by Zeng et al. (2012). The goal was to study the effects of nanowires on the thermal and structural properties of TD. After mixing specific amounts of Cu NWs (0.0625, 0.125, 0.745, 0.961, 1.43, 2.78, 4.75, 5.14, and 11.9 vol%) and acetone with tetradecanol, ultrasonication was performed on the samples for 10 min at 50 °C. This was followed by leaving the samples at the environment to exclude the acetone through natural evaporation. Thereafter, 1 hour of extra ultrasonication at 50 °C was carried out to disperse the nanowires within the PCM uniformly and to ensure the exclusion of acetone. The colloids again cooled down to the ambient temperature and dried out in a vacuum oven for 24 hours. The dried

composite PCM were then ground and the resulting powders compressed at a high pressure of 20 MPa to get two identical 13 mm thickness cylinders. Following the same procedure, a 50 wt% copper nano-particles (Cu NPs)/TD solid sample was fabricated in order to compare the amounts of thermal conductivity enhancement for Cu NWs and Cu NPs. Scanning electron microscopy (SEM) and X-ray diffraction (XRD) were utilized to investigate the surface morphology and structural aspects of PCM powders. SEM image of Cu NWs successfully showed that a spongy structure has been made as the result of self-entangled nanowires. The results also revealed that TD matrix had wrapped the nanowires. Although, the spongy structure of Cu NWs could absorb tetradecanol inside its vacancies, was not damaged by ultrasonication process. On the other hand, XRD results showed that Cu nanowires were stable within the composite PCM. Differential scanning calorimetry (DSC) and thermogravimetry (TG) were further performed to characterize the thermal energy storage and thermal stability of the solid samples. Comparing DSC curves of pure and nanowire-enhanced solid PCMs, the heat transfer rate across the sides of composites was improved in the presence of Cu NWs. This observation implies higher melting rates of NePCM compared to pure TD. It was also inferred from the TG curves that as the mass fraction of nanowires was increased, their spongy structure could absorb higher amount of TD and consequently the speed of composite weight loss due to evaporation was reduced. Transient plane source (TPS) technique was used to measure the thermal conductivity of the composite PCM at ambient temperature. It was observed that as the loading of copper nanowires increased, the thermal conductivity values followed a monotonic rise (Figure 2.15). For the most concentrated sample, i.e. 11.9 vol%, the thermal conductivity data (2.86 W/mK) was 9 times greater than pure TD (0.32 W/mK). A turning point of 1.5 vol% of Cu NWs was also defined as the point upper which the rate of thermal conductivity improvement showed noticeable increase.

Considering similar vol% of Cu NPs/TD and Cu NWs/TD, the amount of enhancement for nanowires was nearly 3 times higher than copper nanoparticles. It was finally mentioned that ultra-high aspect ratio and spongy structure of copper nanowires are the main role-player which make Cu NWs an excellent candidate to enhance thermal conductivity.

TiO_2-H_2O colloids were proposed as a novel NePCM by He et al. (2012). The effect of three different mass fraction loadings of TiO_2 nanoparticles, i.e. 0.3, 1.2 and 2.4 wt%, on the nucleation supercooling degree of deionized water was studied. Dispersing spherical TiO_2 nanoparticles into deionized water, the sample colloids were prepared by a two-step method. Sodium dodecylben zenesulfonate (SDBS) surfactant was employed to stabilize TiO_2 particles within deionized water. With the aid of a supersonic oscillator, the nanofluids with the mass fractions of 0.3, 1.2 and 2.4 wt% were then well mixed. Utilizing a TEM instrument, it was shown that the average size of spherical TiO_2 nanoparticles was 20 nm. It was also proven that the particles were well dispersed. The samples were then poured into four different test tubes and were placed into a thermostatic bath for cooling experiments. Type-T copper-constantan thermocouples with the accuracy of ±0.2 °C were attached to the central position of the tubes for temperature readings. The thermocouples were linked to a data acquisition apparatus (ADAM4000) and the time interval for data logging was 10 sec. Adopting the mean temperature values of four repeated tests, the final cooling T-t curve for each sample was obtained (Figure 2.16). It was shown that as the mass fraction of TiO_2 nanoparticles increased, the total freezing time and the supercooling degree of nanofluids were both decreased. For the most concentrated sample, i.e. 2.4 wt%, the total freezing time was deducted by 33.33% and the supercooling effect was completely excluded (100% decreased). Furthermore, the data revealed that the phase change temperature is poorly affected by increasing the loading of nanoparticles, i.e. 4.2%

change for the 2.4 wt% sample. It was also found that the bath cooling temperature has a considerable effect on the onset of nucleation and supercooling degree. As the cooling temperature was reduced, the supercooling degree was greater. It was concluded that the addition of TiO_2 nanoparticles will improve the thermal conductivity of the colloids. That's why their application is more advantageous compared to other nucleating agents.

Using direct-synthesis method, Teng et al. (2013) experimentally investigated the thermal behavior of modified phase change materials (MPCM). Paraffin was selected as the base PCM, while graphite and MWCNTs served as the studied nanofillers. Graphite (3.2 μm size) and MWCNTs (20-30 nm size) (1, 2, and 3 wt%) were dispersed into fully refined paraffin to produce the samples. Field-emission scanning electron microscopy (FE-SEM) was carried out and revealed aggregation in both graphite and MWCNTs powders. The outside diameter of MWCNTs, however, was nearly equal to the size reported by the provider company. Graphite particle size distribution was uneven and on average was lower than the pre-specified values. Upon melting of paraffin at 100 °C in a water tank, an electromagnetic stirrer/hot plate was used at 120 °C. Graphite or MWCNTs was gradually added and dispersed into the melted paraffin to reach the pre-defined concentrations under continuous stirring. Then, a high-speed homogenizer was utilized for 40 min at 120 °C to ensure homogenous MPCM colloids. Furthermore, an ultrasonic vibrator was operated at 90 °C for 1 hour to finalize the modification route of MPCMs. Finally, a polypropylene (P.P.) test tube was filled with 40 grams of pure paraffin or a MPCM suspension for charge/discharge temperature tests. K-type thermocouples with an accuracy ±0.1 °C were connected to a data logger apparatus to continuously monitor the temperature of the samples. MPCM colloids were then exposed to charging/discharging experiments for 90 and 80 min, respectively. The reported data was related to last 10 min of the

tests, and was compared to the pure paraffin sample to see the effects of nano-additives. At a constant charging period, the temperature gap between the sample and heating temperature was noticeably decreased while the mass fraction of MWCNTs increased. However, using graphite nanofiller a reverse behavior was observed. This phenomenon revealed that though the thermal conductivity of graphite is much greater than MWCNTs, due to its weak dispersion it cannot contribute to ameliorate the liquid paraffin thermal resistance. Interestingly, during discharging process, it was shown that adding both graphite and MWCNTs highly decreased the temperature difference ratio. A mechanical cooling system along with a differential scanning calorimetry (DSC) apparatus (temperature accuracy of ±0.1 °C) at a constant heating/cooling rate of 4.0 °C/min was used to evaluate the solidification and melting temperatures of the specimens. Utilizing a precision electronic balance (precision of 0.1 mg), the colloids' weight were controlled at 5.0 ± 0.1 mg. A software package was operated to extract the latent heat of the samples from the DSC thermographs in the range of 30 to 70 °C. DSC curves of MWCNTs showed that it can increase the solidification onset temperature and melting peak temperature of paraffin. Furthermore, it caused a bigger range of phase change temperature with a small reduction in both melting onset temperature and solidification peak temperature. On the other hand, adding graphite to paraffin ended up in increasing the onset of melting temperature and decreasing the onset of paraffin solidification temperature. Two distinct phase change peaks with higher heat flow of charging/discharging process were observed. The authors again claimed that there is a link between weak dispersion of graphite in paraffin which increases the porosity of MPCMs and the observed delay in the onset of phase change temperature. In addition, both MWCNTs and graphite additives reduced the melting and solidification heat of paraffin (Figures 2.17-2.18) while adding graphite was more effective. Comparing studied thermal properties of

MWCNTs- and graphite based MPCM, MWCNTs proved to be a promising additive due to its superior dispersion capability in paraffin and its wider applicable temperature range.

Shi et al. (2013) studied the effects of adding exfoliated graphite nanoplatelets (xGnP) or graphene into paraffin matrix phase change material. The goal was to enhance the thermal conductivity and shape-stability of paraffin. Paraffin (n-nanacosane) (MT of 61.6 °C) was used as the base PCM. In order to prepare graphene, commercial graphite powder (99.9995% purity, 2.25 g/cm^3 density, particle size ~700 μm) was provided. Commercial acid-intercalated graphite was also purchased to produce xGnP. After dissolution of paraffin in toluene at 80 °C, graphene or xGnP (1, 2, 5 and 10 wt%) were added to it and the whole sample was sonicated for 30 min. The time allotted for sonication was to ensure that uniform samples were obtained. After evaporating the solvent in a fume hood at 130 °C, the colloids were poured into cylindrical molds of the dimension 50 mm × 10 mm (I.D. × H). Using a vacuum oven at 150 °C, these isotropic NePCM disks were further dried. Transient plane source (TPS) was utilized to measure the thermal conductivity data of the mixtures in both solid and liquid phases. In solid phase experiments, two identical solid disks were used to sandwich the TPS sensor. Then, a 3 W power was supplied to the disks as a step function at 25 °C during 30 sec of data collection. For the liquid samples tests, the sensor/heater was vertically submerged into the colloid at then the tests performed at 80 °C. Liquid phase experimental conditions were chosen so as to avoid convection heat transfer. The obtained thermal conductivity values for the solid disks were generally greater than that of liquid samples (Figure 2.19). It was shown that in both phases, graphene thermal conductivity enhancement was much lower than paraffin/xGnP samples. Since the thermal conductivity of a single-sheet graphene is very high (4400-5300 W/mK), this observation was quite surprising. The authors claimed that it was occurred due to big interfacial/contact thermal

resistance among a large number of contact layers within their small size graphene flakes. On the other hand, as the mass fraction of xGnP increased, the thermal conductivity value of paraffin/xGnP composites improved. For example, for 10 wt% solid paraffin/xGnP, the thermal conductivity value (2.7 W/mK) was 10 times bigger than that of pure solid paraffin (0.25 W/mK). Three different routes of mixing the nano-fillers into the base PCM were also investigated to compare the final thermal conductivity values. In the first method, the nano-fillers were added to the solution of paraffin/toluene and then sonicated. The only difference of the second route was that toluene solvent was excluded. For the third method, a 3-roller mill was utilized to mix the paraffin and nano-fillers powders. It was shown that the first method provided highest thermal conductivity values, while the third method was the least effective one with a difference up to 40%. It was finally concluded that the better uniformity of fillers dispersion leads to greater enhancement in thermal conductivity data of the NePCM composites.

Yu et al. (2013) experimentally studied the effect of carbon-base nano-additives on the thermal conductivity values of liquid-based paraffin suspensions using the transient hot wire (THW) method. The nano-fillers of interest were pristine short MWCNTs (S-MWCNTs), carboxyl-functionalized short MWCNTs (C-S-MWCNTs), long MWCNTs (L-MWCNTs), graphene nano-platelets (GNPs), and carbon nano-fibers (CNFs). As for the base PCM, a paraffin wax (melting temperature (MT) of 58-60 °C) was used. After melting and degassing the paraffin at 110 °C for 3 hours in a vacuum oven, a selected nano-filler (1, 2, 3 and 4 wt%) was added to the paraffin. Thereafter, to ensure having a well dispersed colloid, a magnetic stirrer and a bath sonicator both at 75 °C were utilized for 15 min and 50 min, respectively. Considering the pure liquid paraffin sample, finally 21 testing samples were prepared. Scanning electron microscopy (SEM), atomic force microscopy (AFM), transmission electron microscopy (TEM),

and dynamic light scattering (DLS) were all performed to quantify the actual size, shape, thickness, surface morphology and distribution of suspended carbon nano-materials. All the SEM images of CNTs and CNFs show thin-wire-shaped structures with approximate diameters of 20, 20, 40, and 100 nm, for S-MWCNTs, C-S-MWCNTs, L-MWCNTs, and CNFs, respectively. On the other hand, GNPs had planar high aspect ratio geometry with a size of greater than 1 μm and a thickness of 78 nm. This thickness included nearly 230 mono-layers of graphene with the aspect ratio of 200. It was concluded that these quantified values were somehow bigger than pre-specified sizes by the suppliers. Therefore, it was suggested that clustering in the received nano-materials might have happened. As for the stability concerns, all the 5 test colloids with the highest concentration (4 wt%) were found to be visually stable during 1.5 h of the property measurements. The thermal conductivities of the liquid samples at 65 °C were measured using a commercial transient hot wire apparatus (KD2 Pro) while keeping the samples in a constant-temperature bath with the accuracy of 0.01 °C. With the aid of a T-type thermocouple (uncertainty of 0.3 °C), the variation of temperature within the sample was checked. Each data point (Figure 2.20) represents an average value of 5 repeated tests for the same sample with a standard deviation less than 1%. The figure shows that as the amount of loading of carbon nano-additives increased, the thermal conductivity values went up. However, the rate of enhancement was highly dependent on the shape and size of the added nano-material. Due to 2-D high aspect ratio planar structure of GNPs, they caused greatest improvement in the obtained thermal conductivity values compared to other studied nanostructures. For example, for 4 wt% liquid paraffin/GNPs colloid, the thermal conductivity value (0.29 W/mK) was twice bigger than that of pure liquid paraffin. Utilizing a rotational viscometer, the dynamic viscosity of the liquid samples was also measured at 65 °C. At high loadings of GNPs, the paraffin/GNPs

colloids exhibited an interesting decreasing trend of viscosity while all other samples showed a monotonic increasing behavior versus mass fraction of nano-additives. These positive aspects of GNPs, makes them a favorable agent for thermal conductivity enhancement in case proper physical/chemical functionalization addresses their stability issue in advance.

2.3 Concluding Remarks

A review of 20 recent research papers on NePCM, i.e. from 2009 to early 2013, that focused on enhancing the thermal conductivity due to introduction of nanostructures into phase change materials for thermal energy storage was discussed in this chapter. The main aim was to study the dependence of the enhanced thermal conductivity on mass fraction of the nanostructures and temperature for both liquid and solid phases. It is concluded that carbon-based nanostructures and carbon nanotubes generally exhibit far greater enhancement of thermal conductivity in comparison to metallic/metal oxide nanoparticle. However, great care should be taken in order to properly functionalize the nano-additives within PCM matrix to obtain well-dispersed NePCM colloids.

Table 2.1

Summary of utilized PCM and nano-structured thermal conductivity enhancers.

Authors (year)	PCM	Nano-structured materials		
	Materials and Properties	Materials and Properties	Dimensions, etc.	Fractions of enhancers
Gao et al. (2009)	n-hexadecane (n-$C_{16}H_{34}$) purity 99.5% T_m: 18 °C hog fat T_m: 25~30 °C	alumina (Al_2O_3) nanoparticles polydispersity: 0.124	mean diameter: 70 nm	0.5, 1, and 2 vol%[1]
Shaikh and Lafdi (2010)	paraffin wax	SWCNT, MWCNT	N/A	1 vol%
Ai et al. (2010)	stearic acid powder T_m: ~ 66.5 °C	zirconia (ZrO_2) nanopowders	mean diameter: 26 nm	23 wt%
Wang et al. (2011)	palmitic acid (PA) purity 98% T_m: 62.5-64 °C, ρ: 853 kg/m^3, L: 209,200 J/kg paraffin wax (PW) T_m: 48.2 °C, L: 142,200 J/kg	MWCNT (purity: 95%) treated by grafting of Oleylamine and Octanol tethers on surface	average diameter: 30 nm average length: 50 μm specific surface area: 60 m^2/g	0.5 wt%
Hu et al. (2011)	sodium acetate trihydrate (SAT) purity > 99%	aluminum nitride (AIN) nanoparticles purity> 99%	average size: 50 nm	0, 3, 4 and 5 wt%
Sanusi et al. (2011)	n-tricosane ($C_{23}H_{48}$) T_m: 54-58 °C , k: 0.2 W/mK (solid), L: 220,000 J/kg	graphite nanofibers (GNF) of herringbone type	diameter: 2~100 nm, length: ~ up to 100 μm	10 wt%
Zheng et al. (2011)	hexadecane ($C_{16}H_{34}$)	graphite flakes	average diameter: several μm	0.2, 0.5, 0.8, and 1 vol%

	T_m: ~18 °C		thickness: several nm ~ several tens of nm	
Teng et al. (2011)	paraffin wax	alumina (Al_2O_3) nanoparticles MWCNT	N/A	1, 2, and 3 wt%
Bayramoglu (2011)	n-octadecane T_m: 28 °C , ρ: 782.2 kg/m^3, L: 239,900 J/kg	MWCNT (purity: 95%)	outer diameter: 3~20 nm inner diameter: 1~3 nm length: 0.1~10 μm	1.25, 2.5, 5 and 10 wt%
Kalaiselvam et al. (2012)	60% n-tetradecane/40% n-hexadecane, capric/lauric acid, $CaCl_2$-$6H_2O$, n-octadecane, n-hexadecane and n-eicosane	aluminum and alumina (Al_2O_3) nanoparticles	N/A	0.07 vol%
Jesumathy et al. (2012)	paraffin wax (PW) T_m: 58.2 °C, L: 210,000 J/kg	copper oxide (CuO) nanoparticles	mean diameter: 40 nm	2, 5, and 10 wt%
Mare et al. (2012)	deionized water k: 0.6 W/mK, ρ: 998.2 kg/m^3, C_p: 4182 J/kgK	γ-Al_2O_3 nanoparticles k: 36 W/mK, ρ: 3880 kg/m^3, C_p: 773 J/kgK	diameter: 30 nm	1, 2, 3, and 4 vol%
Wu et al. (2012)	paraffin purity 99.99% T_m: 58~60 °C	Cu nanoparticles purity: 99.9%	diameter: 25 nm	0, 0.2, 0.5, 1.2 and 2 wt%
Kumaresan et al. (2012)	RT-20 paraffin T_m: 18~23 °C, T_f: 19~22 °C, ρ: 880 kg/m^3 (solid), 770 kg/m^3 (liquid), k: 0.2 W/mK, L: 134,000 J/kg	MWCNT	average diameter: 30-50 nm average length: 10-20 μm specific surface area: 60 m^2/g	0.15, 0.3, 0.45 and 0.6 vol%
Harikrishnan and Kalaiselvam (2012)	oleic acid ρ: 887 kg/m^3, C_p: 2043 J/kgK, L: 140,200 J/kg	CuO nanoparticles	diameter: 1-80 nm	0.5, 1, 1.5 and 2 wt%

Zeng et al. (2012)	tetradecanol (TD)	copper nanowires (Cu NWs)	N/A	0, 0.0625, 0.125, 0.745, 0.961, 1.43, 2.78, 4.75, 5.14, and 11.9 vol%
He et al. (2012)	deionized water	TiO_2 nanoparticles	average size: 20 nm	0, 0.3, 1.2 and 2.4 wt%
Teng et al. (2013)	paraffin (Fully refined)	MWCNTs Graphite	size: 20-30 nm (MWCNTs) and 3.2 μm (Graphite)	0, 1, 2 and 3 wt%
Shi et al. (2013)	paraffin T_m: 61.6 °C	exfoliated graphite nanoplatelets (xGnP), graphene purity 99.9995%	N/A	0, 1, 2, 5 and 10 wt%
Yu et al. (2013)	paraffin T_m: 58-60 °C	MWCNT (pristine and carboxyl-functionalized) purity> 95% and 97% graphite nanoplatelets (GNP) purity> 99% CNF purity> 95%	length: 0.5-2 μm and 5-15 μm (MWCNT), 10-30 μm (CNF), 5-10 μm (GNP) diameter: 8-15 nm and < 10 nm (MWCNT), 150-200 nm (CNF), 4-20 nm (GNP)	0, 1, 2, 3 and 4 wt%

[1] vol.% and wt.% stand for volumetric and mass fractions, respectively.

Table 2.2

Summary of preparation and characterization methods and instruments for studies of colloidal

dispersions utilized as nano-enhanced phase change materials (NePCM).

Authors (year)	Preparation		Characterization		Study of heat transfer	
	Methods	Dispersion and stabilization [1]	Thermal conductivity [2]	Other measurements and instruments	Stability concerns	
Gao et al. (2009)	two-step	Ultrasonication *surfactant*: Span 80	THW[3], SL-mT	DLS[4], TEM[5]	N/A	N/A
Shaikh and Lafdi (2010)	two-step	N/A	N/A	NFA[6]	N/A	TC[7] readings for melting experiments
Ai et al. (2010)	two-step	High-speed milling *surfactants*: Carbon tetrachloride, chloroform; D3021 to modify surface of zirconia particles	N/A	DTA[8], TEM, XRD[5]	N/A	temperature vs. time data of DTA tests
Wang et al. (2011)	two-step	Sonication	THW, SL-mT	DSC[9], FTIR[5], POM[10], TEM, XRD	visually observed, thermal stability test for up to 80 cycles of freezing/thawing	N/A
Hu et al. (2011)	two-step	N/A	N/A	DSC, OM[11], PSA[12], SEM[13], TG-DTA[14]	visually observed , thermal stability test for up to 50 cycles of freezing/thawing	TC readings for melting/freezing experiments
Sanusi et al. (2011)	two-step	Sonication	steady-state guided hot-plate method, S-1T	N/A	N/A	TC readings for melting/freezing experiments in a cubic cavity

Zheng et al. (2011)	two-step	Ultrasonication	THW, SL-mT	OM, SEM, TEM, XPS[15]	Thermal conductivity data during freeze/melt cycles proved reversibility	N/A
Teng et al. (2011)	two-step	Ultrasonication Electromagnetic agitation	N/A	TEM	N/A	TC readings for melting/freezing experiments in a tube
Bayramoglu (2011)	two-step	Ultrasonication	N/A	DSC, OM, TEM, TGA[5]	thermal stability test for up to 1440 cycles of freezing/thawing, followed by DSC and TGA analyses	N/A
Kalaiselvam et al. (2012)	two-step	N/A	N/A	N/A	N/A	TC readings for melting/freezing experiments
Jesumathy et al. (2012)	two-step	Ultrasonication	THW, SL-mT	DSC, viscometer	visually observed	TC readings for melting/freezing experiments in a cylindrical tube
Mare et al. (2012)	two-step	N/A	N/A	DLS	Observed agglomeration based on DLS data	TC readings for freezing experiments
Wu et al. (2012)	two-step	Ultrasonication *surfactant*: Hitenol BC-10	HotDisk thermal constants analyzer (TPS[16]), SL-mT	FTIR, ITC[17]	observed by consecutively heating and cooling the samples in the constant temperature trough of 70 and 30 °C for 100 cycles conducted by	N/A

					FIIR.	
Kumaresan et al. (2012)	two-step	Ultrasonication magnetic stirring	THW, SL-mT	DSC, RM[18], RTD[19]	visually observed	RTD readings during freezing experiments in copper cylindrical containers
Harikrishnan and Kalaiselvam (2012)	two-step	Ultrasonication	NFA, L-1T	DSC, DTA, TEM, TGA, XRD	visually observed , thermal stability test for up to 150 cycles of freezing/thawing	TC readings for melting/freezing experiments
Zeng et al. (2012)	two-step	Ultrasonication	HotDisk thermal constants analyzer (TPS), S-1T	DSC, SEM, TGA, XRD	N/A	N/A
He et al. (2012)	two-step	Supersonic oscillation *surfactant*: SDBS[20]	N/A	TEM	observed by TEM image	TC readings for freezing experiments
Teng et al. (2013)	two-step	Ultrasonication electromagnetic stirring high-speed homogenizer	N/A	DSC, FE-SEM[21], PEB[22]	visually observed	TC readings for melting/freezing experiments
Shi et al. (2013)	two-step	Sonication	HotDisk thermal constants analyzer	SEM, SM[23], TEM, XRD,	visually observed	N/A

			(TPS), SL-mT			
Yu et al. (2013)	two-step	Sonication magnetic stirring	THW, L-1T	AFM[24], DLS, RV[25], SEM, TEM	visually observed	N/A

[1] This column is only applicable to the two-step method.

[2] Under thermal conductivity column, SL-*x*T stands for S = solid phase, L = liquid phase, *x* =1 for single and m for multiple, T = temperature measurements.

[3] THW stands for transient hot wire method.

[4] DLS denotes dynamic light scattering technique.

[5] FTIR, TEM, TGA, and XRD stand for Fourier transform infrared spectroscopy, transmission electron microscopy, thermal gravimetric analysis, and X-ray diffraction, respectively.

[6] NFA denotes nanoflash analyzer.

[7] TC denotes thermocouples.

[8] DTA denotes differential thermal analysis.

[9] DSC stands for differential scanning calorimetry.

[10] POM denotes polarizing optical microscopy.

[11] OM denotes optical microscopy.

[12] PSA denotes particle size analyzer.

[13] SEM denotes scanning electron microscope.

[14] TG-DTA denotes thermogravimetric/differential thermal analyzer.

[15] XPS denotes X-ray photon spectroscopy.

[16] TPS denotes transient plane source technique.

[17] ITC denotes infrared thermal camera.

[18] RM denotes rheometer.

[19] RTD denotes resistance temperature detector.

[20] SDBS denotes sodium dodecylbenzene sulfonate.

[21] FE-SEM denotes field-emission scanning electron microscopy.

[22] PEB denotes precision electronic balance.

[23] SM denotes source meter.

[24] AFM denotes atomic force microscopy.

[25] RV denotes rotational viscometer.

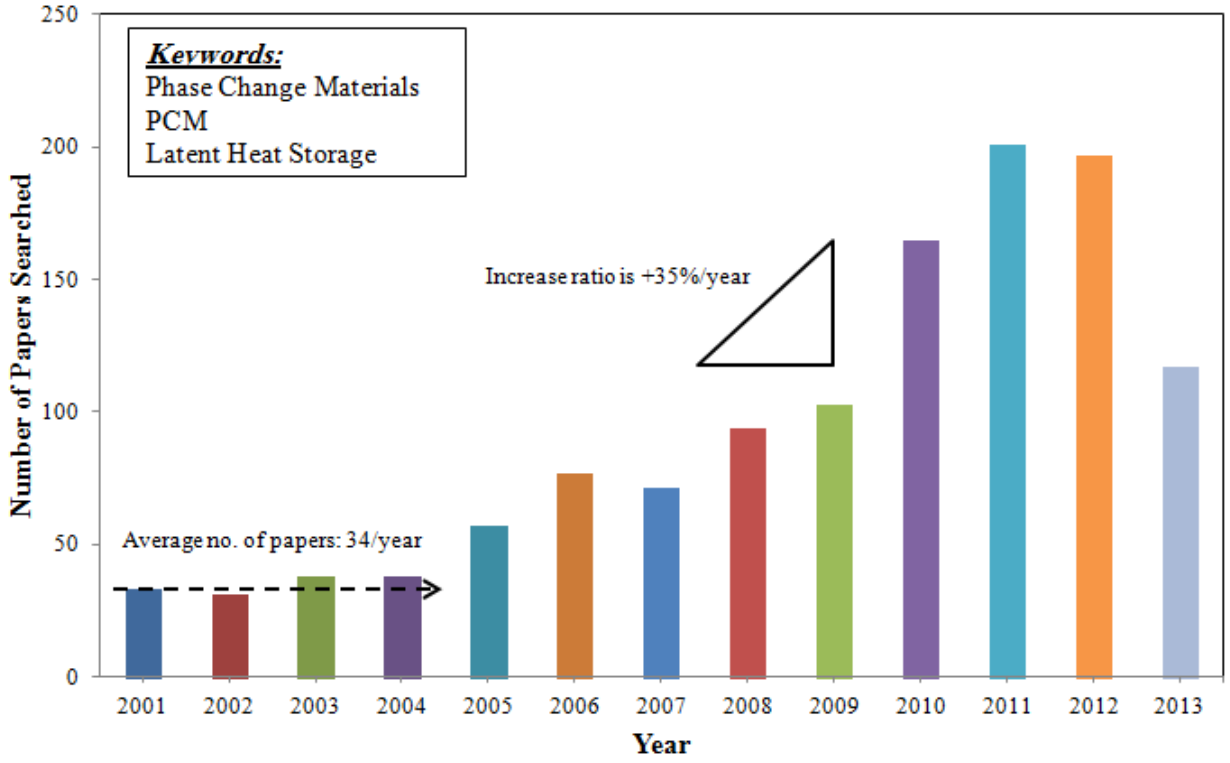

Figure 2.1 Year and number of PCM-related papers since 2001, using the search engine of the 'ScienceDirect' (search date: May 26, 2013)

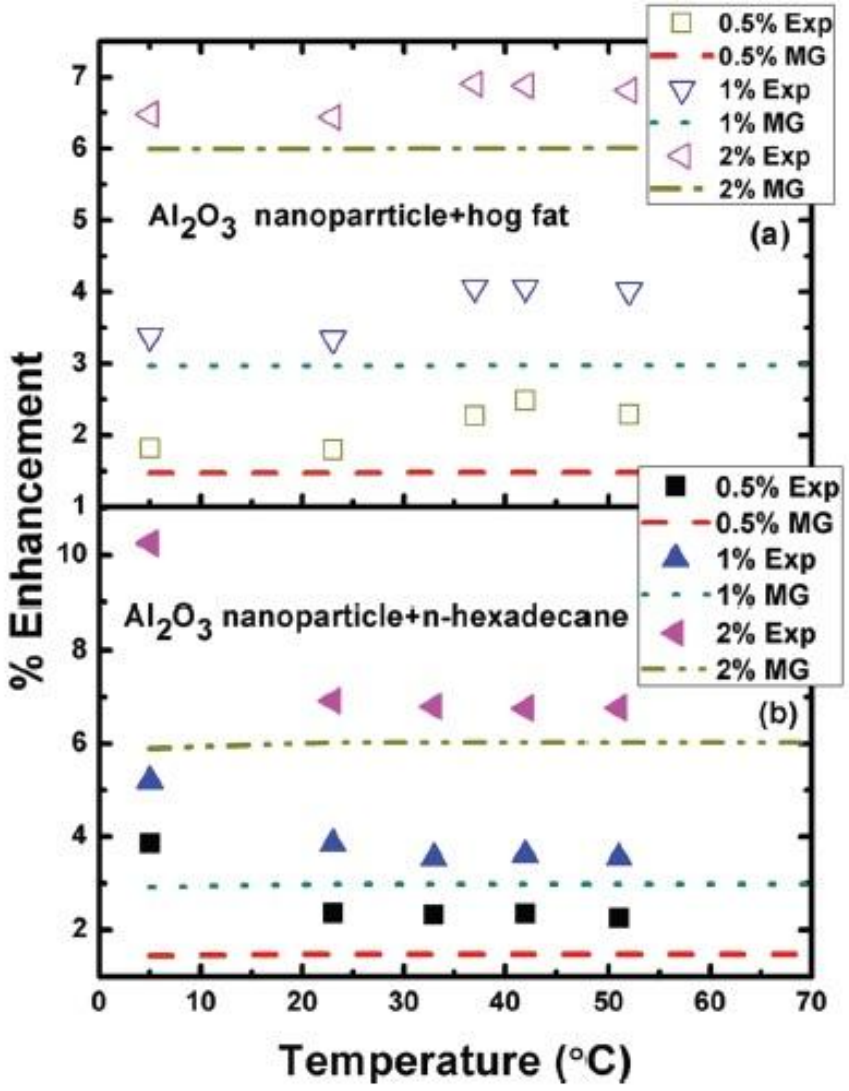

Figure 2.2 Temperature-dependent thermal conductivity enhancement of nanofluids using alumina nanoparticles dispersed in (a) hog fat and (b) hexadecane. Dots correspond to experimental data obtained using the THW method and the dashed lines are the predictions based on the Maxwell-Garnet model of well-dispersed spherical nanoparticles in the colloid (Gao et al., 2009)

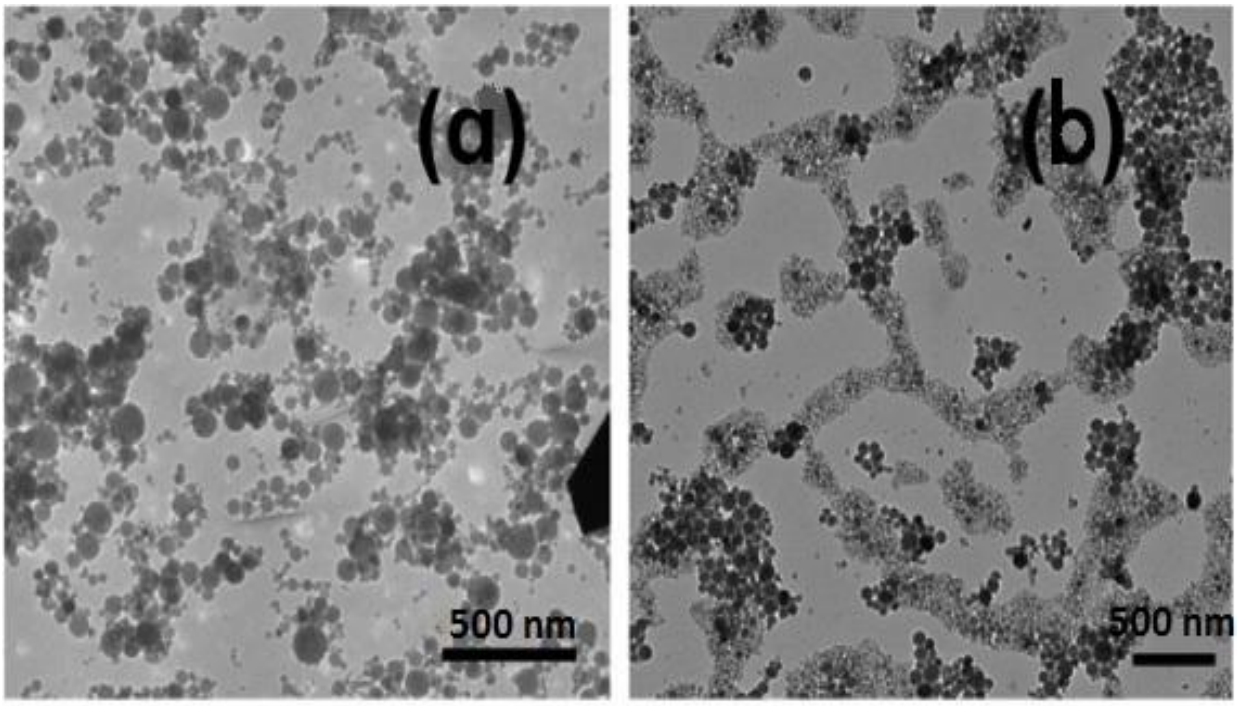

Figure 2.3 TEM images of (a) alumina/hexadecane suspension in liquid state and (b) solidified alumina/hexadecane colloid (Gao et al., 2009)

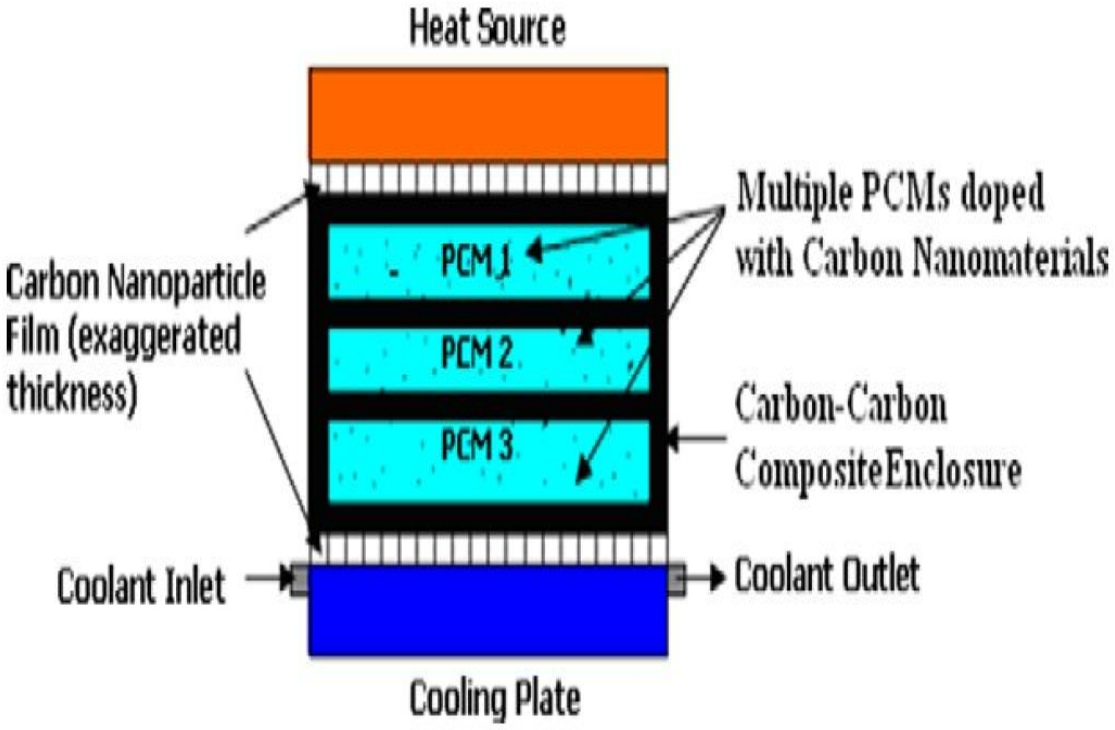

Figure 2.4 Composite 3-PCM thermal control system under varying power load (Shaikh and Lafdi, 2010)

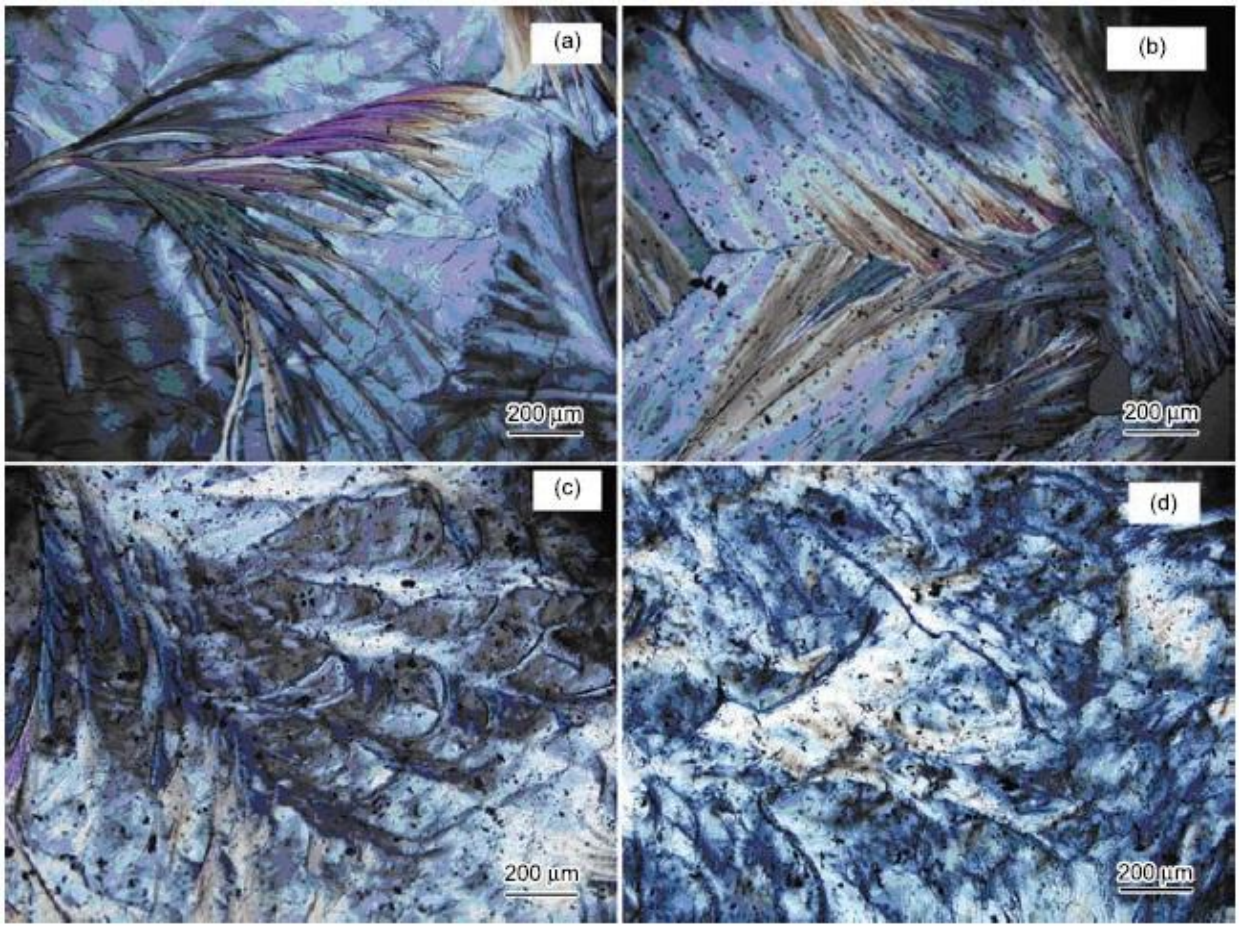

Figure 2.5 Polarizing optical microscopy (POM) images of (a) palmitic acid (PA), (b) P-CNT/PA, (c) G8-CNT/PA and (d) G18-CNT/PA colloids (Wang et al., 2011)

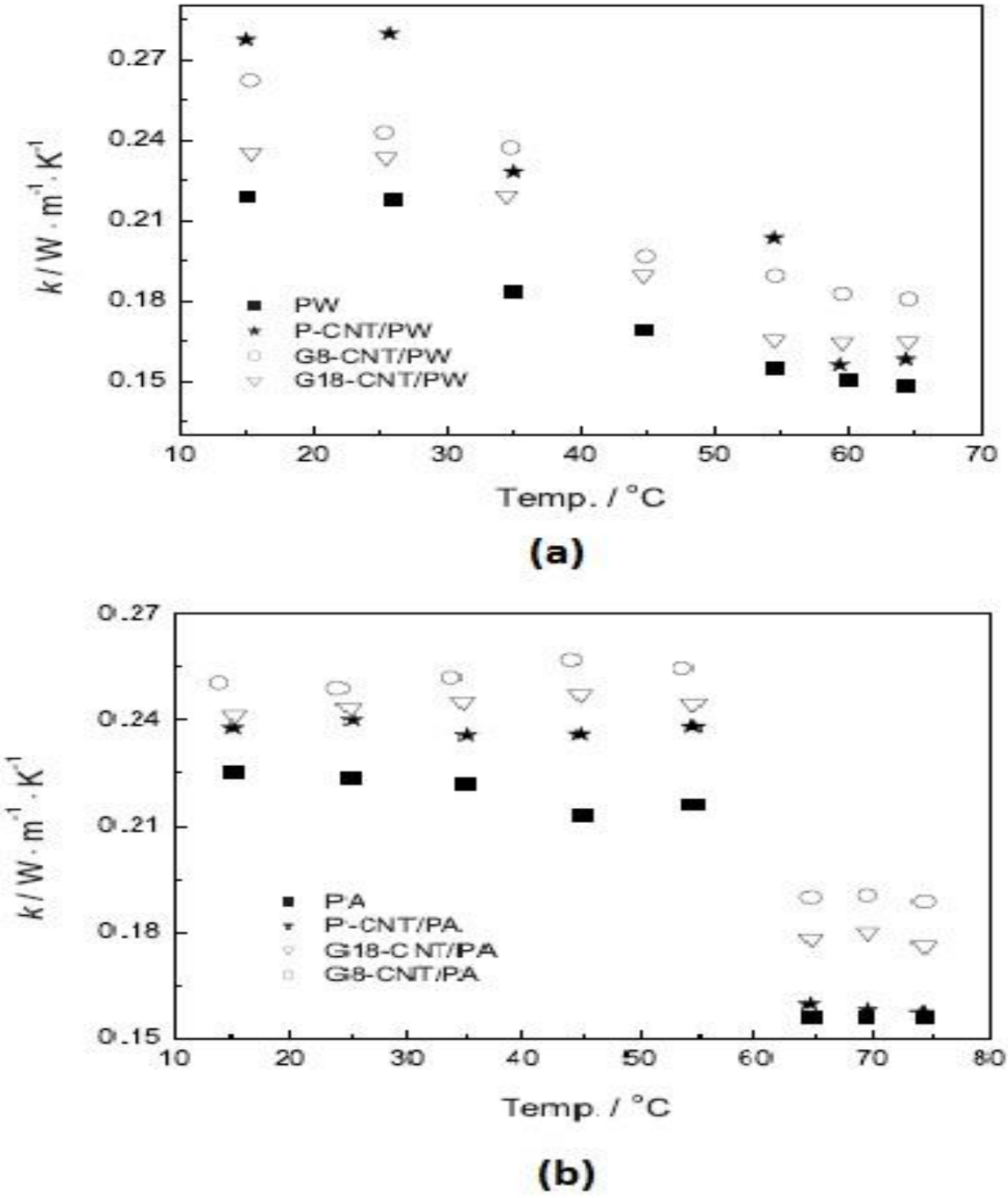

Figure 2.6 Measured thermal conductivity for CNT-enhanced (a) paraffin wax and (b) palmitic acid at various temperatures using the THW method (Wang et al., 2011)

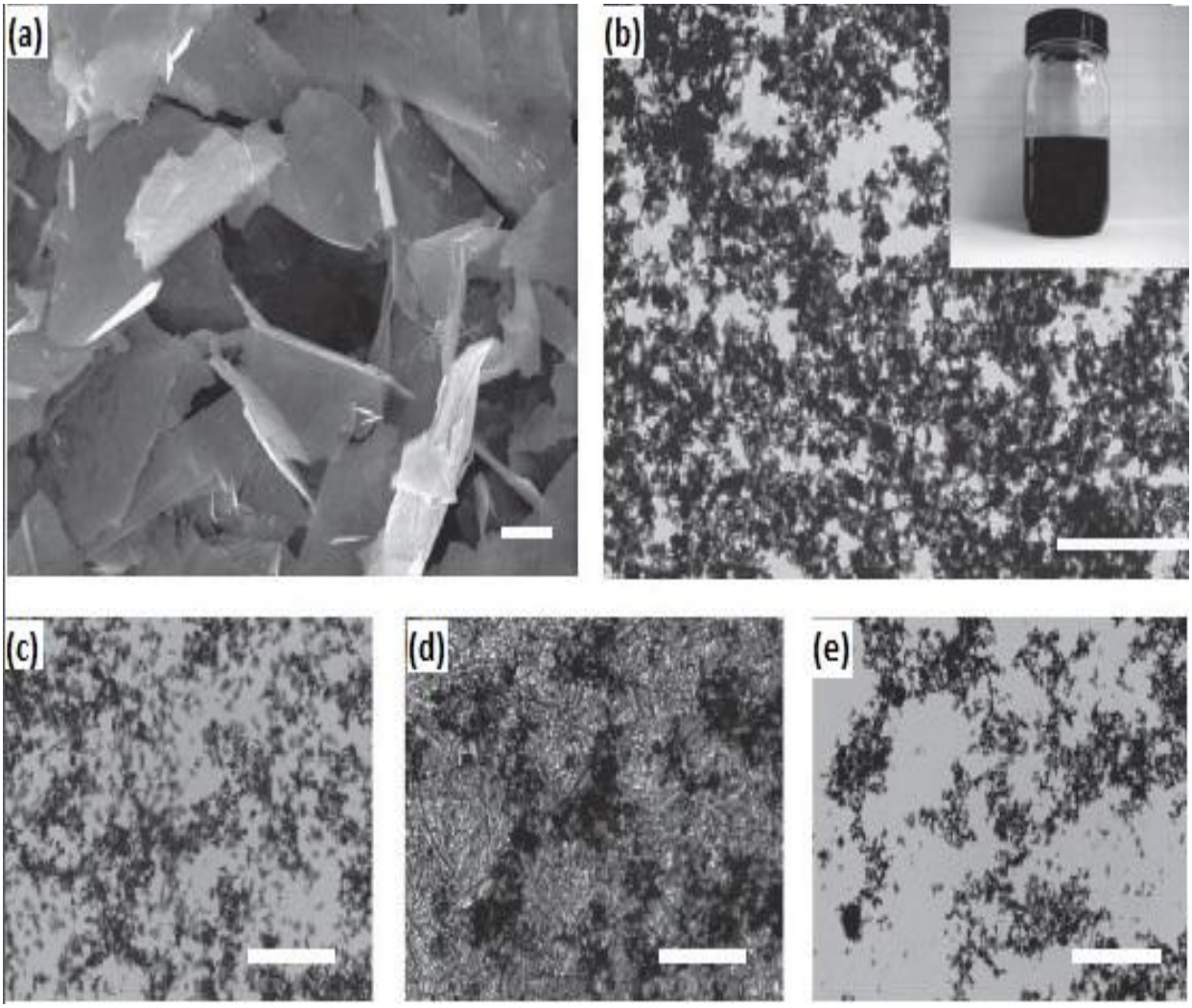

Figure 2.7 (a) SEM image of the graphite flakes prepared by a procedure of H_2SO_4 intercalation, microwave expansion and ultrasonic exfoliation of natural graphite. (b) Microstructure image of the 0.2 vol% graphite/hexadecane suspension observed using an optical microscope. Optical microscope images of the microstructure of (c) 0.05 vol% graphite/hexadecane suspension and (d) solidified graphite/hexadecane mixture with black areas being graphite clusters. (e) Graphite percolation network evident from an optical microscope image of a graphite suspension upon remelting. The respective scale bars were (a) 1 μm and (b-e) 200 μm (Zheng et al., 2011)

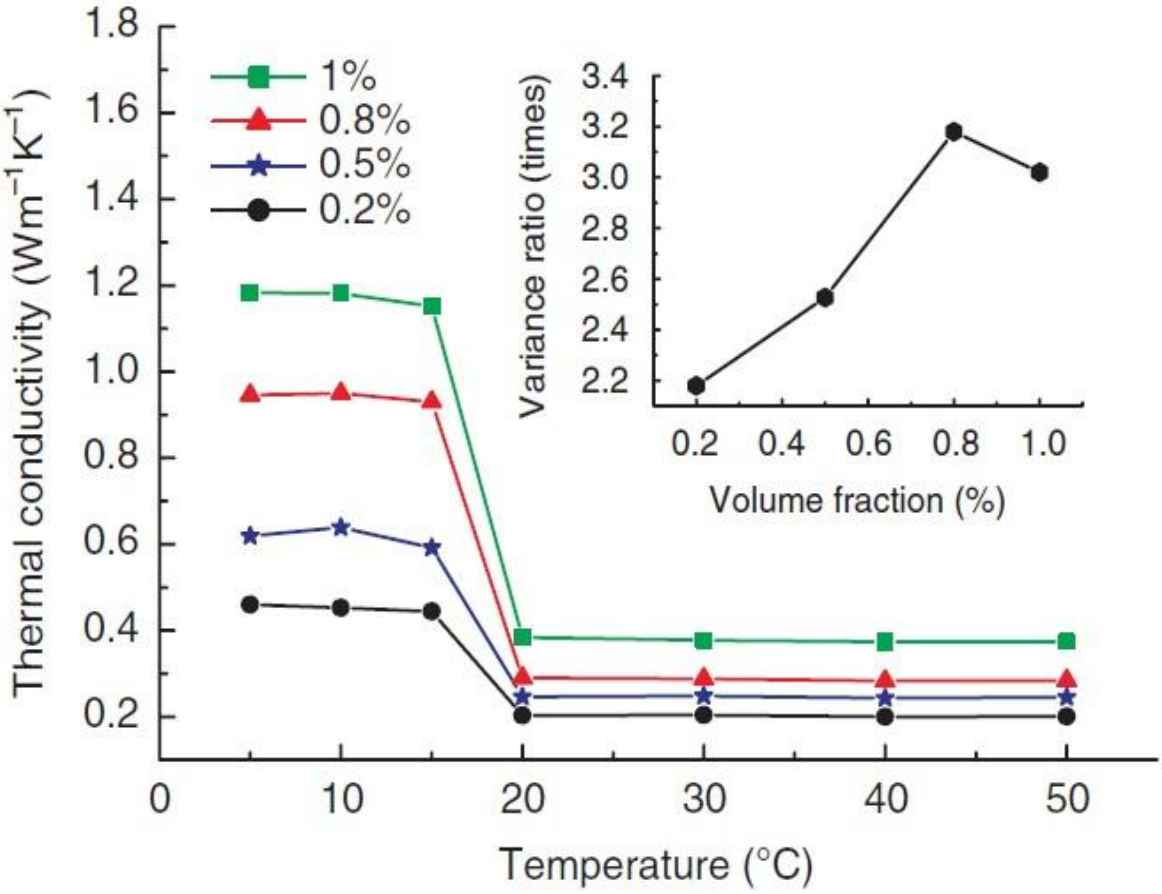

Figure 2.8 Temperature dependent thermal conductivity of graphite/hexadecane suspensions for different volume fractions of additives. The contrast ratio (ratio of thermal conductivity between the solid and liquid phases) as a function of graphite volume fraction is also shown in the inset graph (Zheng et al., 2011)

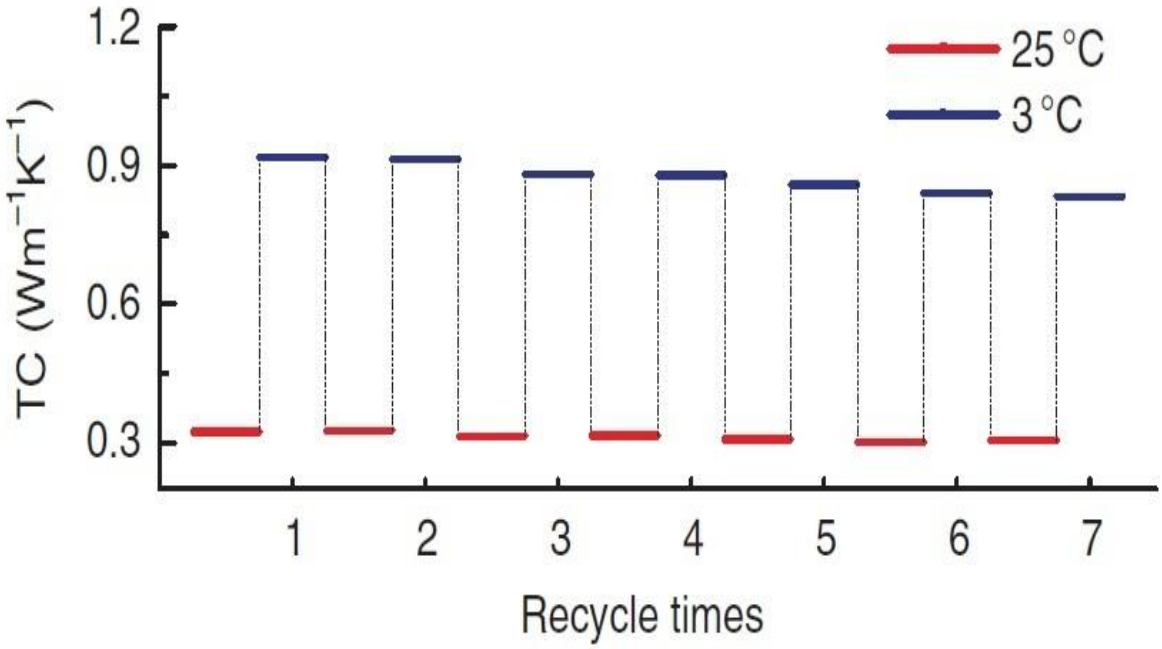

Figure 2.9 Thermal conductivity of 0.8 vol% graphite/hexadecane colloids after consecutive freeze/melt cycles. While blue lines show the thermal conductivity at 3 °C during the cycles, red lines indicate the thermal conductivity at 25 °C (Zheng et al., 2011)

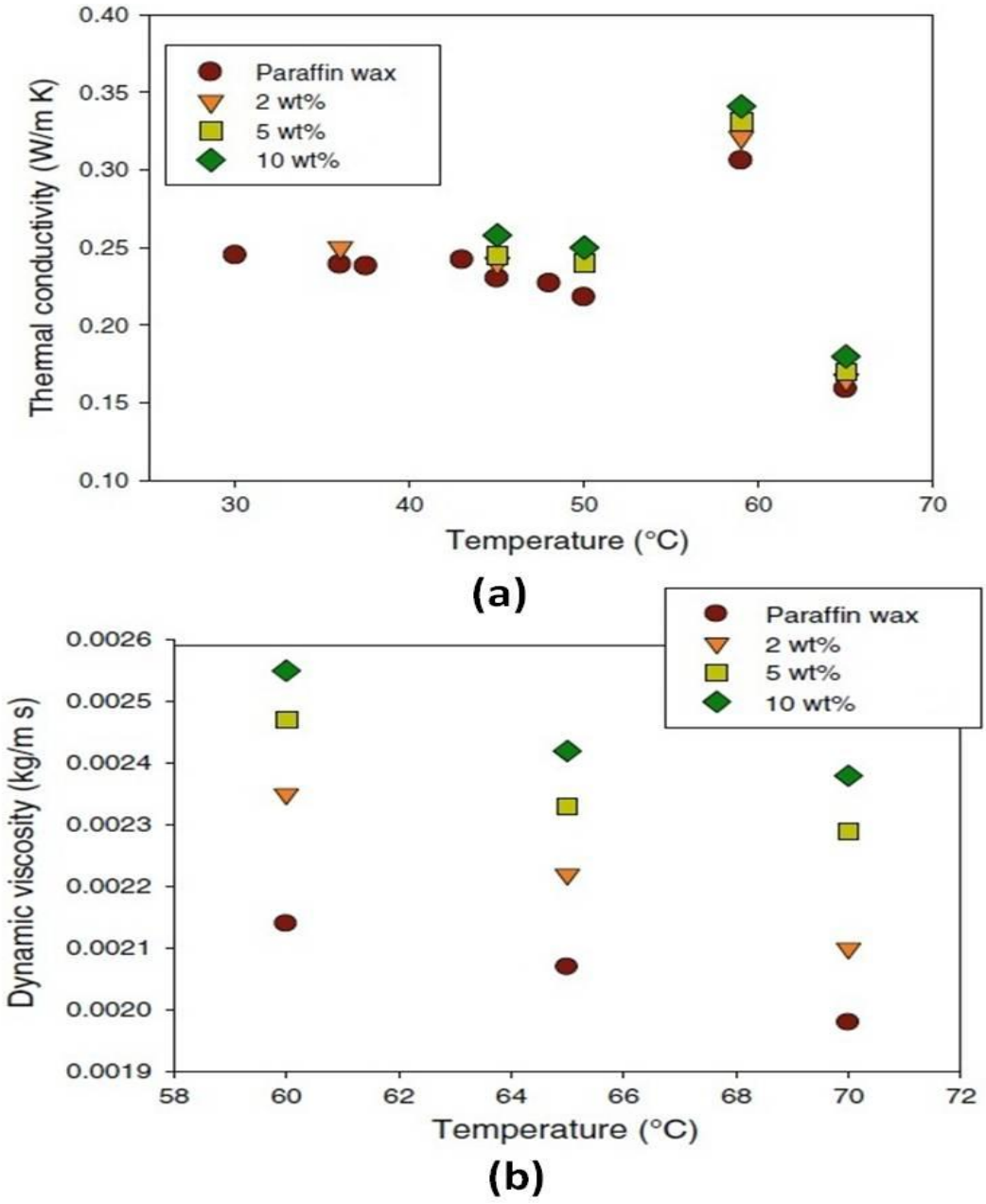

Figure 2.10 (a) Measured thermal conductivity and (b) Dynamic viscosity data for CuO nanoparticle-enhanced paraffin wax as a function of temperature and various loading of nanoparticles (Jesumathy et al., 2012)

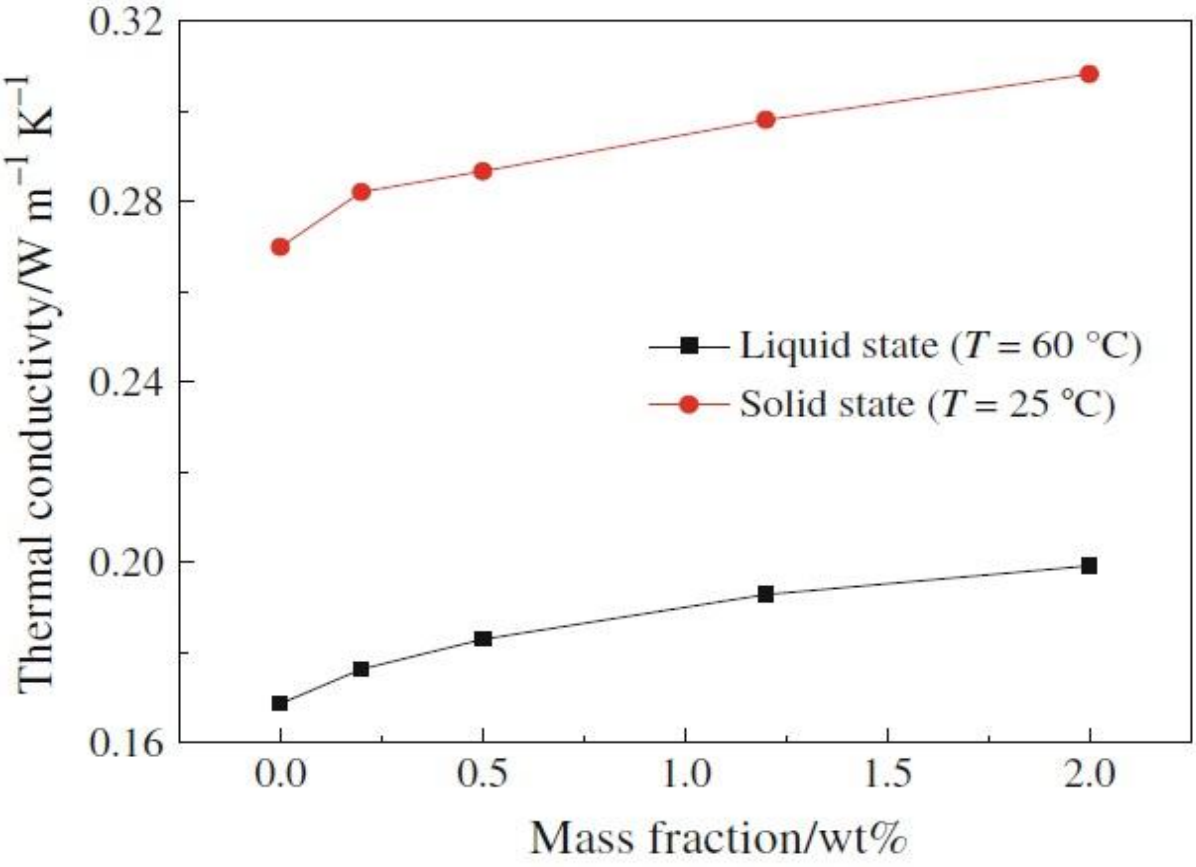

Figure 2.11 Resulted thermal conductivity values for Cu nanoparticle-enhanced paraffin in both liquid and solid phases as a function of mass fraction of loaded nanoparticles (Wu et al., 2012)

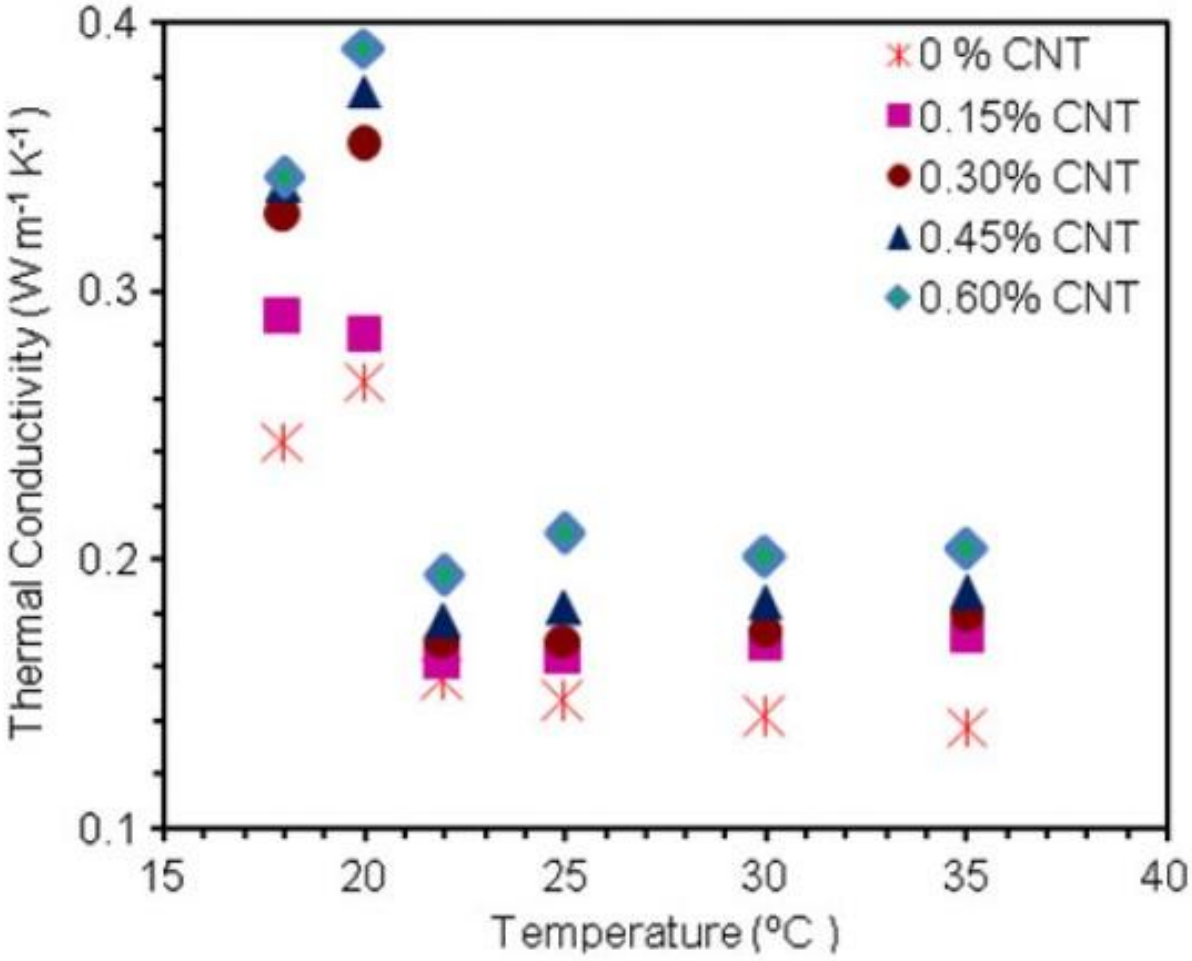

Figure 2.12 Thermal conductivity of nanofluid phase change materials (NFPCM) and pure PCM versus temperature (Kumaresan et al., 2012)

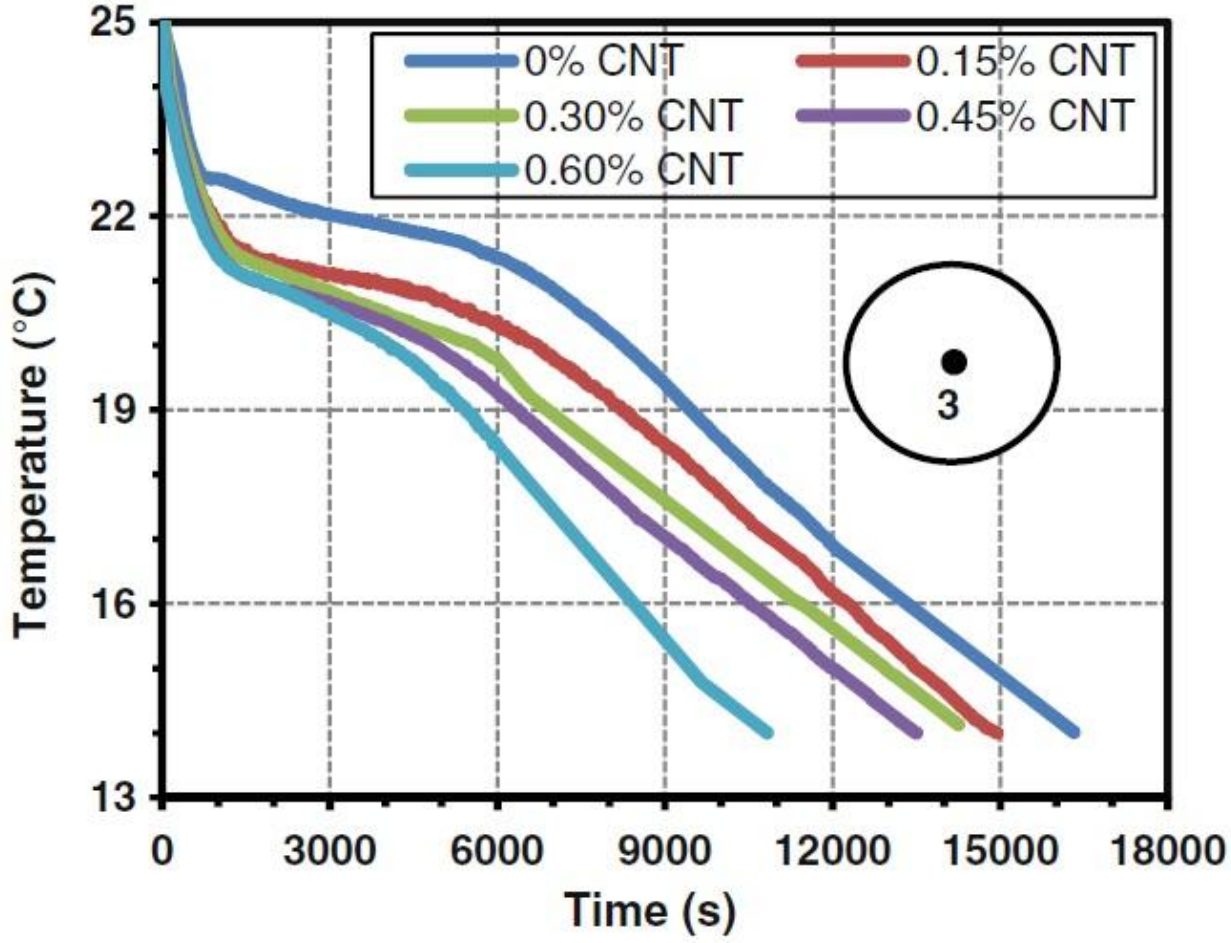

Figure 2.13 Solidification curves of nanofluid phase change materials (NFPCM) and pure PCM versus time (T_∞= 13°C) (Kumaresan et al., 2012)

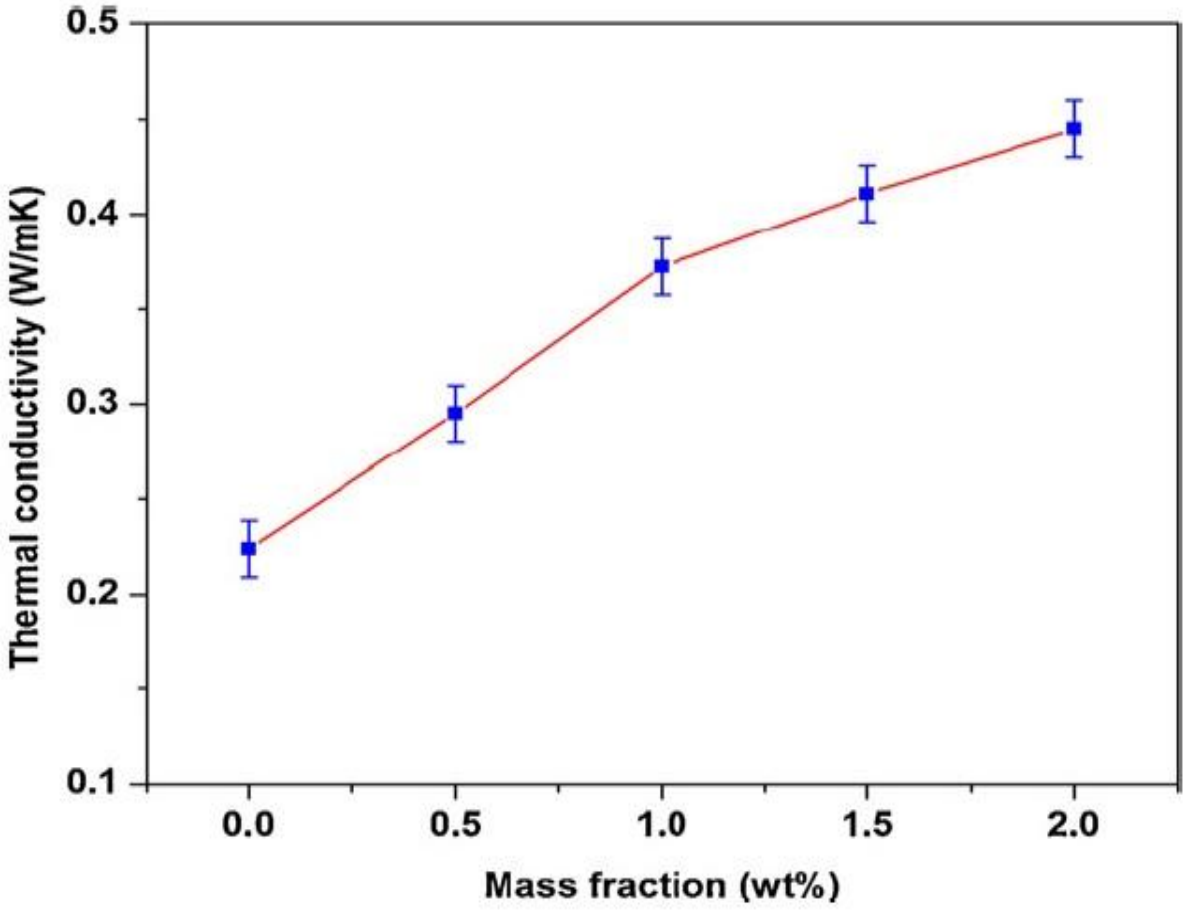

Figure 2.14 Measured thermal conductivity of CuO nanoparticle-enhanced oleic acid nanofluids as a function of various loading of nanoparticles (Harikrishnan and Kalaiselvam, 2012)

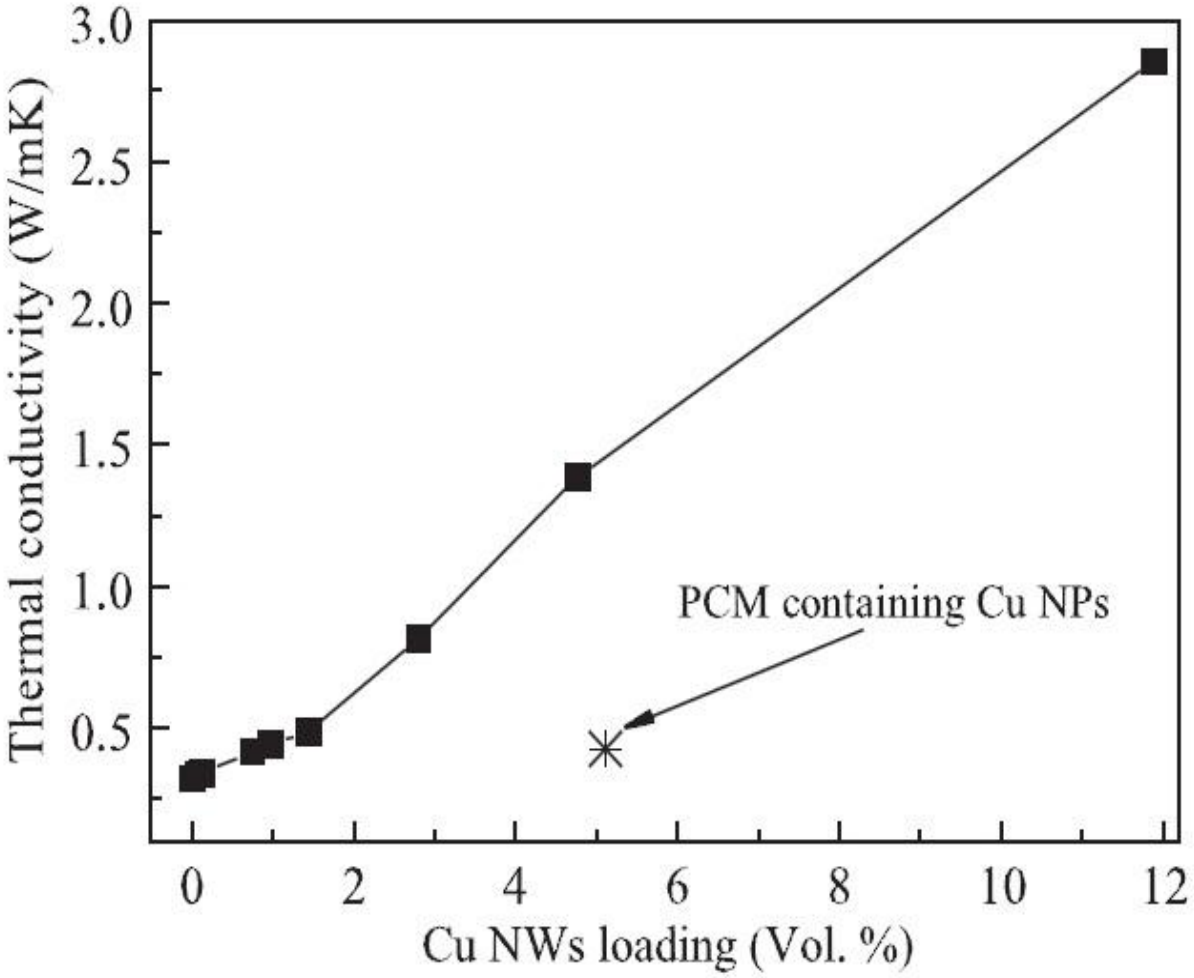

Figure 2.15 Measured thermal conductivity data of copper nanowire-enhanced tetradecanol as a function of various loading of nanowires at ambient temperature (Zeng et al., 2012)

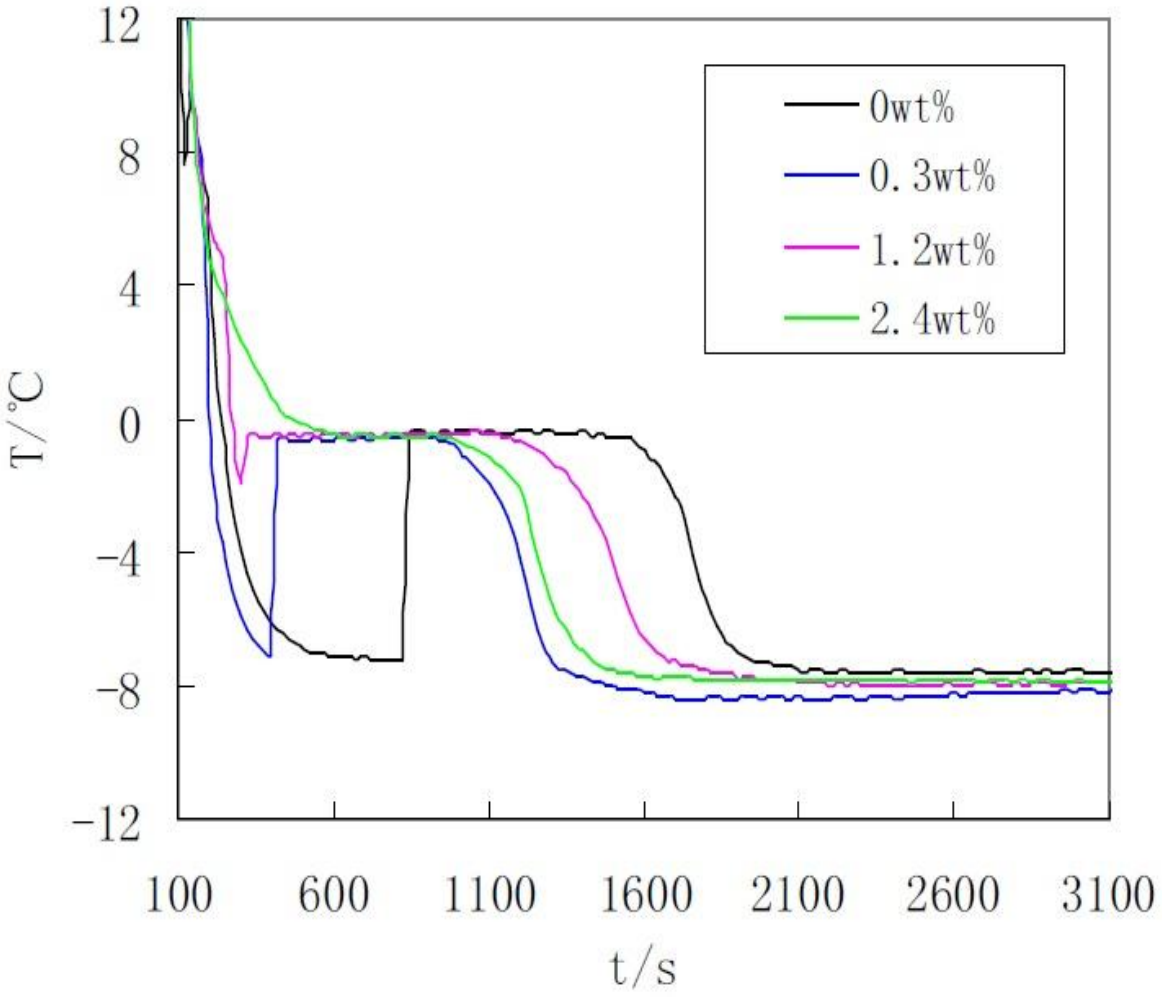

Figure 2.16 Solidification curves of water-based nanofluids and pure deionized water versus time for different TiO_2 mass fractions (He et al., 2012)

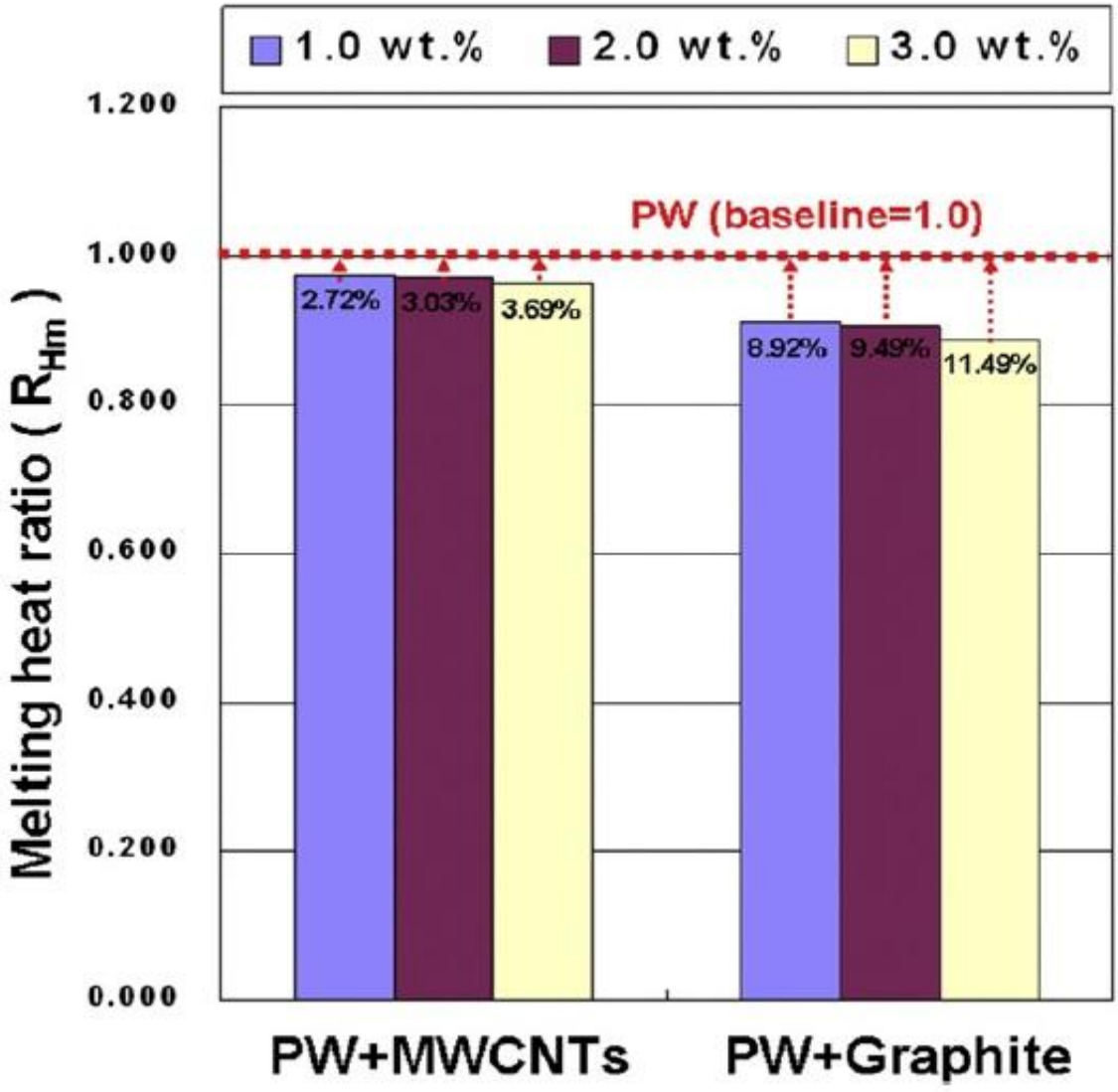

Figure 2.17 Column chart of the ratio of heat of melting for modified phase change materials (MPCMs) (Teng et al., 2013)

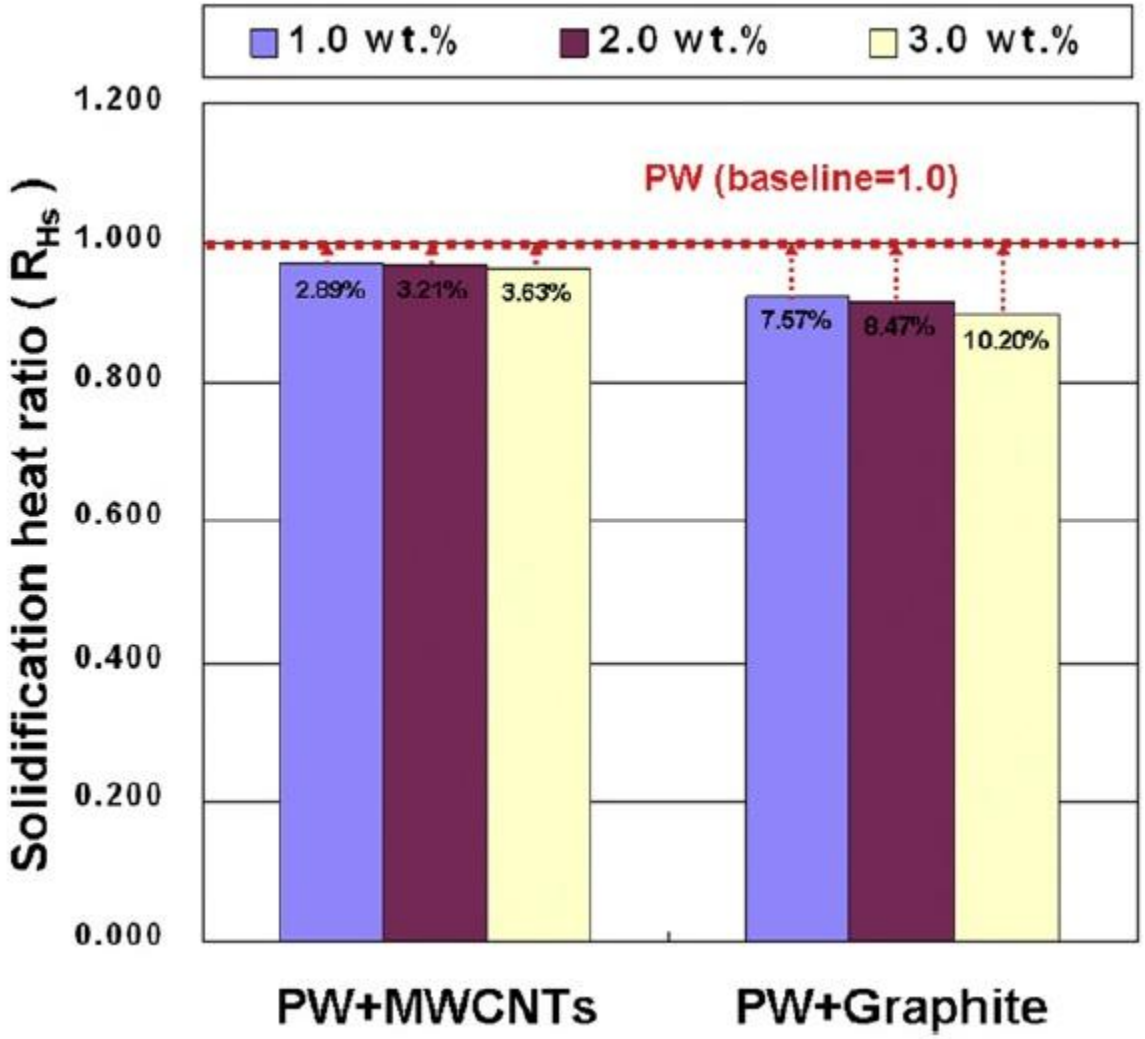

Figure 2.18 Column chart of the ratio of heat of solidification for modified phase change materials (MPCMs) (Teng et al., 2013)

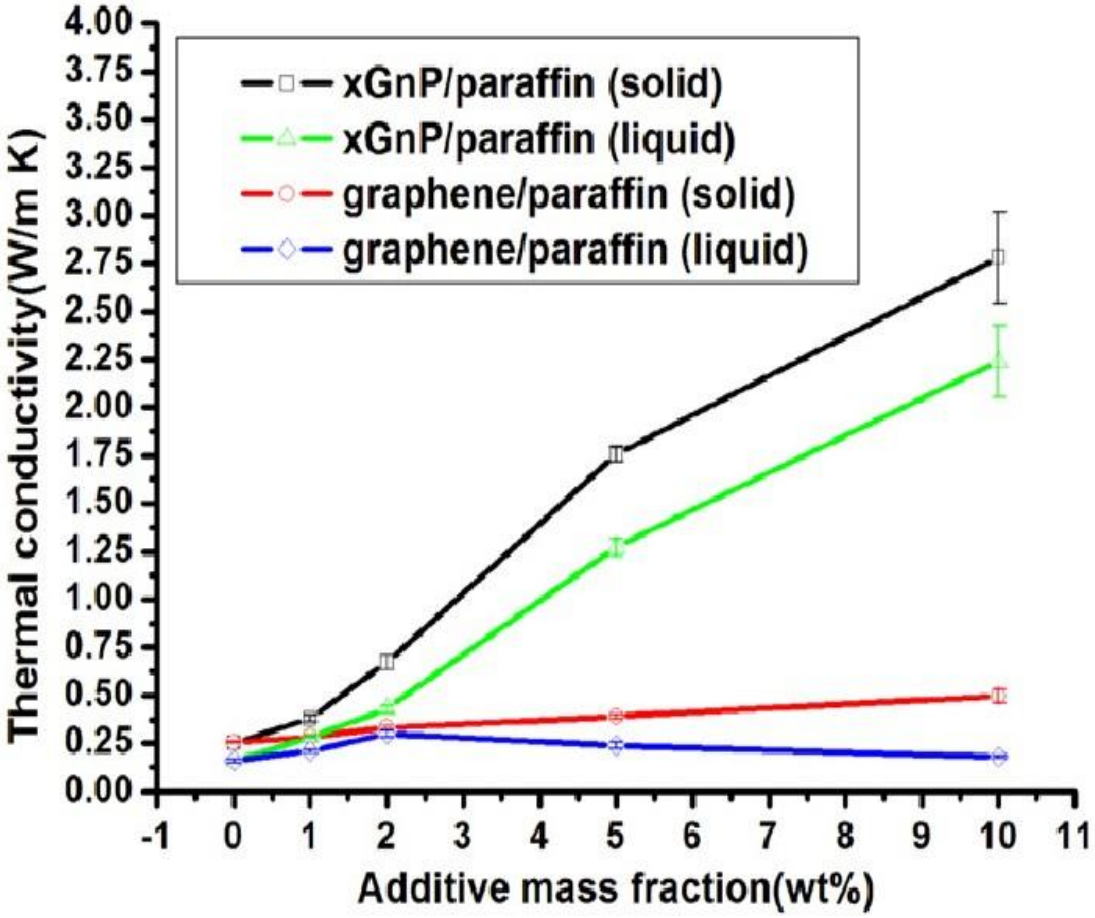

Figure 2.19 Measured thermal conductivity of nanoparticle-enhanced paraffin as a function of various loading of nanoparticles for both solid and liquid phases (Shi et al., 2013)

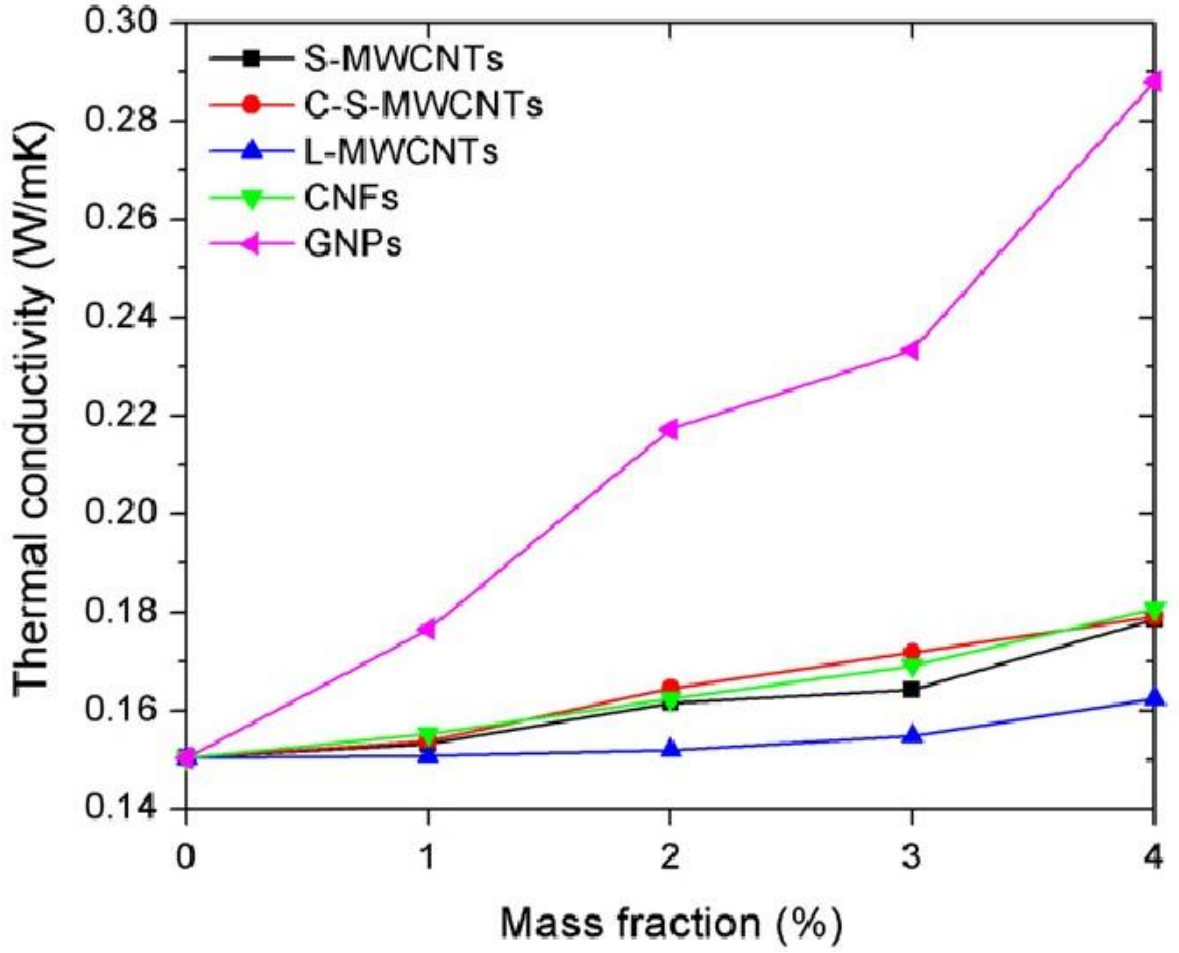

Figure 2.20 Thermal conductivity values of carbon-based nano-materials enhanced dispersed in liquid paraffin versus mass fraction of nano-fillers at 65 °C (Yu et al., 2013)

Chapter 3 Measurements of Thermal Conductivity of Solid Eicosane-Based NePCM

In this chapter, the effective thermal conductivity of solid composites made of eicosane as the base phase change material (PCM) plus copper oxide nanoparticles or MWCNT is studied experimentally. Thermal conductivity data was measured using the transient plane source (TPS) technique. At the beginning of the chapter, an introduction to the recent experimental efforts on thermal conductivity measurements of nanofluids is presented. Then, the preparation procedure of NePCM solid composites and the adopted instrumentation are explained in detail. Finally, the experimental data for each case is presented and discussed as a function of the mass fraction of the nano-additives and temperature.

3.1 Prior Research Studies on Thermal Conductivity Measurements of Nanofluids

Prior research effort on nanofluids (colloidal suspensions of nanoparticles) have focused on single-phase convective and liquid-vapor phase change (i.e. boiling) heat transfer (e.g. Das et al., 2008). Accordingly, experimental investigations of enhanced thermal conductivity of nanofluids have been mainly conducted for water- and ethylene-glycol-based nanofluids as

improved heat transfer fluids (Yu et al., 2009). In order to extend the applicability of these colloids, utilization of nanofluids as superior phase change materials (PCM) undergoing solid-liquid phase transition (i.e. solidification and melting) for thermal energy storage, referred to as nanoparticle-enhanced PCM (NePCM), was recently proposed by Khodadadi and Hosseinizadeh (2007).

Various organic and inorganic materials with high latent heat of fusion have been used as PCM for different thermal energy storage applications (Sharma et al., 2009), such as ice-water storage for thermal comfort in buildings, thermal management of electronic devices, industrial waste heat recovery, and solar thermal power generation. The proper PCM candidates for a specific application are usually chosen according to their melting/freezing points in regard to the desired temperature range. For example, alkanes (i.e. paraffin wax) with high carbon numbers have widely been used for the intermediate temperature range (0-100 °C). When it comes to high temperature applications (> 300 °C), molten salts have long been considered as the favored PCM candidates.

Since 2007, a number of experimental efforts have been devoted to preparation and characterization, as well as application of NePCM made of various combinations of base PCM and nano-structured additives, such as metal and metal oxide nanoparticles, single- and multi-walled carbon nanotubes, and metal and carbon nanofibers (Khodadadi et al., 2013). Among the 20+ such studies reviewed by Khodadadi et al. (2013), four of these investigations concerned combinations of nanoparticles and non-aqueous base PCM. Zeng et al. (2007) prepared and characterized PCM composites made of 1-tetradecanol (TD) enhanced by silver (Ag) nanoparticles with a wide range of particle loadings. Ho and Gao (2009) prepared NePCM made of n-octadecane ($C_{18}H_{38}$) and alumina (Al_2O_3) nanoparticles with two different mass fractions (5

and 10 wt%) and measured the important thermophysical properties. Phase change nanocomposites made of paraffin wax with γ-Al_2O_3 nanoparticles were prepared by Wang et al. (2010a) and the enhanced thermal conductivity was investigated in both solid and liquid phases. Wu et al. (2010) presented their experimental investigation on melting/freezing performance of paraffin enhanced by copper nanoparticles. Comparing to pure paraffin, faster melting and freezing rates by a factor of approximately 30% were observed for NePCM with 1 wt% nanoparticles. Fan (2011) recently reported experimental data on temperature-dependent thermal conductivity of CuO-based colloids in both liquid and solid phases using the Transient Plane Source (TPS) technique. It was observed that in the liquid phase, thermal conductivity of pure eicosane (melting temperature of 35.1 to 38 °C, according to various sources) decreased as the measurement temperature was increased and the enhancement of thermal conductivity due to presence of the additives varied monotonically as the particle loading was increased. The observed enhancement was slightly more marked with increasing temperature, probably due to improved diffusion of nanoparticles at high temperatures. In the range of the loading of nanoparticles studied (mass fractions less than or equal to 10 percent), the relative monotonic enhancement of thermal conductivity in the liquid phase was in good agreement with the predictions based on the model of Maxwell (1873). Considering the data for the solid phase composites, the first attempt of Fan (2011) to measure the thermal conductivity of a sample having solidified slowly from an initial temperature of 40 °C to 20 °C over a period of about 30 minutes while the sensor was submerged in the liquid gave rise to erratic information with high values of standard deviation (as high as 10 percent). Suspecting the greater degree of supercooling of eicosane and the long period of phase transition for the tested samples, Fan (2011) proceeded to measure the thermal conductivity of a rapidly-quenched composite. The

liquid composite was heated to 60 °C and then was poured into an empty cold glass sample container (kept at 10 °C) within which the TPS sensor was set in place. Despite improvements in the values of the standard deviation (less than 1 percent), a non-monotonic relation between the thermal conductivity and the mass fraction that was independent of the temperature range studied was exhibited, when the mass fraction was greater than 2 percent. The measured thermal conductivity values were generally insensitive to the measurement temperature (as observed for pure eicosane by Stryker and Sparrow, 1990) except the data that were obtained near the melting point (35 °C) that exhibited a sharp rise.

Considering the limitations of the experimental work of Fan (2011) having to do with lack of control over the phase transition, a new set of experiments were initiated in which solid samples were prepared following three different approaches, namely:

(i) ambient solidification,

(ii) ice-water bath solidification, and

(iii) oven solidification.

Specifics of these preparation routes for the samples will be discussed below along with results of a detailed temperature-dependent thermal conductivity data of eicosane/CuO solid composites.

The preparation procedure of the eicosane/MWCNT solid samples and preliminary thermal conductivity measurements of these samples are discussed in detail in section 3.5 of this chapter.

3.2 Preparation of the Eicosane-based NePCM Composites

Details of the preparation scheme of the NePCM liquid samples are discussed by Fan (2011). Similar steps were followed in the present study with deviations that will be outlined below. Eicosane ($C_{20}H_{42}$) that possesses a melting point of approximately 37 °C at the atmospheric pressure was selected as the base PCM. Copper (II) oxide (CuO) nanoparticles stabilized by sodium oleate ($C_{18}H_{33}O_2Na$) were synthesized and provided by chemist colleagues (Clary and Mills, 2011). It was shown that the CuO nanoparticles were nearly spherical and most of them had a diameter within the range of 5 to 15 nm (Clary and Mills, 2011). The NePCM samples with eight different mass fractions (0, 1, 2, 3.5, 5, 6.5, 8 and 10 wt%) of nanoparticles were prepared by dispersing the desired amounts of CuO nanoparticles into 99% pure eicosane (Sigma-Aldrich, St. Louis, MO) in liquid phase followed by rigorous stirring on a hot-plate magnetic stirrer (SP131325Q, Thermo Fisher, Dubuque, IA) at 80 °C for 30 minutes. A representative photo of five sample colloids with different mass fractions is shown in Figure 3.1 (Fan, 2011). Although it is seen that more nanoparticles tend to stick on the walls with increasing particle loading, no significant precipitation was visually found at the bottom of the containers, even for the most concentrated 10 wt% sample. Desirable long-term stability of NePCM samples prepared using the sodium-oleate-stabilized CuO nanoparticles in various alkanes (hexane, octane, dodecane, and eicosane) was studied by observing the absorbance spectra for mass fractions up to 20 wt% (Clary and Mills, 2011). In the calculation of the required mass of nanoparticles for each concentration, it was assumed that CuO nanoparticles are pure and the

presence of sodium-oleate surfactant was ignored. There is no data in the literature corresponding to the exact density of CuO nanoparticles. Thus, the density of bulk CuO, i.e. 6,315 kg/m^3 (Fan, 2011) is adopted in these sets of calculations. The liquid and solid densities of eicosane are $\rho_l = 789\ kg/m^3$ and $\rho_s = 840\ kg/m^3$, respectively.

Upon preparation of the liquid samples, appropriate amount of colloids were immediately poured into custom-fabricated molds and the batch of the samples were placed inside a vacuum oven (Fischer Scientific, Isotemp® Vacuum Oven Model 281A) for at least 20 hours. The vacuum oven (Figure 3.2) was operated at -40 kPa gage at a set temperature of 65 °C in order to degas the samples. The aluminum molds were machined disks with a diameter of one inch and height of 0.375 inches. Before pouring the colloid samples, commercial aluminum foil molds (VWR® International LLC., Model 611-1362 shown in Figure 3.3) with a diameter of 1 inch was pressed into the machined aluminum molds using a custom-designed molding handle (Figure 3.4). Upon removing the samples from the oven, phase transition of the liquid samples was realized by subjecting them to one of three procedures that follow. One batch was allowed to solidify at the ambient temperature of the laboratory. The second batch was prepared by placing the metallic tray that supported the molds in the oven directly in contact with an ice-water bath. The third batch was left in the oven to solidify under no vacuum (ambient pressure) while the oven was turned off. Thus, three distinct batches were obtained that differed only in their phase transition routes. Upon completion of solidification (at least 5, 30, and 240 minutes for the ice-water bath, ambient temperature and oven solidification methods, respectively), the samples were easily removed from the aluminum foil molds. A photograph of the pure and 1 wt% composite samples prepared following the ice-water bath solidification scheme is shown in Figure 3.5. For each particle concentration, a pair of samples was available for testing.

Generally, the side of each sample that was in contact with the bottom of the mold (e.g. lower disks of Figure 3.5) was flatter compared the opposite side (e.g. coarse upper disks of Figure 3.5) that was exposed to the local ambient atmosphere and experienced surface tension effects. Given the variation of surface morphology for each sample and considering the strict requirement of the adopted TPS theory in relation to assuring tight contact of the sensor with both disks, it was decided to use fine sand papers in order to smoothen the flatter sides of sample disks further. Thus, different grades of sand paper (starting with grade 300 and finishing with grade 400) were used. Possible thermal contact resistance issues between the samples and the TPS sensor will be discussed below. Despite the shortcoming associated with working with two non-identical samples for each test, it was assured that an appropriate probing depth required by the TPS theory was available for a given test. The weight of each sample was in the range of 3-4 grams. A brief overview diagram containing the descriptions of the preparation schemes is shown in Figure 3.6.

3.3 Thermal Conductivity Measurements

There are two main classes of methods to measure the thermal conductivity of a material depending on its type, form, and state, namely the transient and steady-state methods. Transient methods can be rapidly applied to the test specimen and measure thermal conductivity value within a few minutes. However, utilizing steady-state methods of measuring thermal conductivity, e.g. heat flow meter and guarded hot plate techniques, it is necessary to wait for a long period of time in order to provide a thermally-stable gradient over a testing sample. The

theory and physical principles of the transient and steady-state methods of measuring thermal conductivity are discussed in detail by Wakeham and Assael (1999).

The commonly-used transient methods of measuring thermal conductivity mainly consist of the transient plane source (TPS), transient hot wire (THW) and laser flash techniques. Owing to their ability to measure thermal conductivity relatively fast, the transient methods are especially suitable for liquid samples to avoid undesirable natural convection effect on thermal conductivity data. That is why many researchers, e.g. Wang et al. (2008, 2009, 2010a, and 2010b), have chosen to utilize these techniques for liquid-state NePCM and nanofluids.

3.3.1 Instrumentation, Theory and Experimental Details

Thermal conductivity of the NePCM samples was measured by utilizing a Hot Disk Thermal Constants Analyzer (TPS 500, Hot Disk AB, Gothenburg, SWEDEN) (Figure 3.7) based on the transient plane source technique (maximum uncertainty of 2% specified by the manufacturer). This instrument offers rapid means of measuring the thermal conductivity with the measurement time being as short as 2.5 sec.

The range of applicability and other main specifications of the TPS 500 apparatus are given in Table 3.1. The instrument can be utilized to measure thermal conductivity of solids as well as liquids and powders. For hydrocarbon-based NePCM, thermal conductivity values are about 0.1 W/mK and the TPS instrument is a proper candidate to be utilized (Table 3.1). The theory and data reduction procedures of the TPS technique were thoroughly outlined by Gustafsson (1991), Gustavsson et al. (1994) and in the ISO Standard (ISO 22007-2:2008). The TPS theory is briefly discussed below. A double-spiral-shaped hot disk (made of Nickel coated

with Kapton as shown in Figure 3.8) with an outer radius of r, serves as a planar heat source and temperature response sensor. The outer radius of the utilized TPS 500 sensor in this study is 3.189 mm.

The TPS sensor is made of Nickel (Ni) with a thickness of 10 μm, and is coated with thin supporting chemically-resistant layers of Kapton (polyimide). While the sensor acts as a planar heat source thus increasing the temperature of the sample, it also serves as a resistance thermometer to record the transient temperature rise versus heating time. As the TPS theory implies for testing solid samples, the sensor should be sandwiched between two identical infinitely-large samples. This is the basic assumption of the TPS technique. In other words, it is assumed that the released "thermal wave" from the TPS sensor during the heating time should not reach the outer boundaries of the test specimen. Therefore, a parameter called the "thermal penetration depth" is defined and estimated in the instruction manual (ThermTest Inc., Fredericton, New Brunswick, CANADA) as:

$$d = 2\sqrt{\alpha t}\,, \tag{3.1}$$

where α and t stand for the thermal diffusivity of the sample and total heating (measurement) time, respectively.

In response to heating, $R(t)$, the electrical resistance of the sensor as a function of time, is given as

$$R(t) = R_0\{1 + \kappa[\Delta T_K + \Delta T_{avg}(\tau)]\}\,, \tag{3.2}$$

where $R_{0,}$ κ, ΔT_K, and $\Delta T_{avg}(\tau)$ stand for initial resistance value at $t = 0$, temperature coefficient of resistance (TCR), constant temperature difference between the two sides of the Kapton layer, and the average temperature rise of the sample surface, respectively.

Re-ordering the equation (3.2), it takes the form

$$\Delta T_K + \Delta T_{avg}(\tau) = \frac{1}{\kappa}\left[\frac{R(t)}{R_0} - 1\right], \tag{3.3}$$

which accounts for the recorded temperature increase by the TPS sensor.

Ideally, if a perfect thermal contact is achieved between the TPS sensor and the sample surface, the value of ΔT_K will be equal to zero. However, in real-world applications after a very short time Δt_K, ΔT_K becomes a constant value. Under this condition, Δt_K can be obtained by

$$\Delta t_\kappa = \frac{\delta_\kappa^2}{\alpha_\kappa}, \tag{3.4}$$

where δ_κ is the thickness of the Kapton layer and α_κ is the thermal diffusivity of the Kapton material. Relation (3.4) corresponds to the Fourier number being equal to unity which means that the diffusive heat transport rate through the medium is equal to the heat storage rate in the medium.

The relationship between the average temperature rise of the sample surface $\Delta T_{avg}(\tau)$, and the thermal conductivity of the sample (k) is given as

$$\Delta T_{avg}(\tau) = \frac{P}{\pi^{3/2} r k} D(\tau), \tag{3.5}$$

where P, r and $D(\tau)$ denote total output power of the TPS sensor, outer radius of the sensor and a dimensionless function of time, respectively. $D(\tau)$ is a complicated function of time which

includes integral terms of the Bessel function (Gustafsson, 1991). The dimensionless time is introduced as

$$\tau = \sqrt{\frac{\alpha t}{r^2}}, \tag{3.6}$$

where α and t stand for thermal diffusivity of the sample and total heating (measurement) time, respectively.

There is a linear relationship for $\Delta T_{avg}(\tau)$ as a function of $D(\tau)$ as it is shown in equation (3.5). Therefore, by fitting a linear curve to its plot, both $P/\pi^{3/2}rk$ (slope) and ΔT_K (intercept) will be obtained simultaneously. A number of data points at the beginning of the temperature recording must be discarded in order to exclude the noisy information during the initial measurement time period (Δt_K). Thus, knowing the radius of the TPS sensor and the output power, thermal conductivity of the testing sample is easily extracted.

Great care should be taken to ensure that the necessary relaxation time period between consecutive measurements is considered and the sample reaches thermal equilibrium with the environment. This period should be greater than 36 times of the heating (measurement) period, as recommended by the manufacturer. It is noted that although thermal conductivity and diffusivity could be obtained simultaneously in TPS measurements, the data on thermal diffusivity of NeCPM samples that are of less interest will not be presented in this chapter.

The performance of the thermal constants analyzer was tested with deionized water at room temperature (21 ± 1 °C). Two set of tests (ten runs) were carried out on different occasions. The thermal conductivities were determined to be 0.5971 W/mK ± 0.36% and 0.6012 W/mK ± 0.50%. These values were both in excellent agreement with the well-established quantity of 0.6

W/mK. The accuracy and reproducibility, 5 and 2% respectively, of the instrument specified by the manufacturer were verified. Another benchmarking study was carried out with stainless steel disks at room temperature. Ten runs were performed and the thermal conductivity was equal to 13.76 W/mK ± 1.2%, while the actual value provided by the company was 13.85 W/mK which again verifies the accuracy and reproducibility of the TPS instrument. Given the availability of a pair of eicosane-CuO solid composites for each particle loading, a support set-up (Figure 3.9) for holding the two samples, while sandwiching the delicate TPS sensor during the tests, was designed and fabricated. The sanded sides of the two solid disks were positioned on a pair of aluminum cold plates (LYTRON Co., Woburn, MA, Model CP20G01) (Figure 3.10), whereas flow inlets and outlets of the cold plates (I.D. of 5/16 inches and O.D. of 3/8 inches) were connected to a bath/circulator. The programmable temperature bath (TC-502P, Brookfield, Middleboro, MA) (Figure 3.11 (a)) was utilized to circulate a 50:50 water/ethylene glycol solution as the working fluid at a constant temperature through the two cold plates. The bath system has an stability of 0.01 °C allowing the user to control the measurement temperature of interest within the bath. Owing to the internally criss-crossed finned structure of the aluminum cold plates, the cold plates can be adjusted rapidly to the temperature of the bath. The sample-holding assembly was insulated effectively from the laboratory environment using Styrofoam® sheets. An adjustable screw was used on top of a compression metal plate to impose a uniform pressure on the sample-holding assembly. Two adjustable screws on the sides of the set-up in addition to an adjustable metal plate were utilized to precisely adjust the horizontal level of the TPS sensor between the solid samples as recommended by the manufacturer. In order to monitor the sample temperature as accurately as possible with the current set-up, a thermistor (GE, Model A733F-CSP60BT103M, accuracy of 0.01 °C) (Figure 3.11 (b)) that was touching the surface of

the top aluminum cold plate was also employed. Upon gaining experience with this newly-designed set-up, the temperature reading of the thermistor was used as the reporting temperature of the samples in this chapter. At each measurement temperature, thermal equilibrium in the samples was assured by waiting for 90 minutes after the thermistor had reached the set point. Since the TPS sensor registers the temperature rise of the sample upon heating, using the temperature of the thermistor to report the measurement temperatures involves certain inaccuracies. Thermal conductivity measurements were performed in 5 °C increments for the 10-30 °C temperature range. Above 30 °C, measurements were obtained at 32, 33, 34 and 35 °C in order to provide detailed information near the melting point (37 °C).

Typical temperature rise vs. time data that were obtained by the TPS sensor for the case of pure eicosane samples are shown in Figure 3.12a. These measurements were obtained for thermistor readings of 10, 20 and 35 °C. Such data that were collected over a time period of 2.5 s are used by the TPS unit to determine the thermal conductivity of the samples.

3.3.2 Effect of Contact Resistance on Thermal Conductivity Measurements

In order to study the effect of thermal contact resistance on thermal conductivity measurement results, a set of experiments on a pair of pure solid eicosane disks prepared following the ambient temperature solidification was performed. In the first case at T=10 °C, once the tip of the adjustable screw on top of the set up was in touch with the metal plate, thermal conductivity data was measured. Then, each time the screw was turned in such way to impart a pressure on the set up with a step size of 0.25 turns until it reaches 1.25 turns. Similar tests were carried out for the temperatures of 20 and 30 °C. The thermal conductivity data are

shown in Figure 3.12b and are tabulated in Table 3.2. As it is shown in Figure 3.12b, the measured thermal conductivity values are lower than those reported in the literature (Stryker and Sparrow, 1990) for the data associated with 0 and 0.25 turns. The measured data for the case of zero turns show a broad variation that might be associated with thermal expansion coefficients of the samples, cold plates and insulation materials. However, the measured data start to exhibit an asymptotic behavior and are independent of the number of the turns of the screw and the measurement temperature once it reaches to 0.5 turns. The hypothesis is that initially the TPS sensor is not held tightly between the sample pairs and therefore there are some tiny air bubbles in contact with the sensor which results in a lower thermal conductivity value. It should be mentioned that in this chapter, all the data are associated with 0.75 turns of the screw and this condition is kept constant for all the measurements.

3.4 Results and Discussion

For a given CuO particle loading, three (3) tests were performed at each of the aforementioned measurement temperatures and the average values are presented below. For each of the reported data points under any preparation method, the standard deviation was less than 1.35%.

3.4.1 Ambient solidification data

The measured thermal conductivity of solid pure eicosane and eicosane-CuO composites that were prepared following the ambient solidification route are presented in Figure 3.13 and tabulated in Table 3.3. The thermal conductivity data in Figure 3.13 for the 10-34 °C range should be read from the scale on the left ordinate, whereas the data at 35 °C can be recovered from the scale on the right ordinate. The thermal conductivity measurements of pure eicosane matched the experimental data of Stryker and Sparrow (1990) very closely. Similar to Stryker and Sparrow (1990), the measured data were independent of temperature for the 10-33 °C range. However, contrary to the present measured data and those of Stryker and Sparrow (1990), Yarbrough and Kuan (1981) who utilized the steady-state measurement technique (i.e., an unguarded radial heat-flow apparatus) have reported a linear decreasing trend for thermal conductivity of pure eicosane in the solid phase as a function of temperature in the 0-20 °C range. Parallel to Fan (2011), a sudden rise in thermal conductivity is observed for the measurement temperature of 35 °C that is in sharp contrast to the observations of Stryker and Sparrow (1990). With nanoparticle loadings of 1 and 2 wt%, the thermal conductivity was monotonically raised as the concentration of the additives was increased for all the measured temperatures. Surprisingly, for the 10-33 °C range, as the particle loading is raised to 5 wt%, the thermal conductivity of the composite is measured to be lower than 2 wt% samples and equal or a bit higher than the 1 wt% composites. For the measurements performed for the 5 wt% sample as melting is approached (at 35 °C), thermal conductivity is higher than the 1 and 2 wt% composites. Measurements of Fan (2011) for 5 wt% solid samples that were obtained following rapid quenching from an originally liquid sample also exhibited this non-monotonic dependence on the particle loading to the extent that the measured data matched or were even lower than pure

eicosane samples. For the highest loading of the nanoparticles being 10 wt%, the measured thermal conductivity values were the greatest quantities recorded at each measurement temperature. The maximum amount of thermal conductivity enhancement was observed to be nearly 13% (Figure 3.14). Interestingly, the slope of the thermal conductivity rise over the narrow temperature range of 33-35 °C was observed to steepen monotonically as the particle loading was increased.

3.4.2 Ice-water bath solidification data

The measured thermal conductivity of solid pure eicosane and eicosane-CuO composites that were prepared following the ice-water bath solidification route are presented in Figure 3.15 and tabulated in Table 3.4. Thermal conductivity data of composites prepared using the ice-water bath solidification route were found to be lower than the samples obtained by the ambient solidification scheme (Figure 3.13) by nearly 5 percent. Similar to pure eicosane data of Figure 3.13 and those of Stryker and Sparrow (1990), measured thermal conductivity values of pure eicosane were independent of temperature for the 10-33 °C range. The trends of the measured data of composites in Figure 3.13 for the 1, 2, 3.5 and 5 wt% samples carry over almost identically to the ice-water bath solidified disks data of Figure 3.15. For the highest loading of nanoparticles, i.e. 10 wt% eicosane/CuO solid samples prepared using the ice-water bath route, measured thermal conductivity enhancement compared to the 2 wt% sample was observed to be greater when compared to the equivalent samples of Figure 3.13 prepared under the ambient solidification condition. Focusing on the thermal conductivity data at 30 °C, there is a monotonic rise up to 2 wt% loading of nanoparticles. Then, a decreasing trend is observed up to 5 wt%

followed by another monotonic rise up to 10 wt% sample which exhibits the greatest thermal conductivity value. The relative thermal conductivity quantities of the samples obtained by the ice-water bath solidification method along with the predictions of the model of Maxwell (1873) are shown in Figure 3.16. Maxwell's equation is given by Das et al. (2008) as

$$k_{eff} = k_c \left[\frac{k_d + 2k_c - 2\emptyset_{vol}(k_c - k_d)}{k_d + 2k_c + \emptyset_{vol}(k_c - k_d)} \right], \tag{3.7}$$

where subscripts eff, c, d and $\emptyset_{\text{vol}}$ denote effective, continuous phase, discrete phase and the volume fraction of the discrete phase, respectively. Quantity k stands for thermal conductivity (W/mK). In this study, discrete phase is the nano-additive material and the continuous phase is the base PCM (eicosane). Also, the thermal conductivity value of CuO nanoparticles is adopted to be equal to 18 W/mK as it is proposed by Jang and Choi (2007). Note that during the experiments, weight fractions are used for mixing the nanoparticles into the base liquid PCM. Upon solidification of colloids, weight fraction does not change, whereas the base PCM shrinks due to the higher density of eicosane in the solid phase. In effect, the volume fractions of the liquid and solid colloids samples are different. Thus, in utilizing the Maxwell's relation for the solid samples, care must be taken to calculate the correct volume fraction of the solid phase properly. Regardless of the phase, knowing the mass fraction of a nano-additive, it can readily be converted to the corresponding volume fraction using

$$\emptyset_{vol} = \frac{\emptyset_{wt}\rho_c}{\emptyset_{wt}\rho_c + (1 - \emptyset_{wt})\rho_d}, \tag{3.8}$$

where $\emptyset_{wt}$ stands for the mass fraction and ρ stands for relevant densities (kg/m^3). In computing the volume fraction of the solid samples using this equation, the density of the solid phase PCM must be utilized.

While the extent of thermal conductivity enhancement is observed to be always greater than the Maxwell's prediction in Figure 3.16, the plot also exhibits the non-monotonic relation between the thermal conductivity and the mass fraction at a given temperature. As for the slope of the thermal conductivity rise over the narrow temperature range of 33-35 °C, the monotonic dependence on the particle concentration was preserved, however the values of the slopes were greater for samples of Figure 3.15 when compared to similar loadings of Figure 3.13. It appears that the observed deviations of the samples prepared by the ice-water bath solidification route when compared to the ambient solidification scheme can be linked to the rapid phase transformation that might have given rise to (1) greater void percentage within the ice-water bath prepared samples and (2) crystal structure deviations between the two approaches.

3.4.3 Oven solidification data

The measured thermal conductivity of solid pure eicosane and eicosane-CuO composites that were prepared following the oven solidification route are presented in Figure 3.17 and tabulated in Table 3.5. Thermal conductivity data of the samples prepared under the oven solidification method were found to be the highest values compared with the samples prepared using either the ambient solidification scheme (Figure 3.13) or the ice-water bath solidification method (Figure 3.15). For example, considering the data for 10 wt% mass fraction samples, variations of thermal conductivity values vs. temperature for all three preparation schemes are shown in Figure 3.18. The results suggest that at a constant concentration of particles if the solidification process takes place over a longer time period, the thermal conductivity values increase. The hypothesis is that longer phase change duration leads to formation of bigger micro-

grains in the structure of solid NePCM composites. Consequently, the number of thermal resistance layers decreases and the overall thermal conductivity values increase.

3.5 Attempts to Address Different Thermal Conductivity Results in Terms of Crystal Structure of the Solid Sample

A number of experimental methods were applied in order to address the probable dependence of the solidification route on the observed values of thermal conductivity. However, the attempts were finally unsuccessful. Attempts to utilize scanning electron microscopy (SEM) failed in the middle of testing procedure due to the low melting temperature of eicosane, i.e. 37 °C, while the output electron beam of the SEM instrument requires a material with a melting temperature of at least 60 °C (Miller, 2012 and Prorok, 2012). Then, the atomic force microscopy (AFM) was performed and it failed too due to the high sensitivity of the method to semi-rough surface of our solid eicosane samples (Auad, 2012). Finally, the X-ray diffraction (XRD) method was utilized for pure eicosane sample solidified under the oven solidification route and the average size of crystallite structure was determined to be 33 nm. However, due to lack of literature data on the crystallite size study of hydrocarbon-based materials, the applied method could not be properly verified (Fergus, 2012).

3.6 Preliminary Work on Multi-Walled Carbon Nanotubes (MWCNTs)

MWCNTs (purity>95%, outer diameter of 6-9 nm, length of 5 μm, density of 2100 kg/m^3, Sigma Aldrich, St. Louis, MO) were introduced into eicosane as the base PCM. The objective was to compare the thermal conductivity enhancement potential of this alternative nano-additive versus that of CuO nanoparticles. CNTs' rod-shape structures differ markedly from spherical CuO nanoparticles that were studied earlier in the project. Therefore, their concentration within the base material should be such that a network of CNT rods in contact to each other is created in order to assure increasing the thermal conductivity of the matrix. The minimum concentration of CNTs that will give rise to formation of long-range connectivity of the matrix is referred to as percolation threshold. The percolation threshold for the MWCNTs was calculated based on the relation given by Larson (1998). It is defined as the lowest concentration of particles which ensures that MWCNT rods are well inter-connected within the NePCM solid composite. The equation is given as:

$$\phi_{percolation} = \frac{Volume\ of\ 1\ Rod}{Excluded\ Volume\ of\ 1\ Rod} = \frac{\pi R^2\left(\frac{4}{3}R+L\right)}{\frac{32}{3}\pi R^3+8\pi R^2 L+4RL^2\langle\sin\gamma\rangle} \approx \frac{R}{L}, \tag{3.9}$$

where R and L refer to the radius and length of the MWCNT rods, respectively.

For our specific carbon nanotubes dimensions, the percolation threshold was calculated to be equal to 0.1 vol% (0.27 wt%). After preparing 20 ml of the 0.1 vol% eicosane-MWCNTs liquid sample under the same procedure as eicosane-CuO colloids, as per assistance of Davis and

Benavides (2012), the eicosane-MWCNTs liquid colloid was poured into a shear mixing chamber which was already placed into a hot oil bath maintained at 80 °C (Figure 3.19). The colloid was then allowed to be continuously mixed for 72 hours. Upon removing the samples from the mixing set up, the colloids were subjected to one of two solidification procedures that follow. One pair of NePCM solid disks was obtained under solidification at the ambient temperature. The second pair was prepared by placing the bottom of the aluminum molds containing the liquid samples directly in contact with an ice-water bath. The measured thermal conductivity of solid pure eicosane and eicosane-MWCNTs composites are presented in Figure 3.20 and also tabulated in Table 3.6. Three runs were performed at each of the measurement temperatures and the average values are presented. The standard deviation of the measured data was nearly 1%. Similar to the results for the eicosane-CuO samples, measured thermal conductivity data of the eicosane-MWCNTs composites were found to be nearly independent of the measurement temperature in the temperature range of 10-33 °C. Irrespective of the solidification method, as the melting temperature was approached, thermal conductivity data of the solid disks rose sharply. The composites prepared using the ice-water bath solidification scheme consistently exhibited lower values of thermal conductivity compared to the disks solidified at ambient temperature. This observation is consistent with the findings for the eicosane-CuO nanoparticle colloids prepared following similar routes. Around 25% and 35% improvement in thermal conductivity values were observed for the composites prepared under ice-water bath solidification and ambient temperature solidification methods, respectively. This range of thermal conductivity enhancement is much greater than that of 1 wt% eicosane-CuO samples (~1-4%) fabricated under any of the three aforementioned solidification routes. However, proper functionalization procedures need to be undertaken for MWCNTs in the future

studies to ensure its stability over long-time thawing/freezing cycles in actual thermal energy systems applications.

3.7 Summary

Thermal conductivity of pure eicosane, eicosane-CuO and eicosane-MWCNTs solid composites with different loadings of CuO nanoparticles and a constant concentration of MWCNTs were measured experimentally by using the transient plane source technique. The samples were prepared using three different solidification routes. With the aid of a controllable temperature bath, measurements were conducted at various temperatures between 10 and 35 °C for the solid samples. The pertinent conclusions are:

1. Measured thermal conductivity values of the composites were found to be independent of the measurement temperature for a given particle loading regardless of the solidification procedure.

2. Irrespective of the preparation/solidification scheme, as the melting temperature was approached, thermal conductivity of the composites rose sharply for all sets of solid disks.

3. The ice-water bath solidification route for the eicosane-CuO samples consistently exhibited lowest values of thermal conductivity, whereas the samples of oven solidification scheme corresponded to the highest values. This behavior might be due to the greater void population of ice-water bath samples and/or crystal structure deviations due to processing routes.

4. Considering eicosane-CuO composites, for mass fractions greater than 2 wt%, a non-monotonic relation between the thermal conductivity and the mass fraction, independent of the temperature range studied, was exhibited.

5. Although no functionalization was performed on the MWCNTs, the amount of thermal conductivity enhancement for 0.27 wt% eicosane-MWCNTs solid samples (~25-35%) was much higher than that of 1 wt% eicosane-CuO solid disks (~1-4%).

Table 3.1 Specifications and the range of applicability of the TPS 500 instrument (Hot Disk AB, Gothenburg, SWEDEN)

Materials	Solids, Medium to high viscosity liquids Small particles/powders
Thermal Conductivity (W/mK)	0.03 ~ 100
Thermal Diffusivity (mm^2/sec)	0.02 ~ 40
Specific Heat (MJ/m^3K)	0.1 ~ 4.5
Measurement Time (sec)	2.5 ~ 640

Table 3.2 Thermal conductivity data of solid pure eicosane disks prepared following the ambient temperature solidification route versus the number of turns of the adjustable screw on top of the support set up; Reported values are average of three measurements (maximum standard deviation of 1.5%)

Number of Turns of the Screw	**T=10 °C**	**T=20 °C**	**T=30 °C**
0	0.3641	0.3732	0.3605
0.25	0.4134	0.4112	0.4128
0.5	0.4215	0.4228	0.4237
0.75	0.4216	0.4224	0.4234
1	0.4217	0.4228	0.4235
1.25	0.4216	0.4229	0.4226

Table 3.3 Thermal conductivity data of solid pure eicosane and eicosane-CuO composites prepared following the ambient solidification route; Reported values are average of three measurements (maximum standard deviation of 1.35%)

Temperature (°C)	Pure	1 wt%	2 wt%	3.5 wt%	5 wt%	6.5 wt%	8 wt%	10 wt%
10	0.4212	0.4333	0.4552	0.4490	0.4394	0.4360	0.4675	0.4761
15	0.4230	0.4286	0.4506	0.4443	0.4340	0.4322	0.4661	0.4677
20	0.4223	0.4314	0.4564	0.4458	0.4355	0.4312	0.4677	0.4713
25	0.4241	0.4300	0.4503	0.4424	0.4357	0.4350	0.4532	0.4598
30	0.4244	0.4313	0.4532	0.4441	0.4320	0.4323	0.4551	0.4631
32	0.4267	0.4331	0.4596	0.4511	0.4365	0.4320	0.4622	0.4711
33	0.4229	0.4348	0.4625	0.4538	0.4386	0.4359	0.4730	0.4756
34	0.4513	0.4667	0.4806	0.4783	0.4743	0.4696	0.4861	0.5032
35	0.5503	0.5698	0.5907	0.6170	0.6139	0.6083	0.6320	0.7003

Table 3.4 Thermal conductivity data of solid pure eicosane and eicosane-CuO composites prepared following the ice-water bath solidification route; Reported values are average of three measurements (maximum standard deviation of 1.15%)

Temperature (°C)	Pure	1 wt%	2 wt%	3.5 wt%	5 wt%	6.5 wt%	8 wt%	10 wt%
10	0.4011	0.4123	0.4371	0.4230	0.4178	0.4199	0.4437	0.4606
15	0.4025	0.4110	0.4369	0.4256	0.4192	0.4203	0.4496	0.4550
20	0.4013	0.4076	0.4308	0.4310	0.4137	0.4212	0.4434	0.4532
25	0.4009	0.4151	0.4347	0.4306	0.4184	0.4231	0.4432	0.4562
30	0.3998	0.4097	0.4418	0.4365	0.4163	0.4226	0.4428	0.4508
32	0.4032	0.4169	0.4424	0.4347	0.422	0.4244	0.444	0.4576
33	0.4027	0.4238	0.4431	0.4345	0.4231	0.4229	0.4454	0.4594
34	0.4203	0.4457	0.4678	0.4588	0.4517	0.4565	0.4671	0.4773
35	0.5827	0.6196	0.6486	0.6577	0.6702	0.6695	0.6796	0.6989

Table 3.5 Thermal conductivity data of solid pure eicosane and eicosane-CuO composites prepared following the oven solidification route; Reported values are average of three measurements (maximum standard deviation of 1.4%)

Temperature (°C)	Pure	1 wt%	2 wt%	3.5 wt%	5 wt%	6.5 wt%	8 wt%	10 wt%
10	0.4505	0.4612	0.4839	0.4718	0.4537	0.4525	0.4953	0.5114
15	0.4528	0.4634	0.4822	0.4736	0.4592	0.4566	0.4961	0.5102
20	0.4597	0.4626	0.4835	0.4730	0.4586	0.4588	0.4921	0.5118
25	0.4513	0.4653	0.4831	0.4722	0.4603	0.4574	0.4950	0.5060
30	0.4530	0.4609	0.4878	0.4731	0.4541	0.4518	0.4975	0.5123
32	0.4519	0.4667	0.4893	0.4769	0.4577	0.4571	0.4932	0.5057
33	0.4551	0.4733	0.5001	0.4911	0.4700	0.4630	0.5054	0.5222
34	0.4789	0.4894	0.5164	0.4953	0.4814	0.4791	0.5311	0.5416
35	0.6317	0.6541	0.6896	0.6802	0.6638	0.6589	0.7006	0.7312

Table 3.6 Thermal conductivity data of solid pure eicosane and 0.1 vol% eicosane-MWCNTs composites prepared following the ambient solidification/the ice-water bath solidification route; Reported values are average of three measurements (maximum standard deviation of 1%)

Temperature (°C)	Pure	Ice-Water Bath Solidification	Ambient Temp. Solidification
10	0.4003	0.5156	0.5440
15	0.4076	0.4915	0.5117
20	0.4010	0.5023	0.5476
25	0.3931	0.4992	0.5596
30	0.4008	0.5088	0.5332
33	0.4057	0.5401	0.5869
35	0.5712	1.0690	1.1240

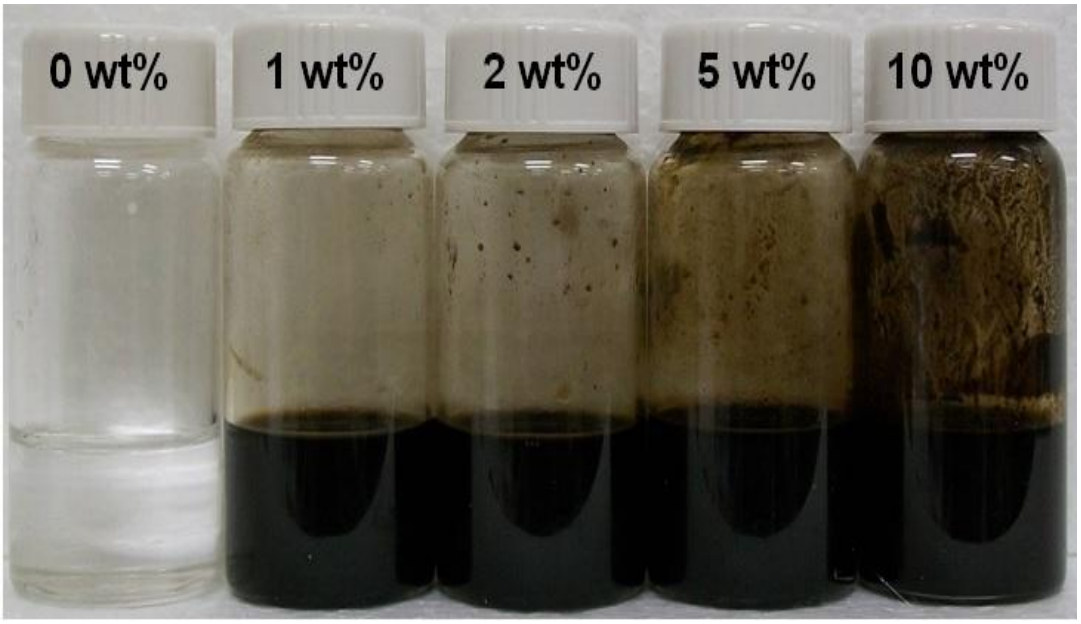

Figure 3.1 Photograph of eicosane-based NePCM samples (in liquid phase) with different mass fractions of CuO nanoparticles (Fan, 2011)

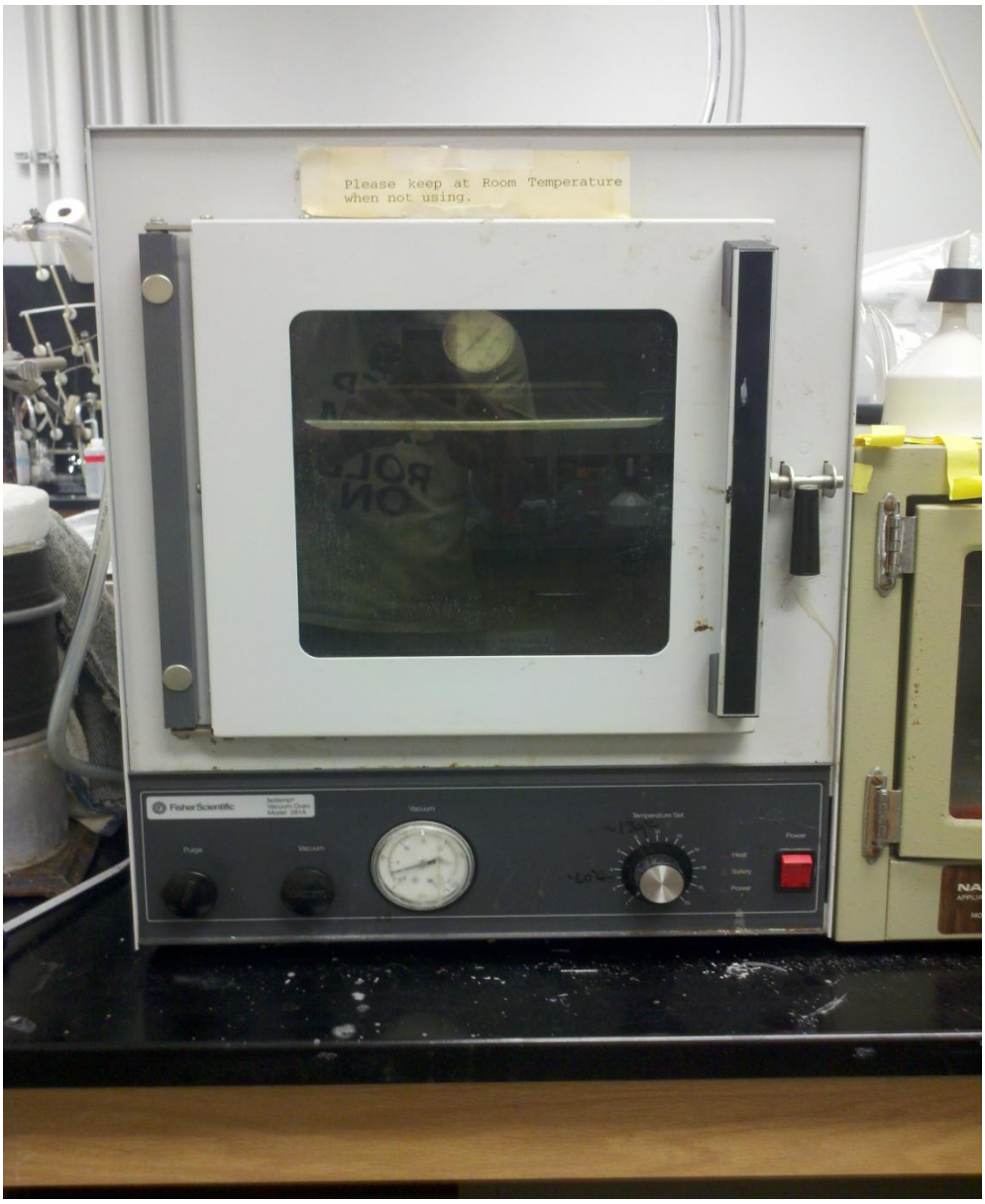

Figure 3.2 Photograph of vacuum oven (Fischer Scientific, Isotemp® Vacuum Oven Model 281A)

Figure 3.3 Photograph of pre-fabricated 1 inch in diameter aluminum foil molds (VWR® International LLC., Model 611-1362)

Figure 3.4 Photograph of the custom-designed molding handle

Figure 3.5 Photograph of eicosane-based NePCM composite samples obtained through freezing of liquid colloids by an ice-water bath right after removal from the mold

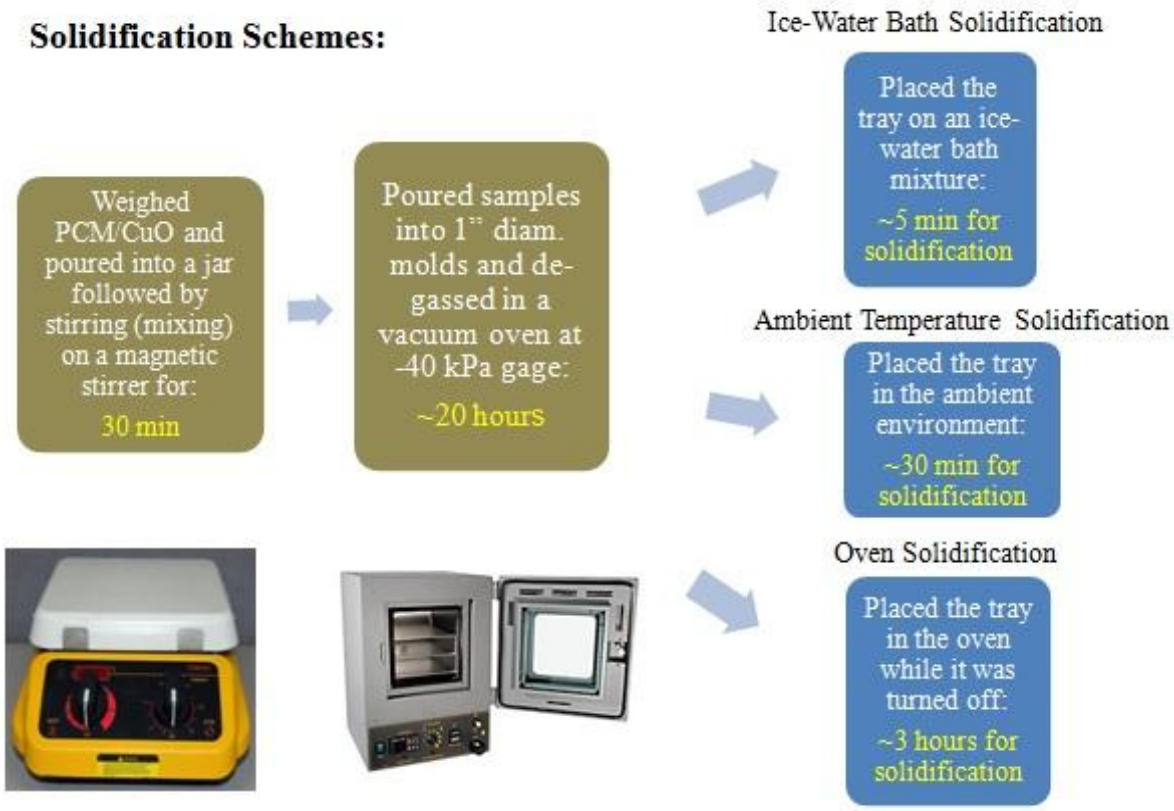

Figure 3.6 Overview diagram of the colloids preparation and solidification schemes

Figure 3.7 Photograph of the Hot Disk thermal constants analyzer (TPS 500, Hot Disk AB, Gothenburg, SWEDEN)

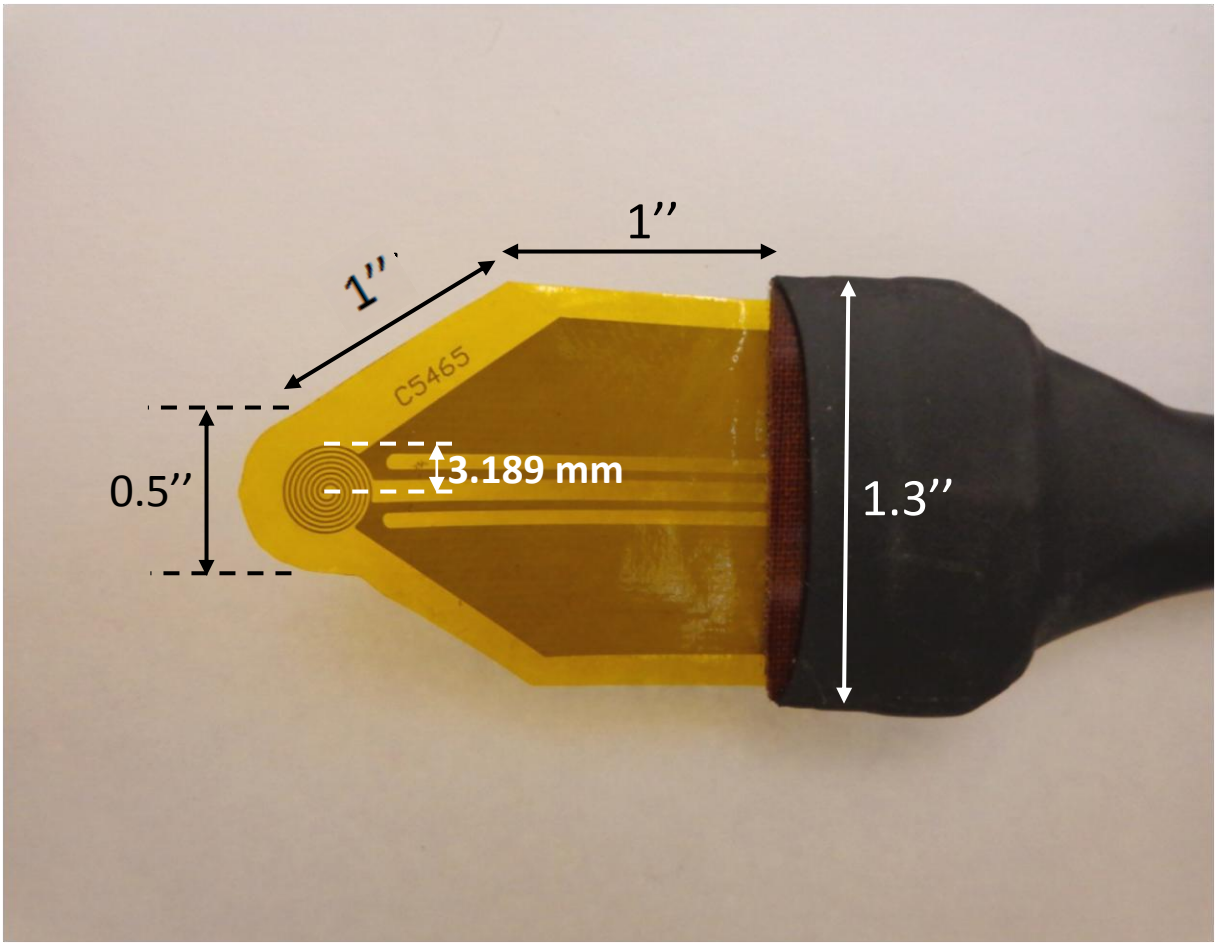

Figure 3.8 Photograph of the Kapton-insulated TPS sensor for thermal conductivity measurements

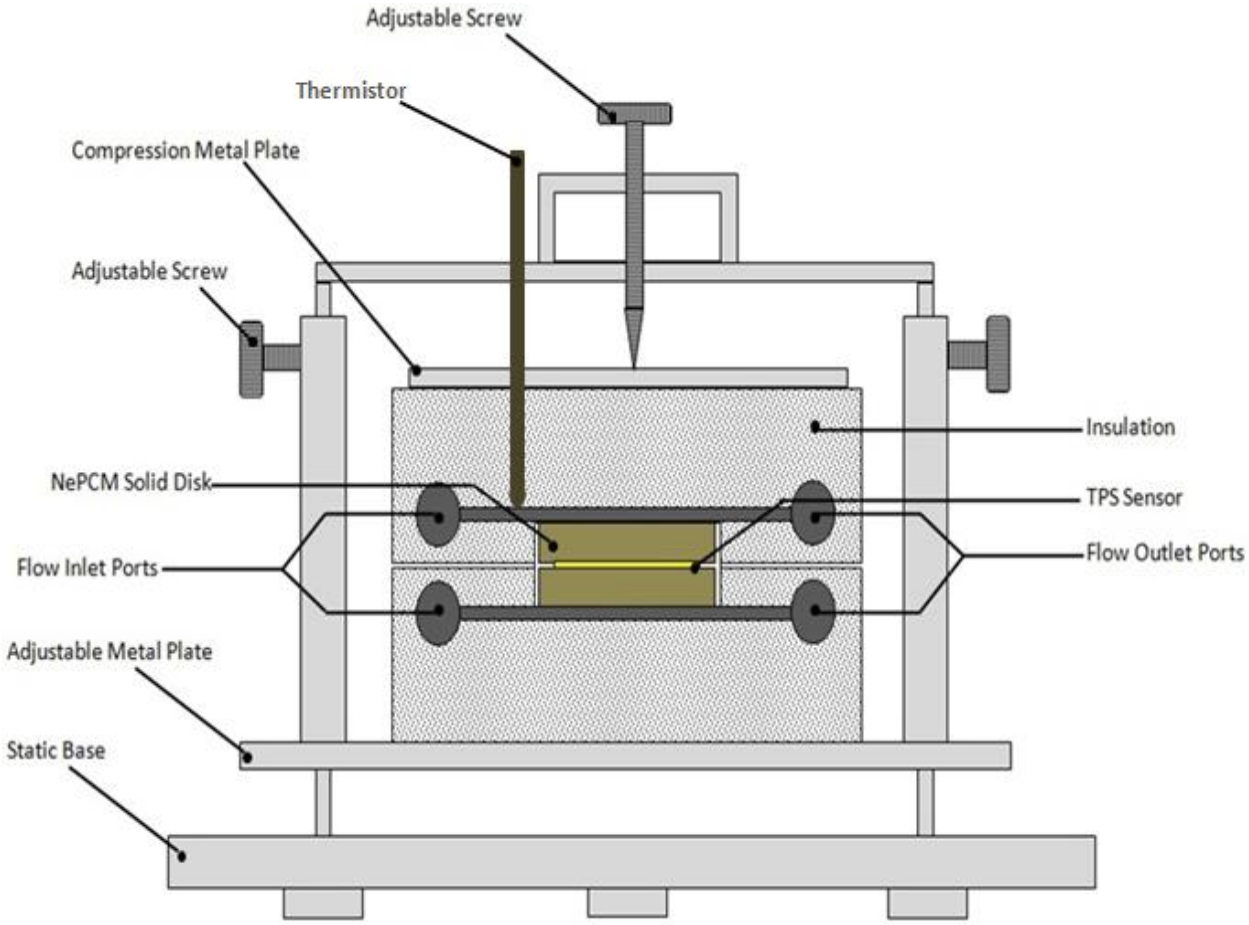

Figure 3.9 Schematic of the support set-up for the samples supplied with the TPS 500 instrument (Hot Disk AB, Gothenburg, SWEDEN)

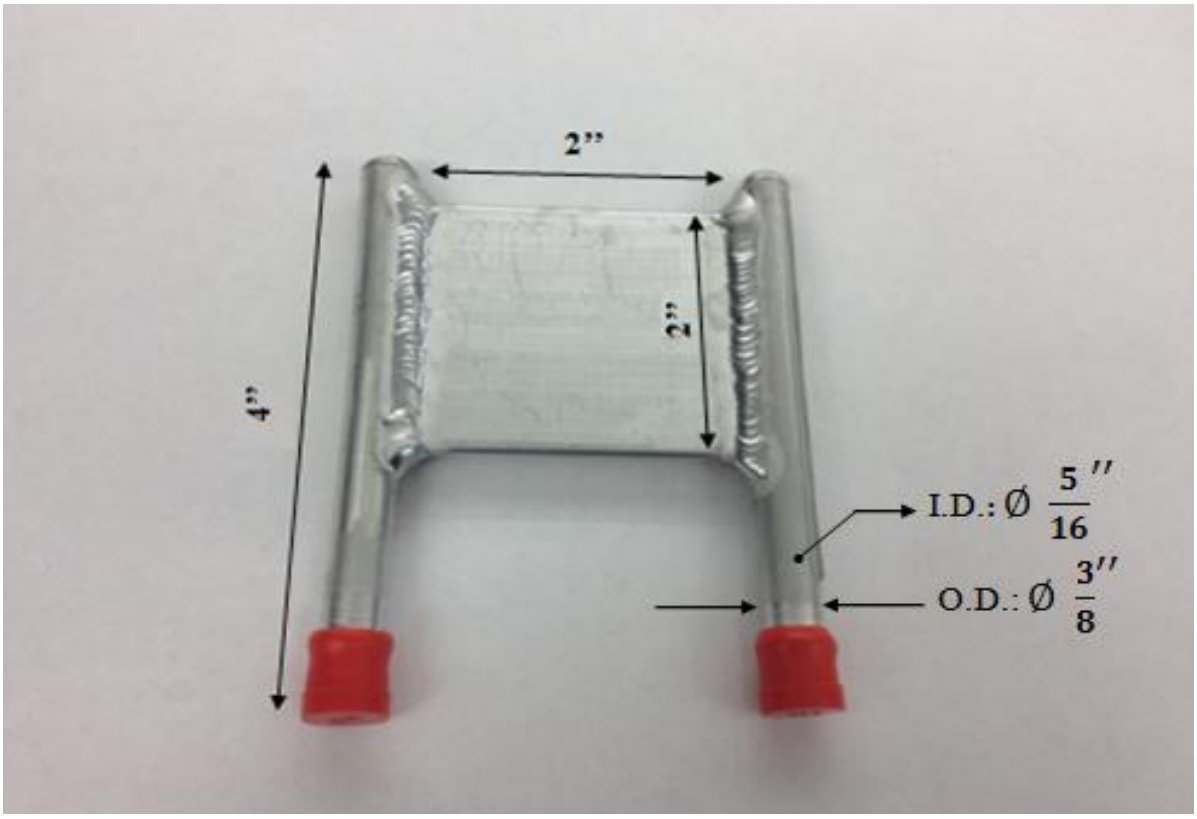

Figure 3.10 Photograph of the aluminum cold plate (LYTRON Co., Woburn, MA, Model CP20G01)

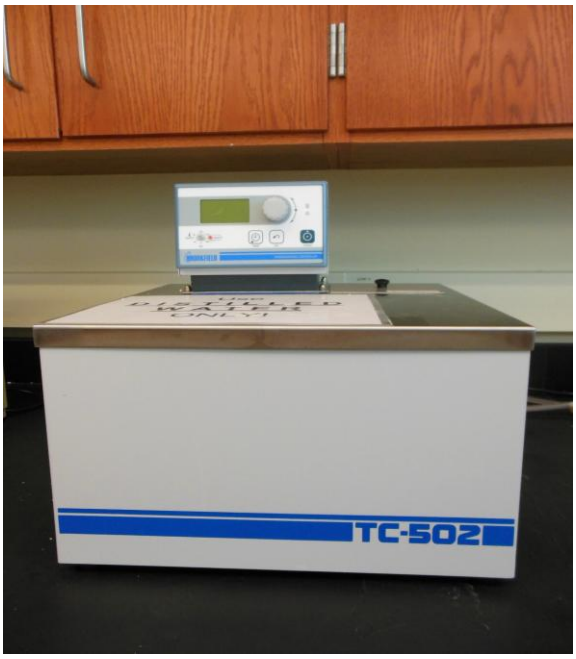

(a)

(b)

Figure 3.11 Photographs of (a) the programmable temperature bath (TC-502P, Brookfield, Middleboro, MA) and (b) the thermistor (GE, Model A733F-CSP60BT103M, accuracy of 0.01 °C) for temperature reading of the cold plate

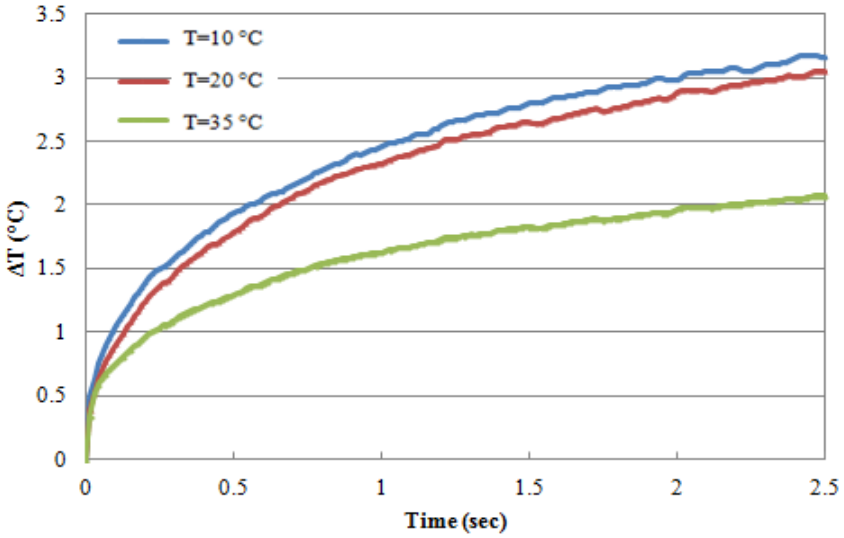

(a)

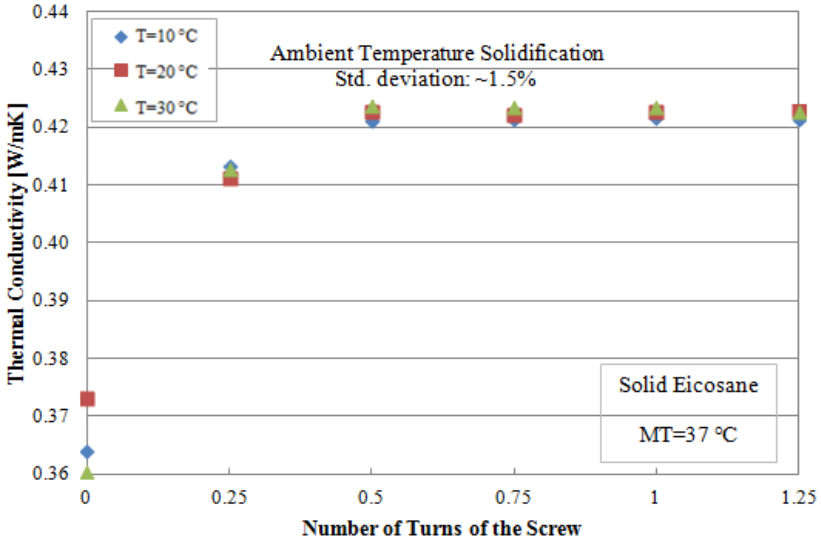

(b)

Figure 3.12 (a) Typical temperature rise vs. time data that were obtained by the TPS sensor for the case of purse eicosane samples, and (b) Thermal conductivity of solid pure eicosane disks prepared following the ambient temperature solidification route versus the number of turns of the adjustable screw on top of the support set up

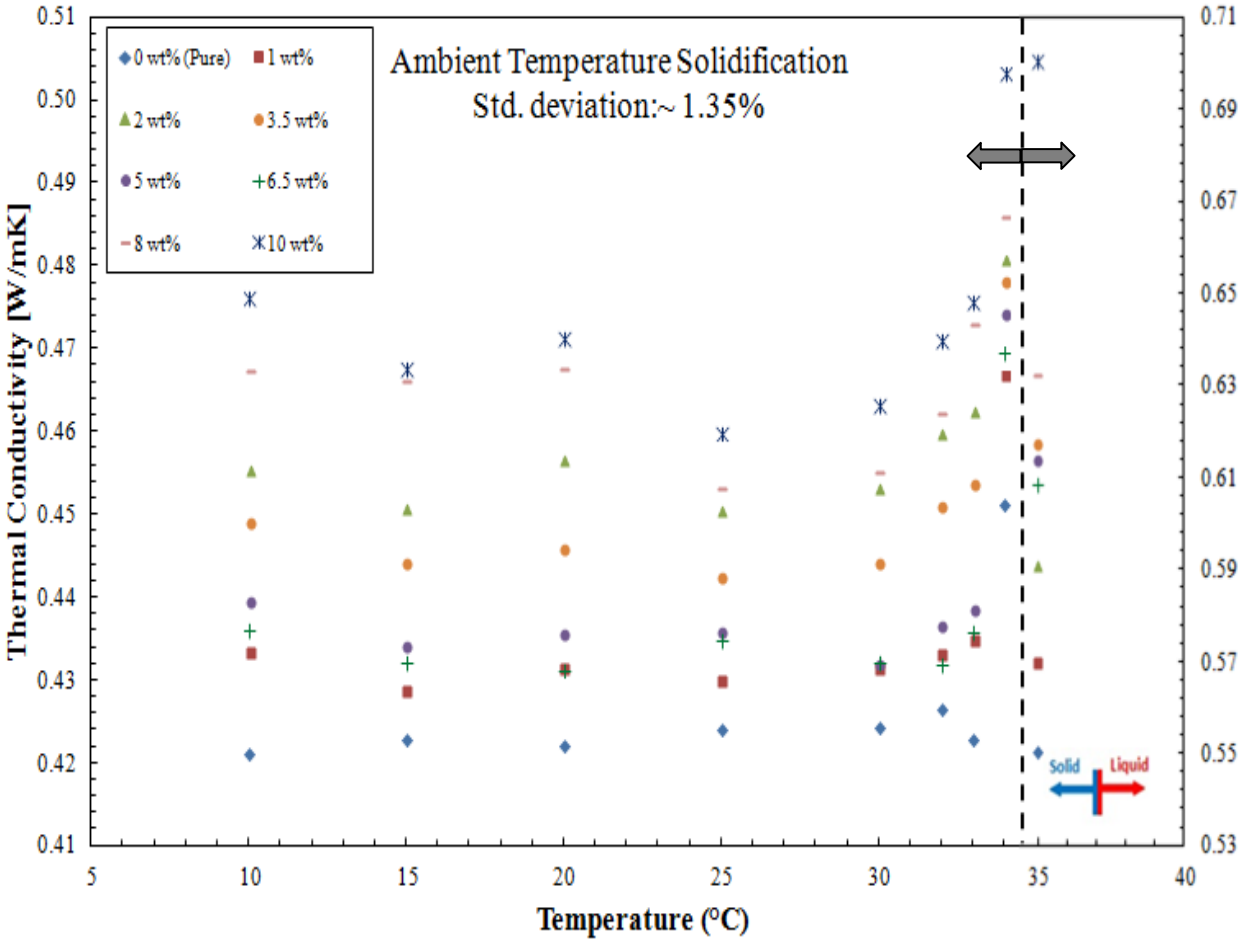

Figure 3.13 Thermal conductivity of solid pure eicosane and eicosane-CuO composites prepared following the ambient temperature solidification route

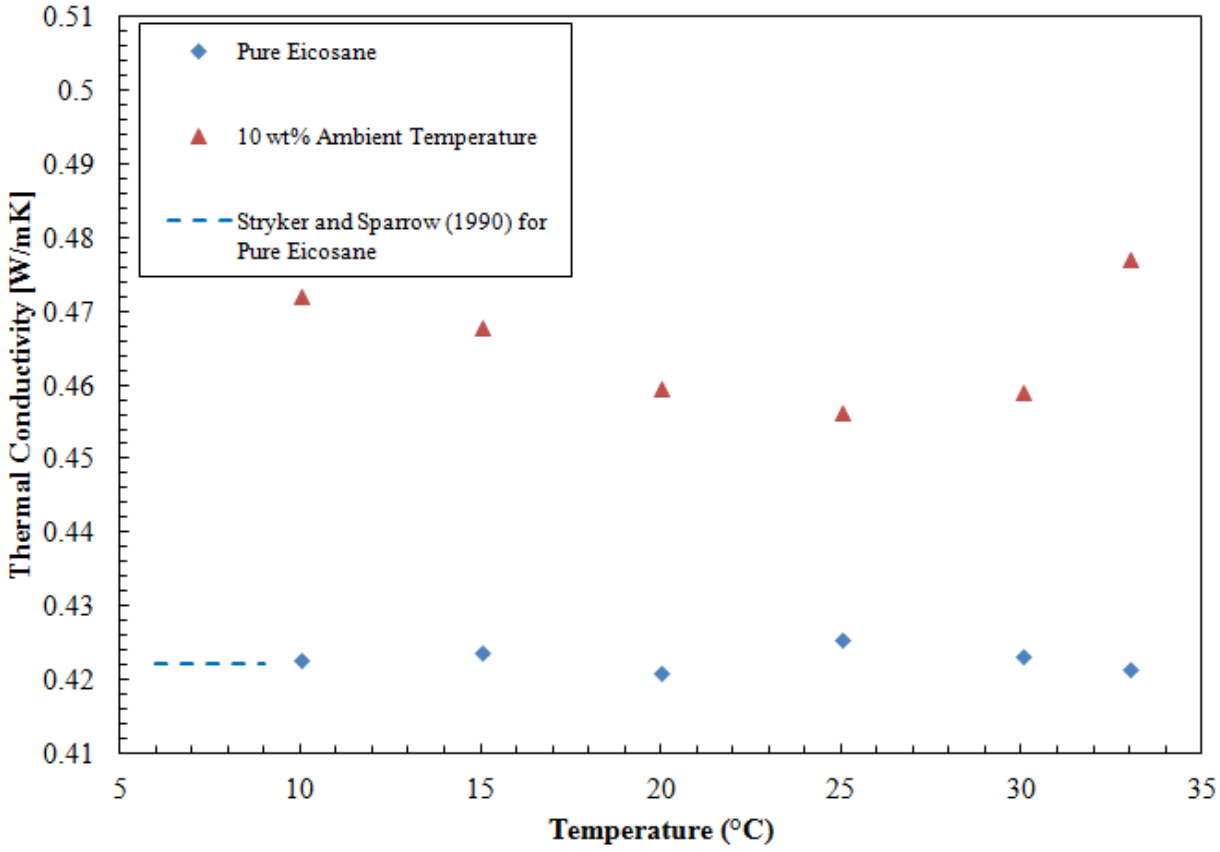

Figure 3.14 Thermal conductivity data for 10 wt% sample vs. pure eicosane following the ambient temperature solidification route

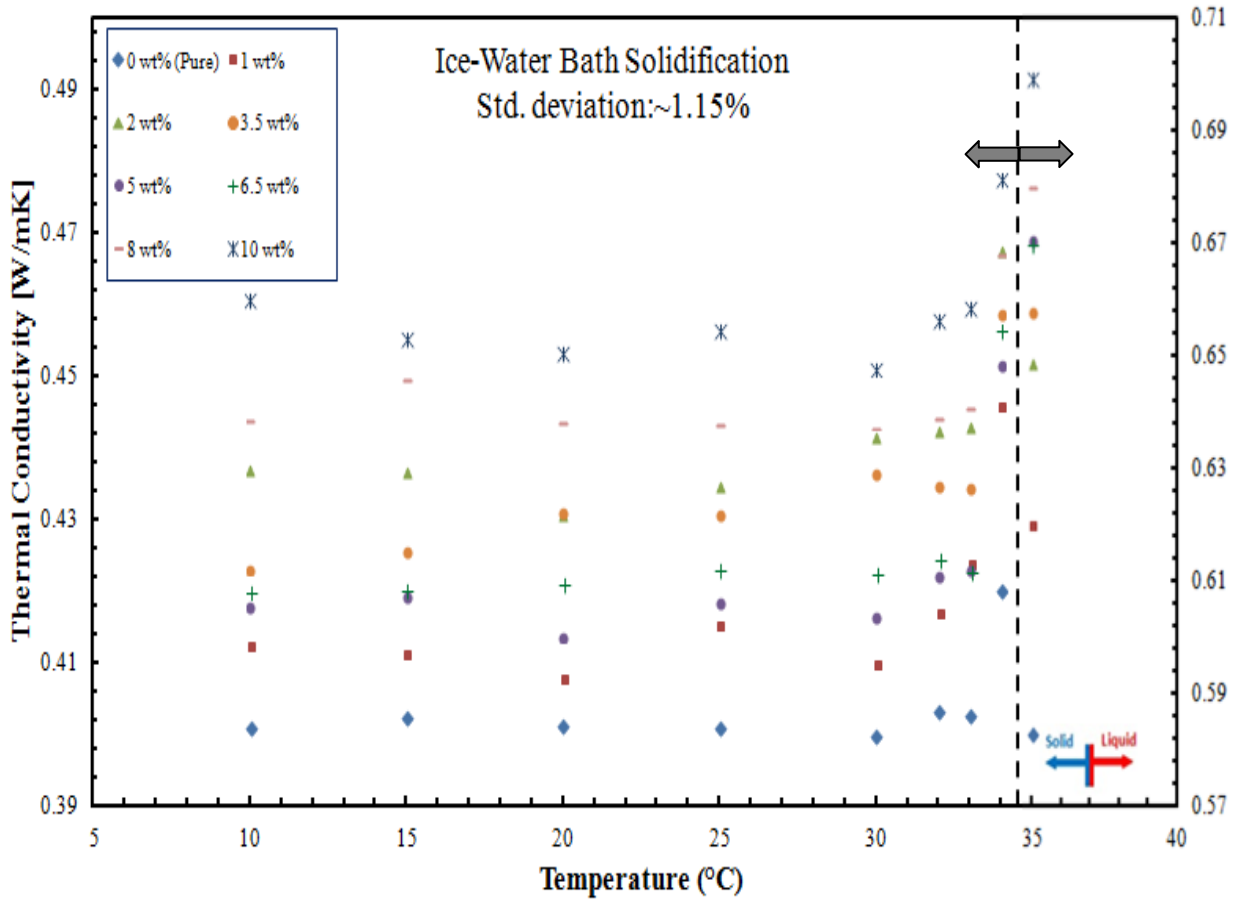

Figure 3.15 Thermal conductivity of solid pure eicosane and eicosane-CuO composites prepared following the ice-water bath solidification route

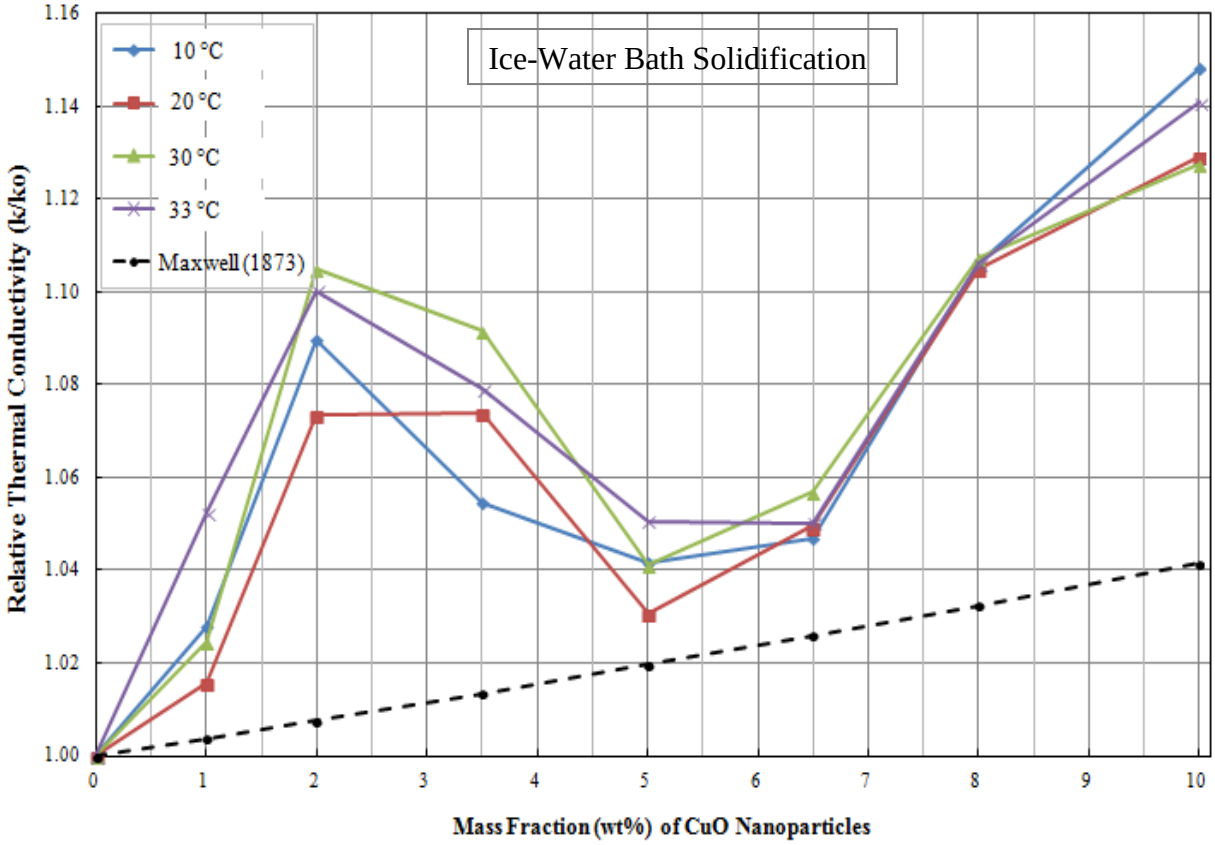

Figure 3.16 Relative thermal conductivity of the samples obtained by the ice-water bath solidification method along with the predictions of the Maxwell's equation

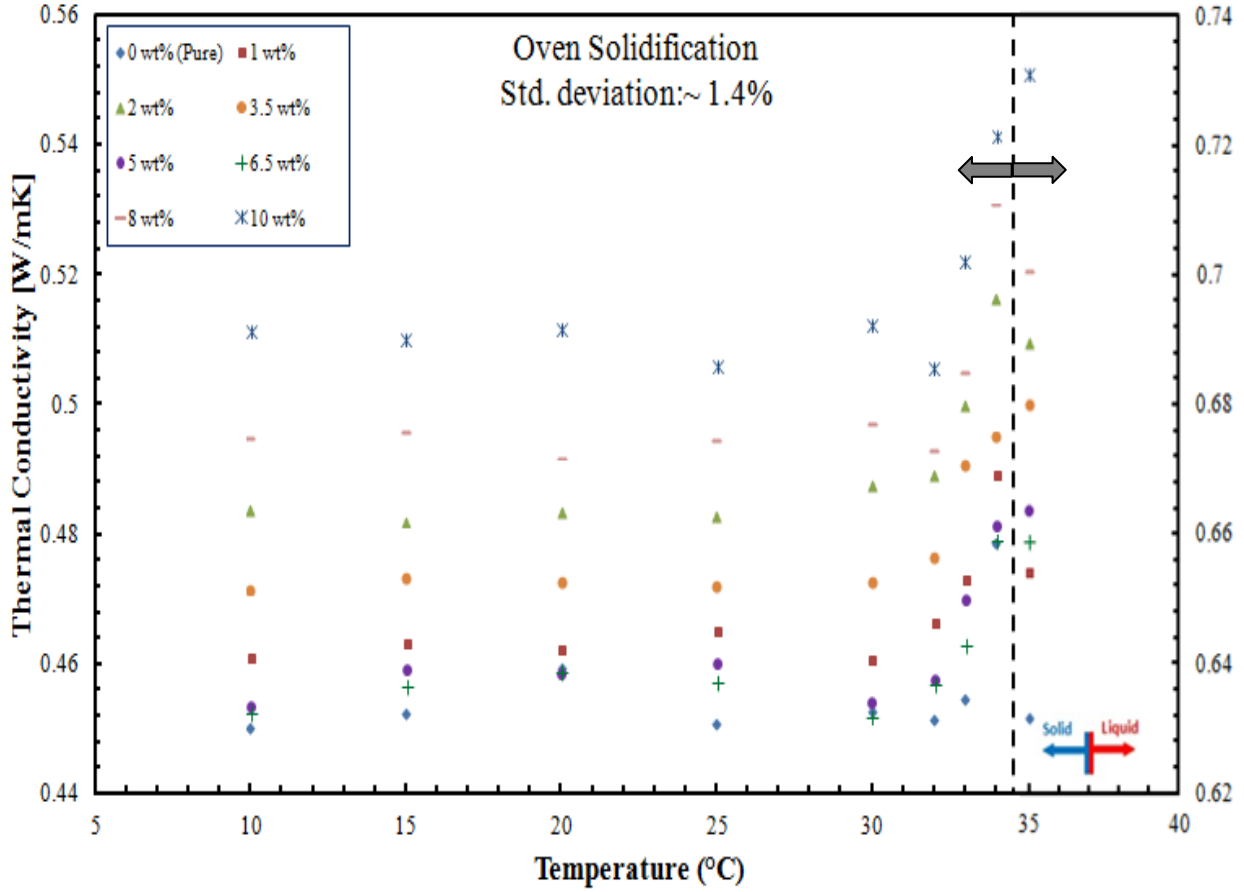

Figure 3.17 Thermal conductivity of solid pure eicosane and eicosane-CuO composites prepared following the oven solidification route

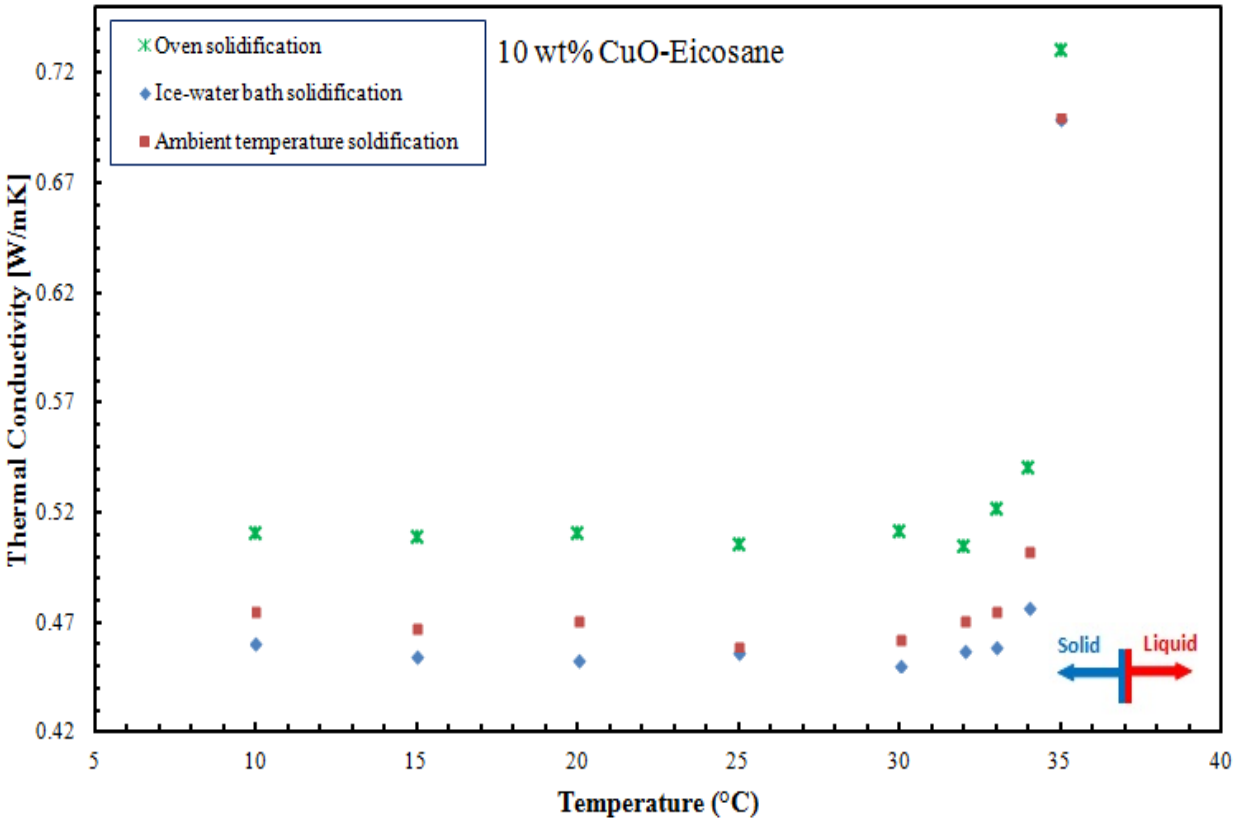

Figure 3.18 Measured thermal conductivity values for the most concentrated eicosane-CuO samples (10 wt%) corresponding to the three different methods of solidification

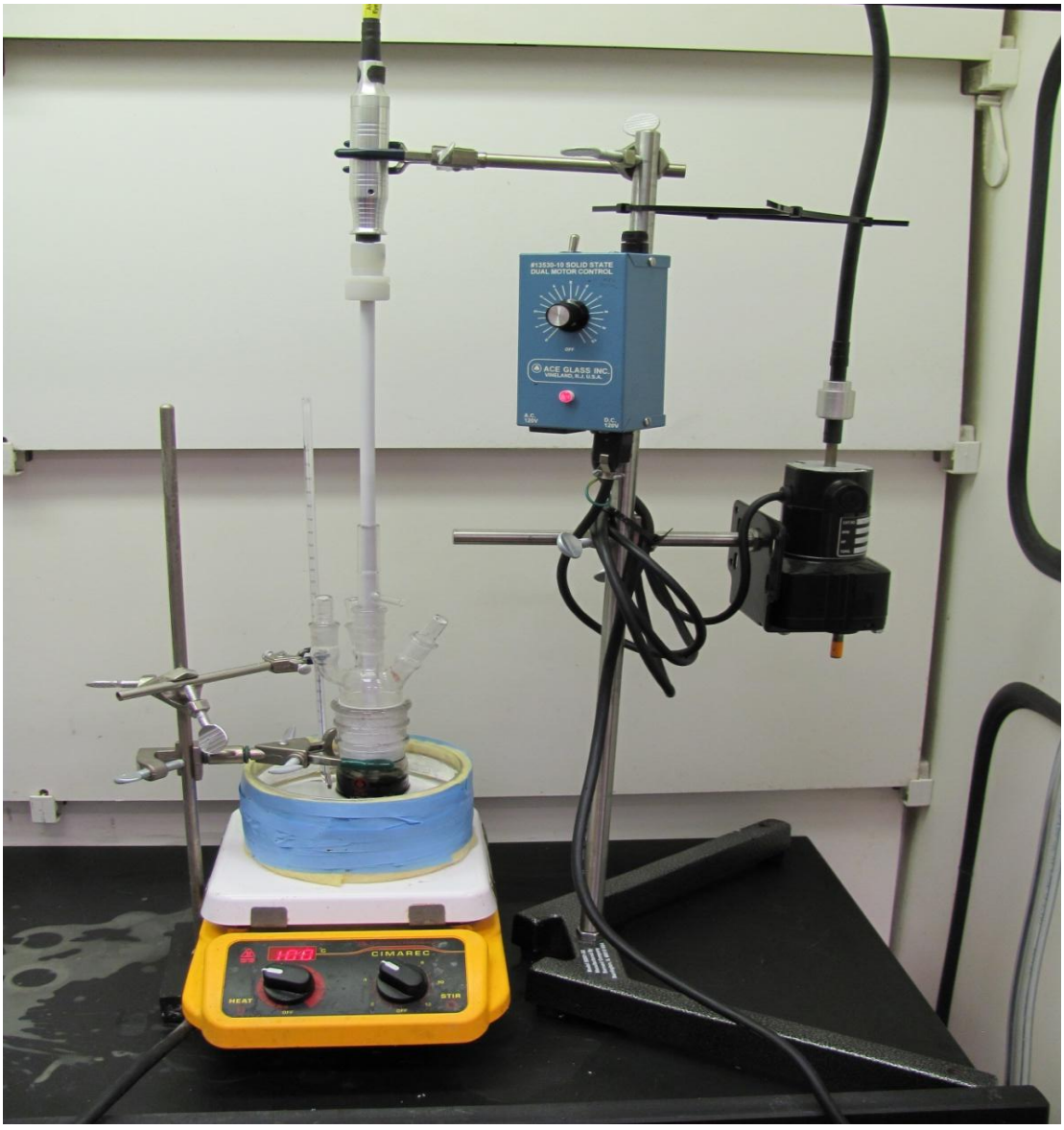

Figure 3.19 Photograph of shear mixing setup utilized for preparation of the 0.1 vol% eicosane-MWCNTs colloid processed within a hot oil bath held at 80 °C (courtesy of Chad Rose, undergraduate student at Auburn University, 2012)

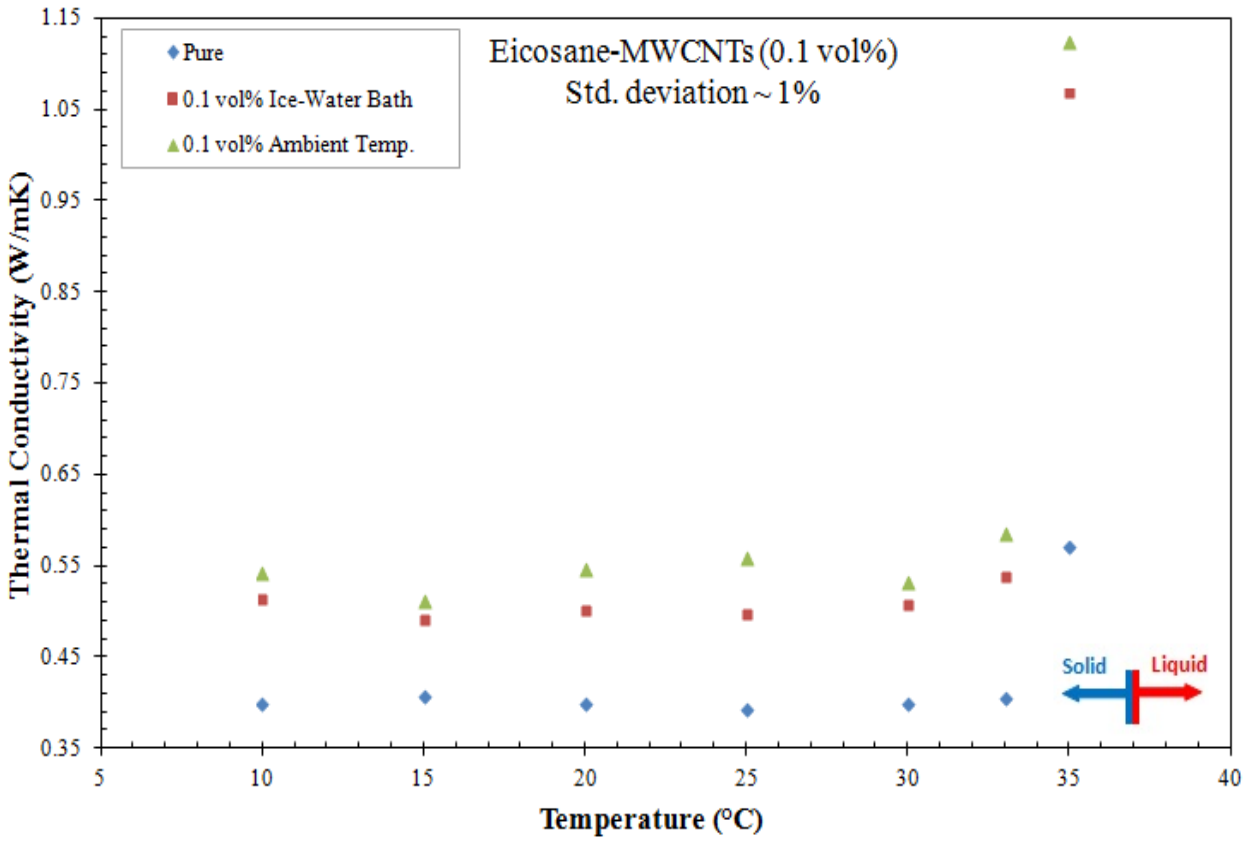

Figure 3.20 Thermal conductivity data of solid pure eicosane and 0.1 vol% eicosane-MWCNTs composites prepared following the ambient solidification/ice-water bath solidification routes

Chapter 4 Explaining Anomalous Thermal Conductivity Measurements near the Melting Temperature

The performance of the commonly-used transient hot wire (THW) technique for measuring the thermal conductivity of materials near their liquid-solid transition point is reported in this chapter. At the beginning of the chapter, a brief introduction to the theoretical studies directed at developing and refining the transient hot wire method is presented in a chronological order. Then, following the problem statement and its mathematical formulation, the adopted computational methodology is discussed in detail. Finally, results and discussions are reported.

4.1 Introduction

Experimental techniques are widely used for determination of various transport properties, such as thermal conductivity, viscosity, etc. These techniques are deeply-rooted in the fundamental relations that govern how the value of the pertinent flux (heat, momentum, etc.) relates to the gradient of the relevant quantity (temperature, velocity, etc.). For instance, both the steady-state and transient techniques that are used for determination of the thermal conductivity utilize the Fourier's Law.

The transient hot wire technique that is now widely used for determination of the thermal conductivity of gases, liquids, pastes, etc., has its roots in an ideal limiting case of a transient heat conduction problem (Carslaw and Jaeger, 1959). In this formulation, an extremely thin wire of infinite length with a high thermal conductivity is surrounded by a homogeneous material that extends in the radial direction away from the wire to infinity. Upon heating the wire for a short time period, the transient signature of the wire's temperature is utilized to obtain the thermal conductivity. The pertinent relation will be discussed below. Assael et al. (2010) has extensively discussed the historical evolution of the transient hot wire technique starting from 1780 up to 2010.

Corrections to the transient hot wire technique that address deviations from the idealized formulation have also been developed. Nine (9) such modifications that account for effects of finite inner cylinder, composite cylinders, Knudsen effects, radiation, required condition at the outer cell circumference, the role of compressibility and natural convection, finite cell dimensions, variable fluid properties and the correction for finite length of wire were addressed in detail by Healy et al. (1976). Thereafter, Nagasaka and Nagashima (1981) developed a new design of an instrument based on the transient hot wire technique by coating the platinum wire with a thin electrical insulation layer made of polyester 2. In this way, the applicable domain of the instrument was broadened to include electrically-conducting fluids. Until that time, the bare metallic wire within the instrument was only compatible with electrically non-conducting media. The analytical solution considering the effects of the insulation layer on the temperature rise of the metallic wire was then discussed extensively. As a case study, thermal conductivity values of an aqueous NaCl solution was measured successfully with an accuracy of $\pm 0.5\%$.

More recently, operational deviations from the ideal case are treated computationally to include the above-mentioned or other effects, whereby analytical relations are replaced with numerical solutions of the governing differential equations, e.g. Assael et al. (1998), Duluc et al. (2003) and Rusconi et al. (2007). Assael et al. (1998) used a numerical finite-element method (FEM) to solve a set of energy conservation equations which describe the operation of the transient hot wire technique. They showed that the method is applicable to predict the thermal conductivity values of liquids. The adopted program considers the essential corrections to the ideal transient hot wire theoretical model which leads to accurate predictions when compared with the experimentally-measured thermal conductivity values. The authors reported computationally-obtained thermal conductivity values vs. literature values for Argon at high pressure conditions with an accuracy of $\pm 0.35\%$. Utilizing the velocity–pressure formulation, spectral methods and domain decomposition technique, Duluc et al. (2003) studied 2-D transient natural convection in liquid nitrogen around a pulse-heating thin bronze wire. The numerical data were then compared with their experimental observations. Considering time evolution diagram of wire superheat, the theoretical heat conduction solution and numerical results were in close agreement during early time steps which indicates a purely conductive heat transfer regime. However, there was an onset time at which natural convection effects became important and thereafter results of the numerical simulation start to diverge from experimental data. The authors proposed the wire thermal inertia as the key role-player of the aforementioned behavior which must be taken into account. Rusconi et al. (2007) studied the same phenomenon using the FlexPDE finite element method analysis on a 2-D cylindrical model. The Navier-Stokes equations along with the heat transport equation were solved simultaneously in the fluid region. A custom-built setup based on the transient hot wire method was also fabricated and tested

against results of the numerical simulation. The occurrence of natural convection effects after a specific time period was observed. To successfully exclude convective effects from thermal conductivity measurements, an operational time scale was quantified. The suggested time-window depends on the dissipated power from the wire and the physical properties of the test fluid. It was also proved that the thickness and the physical properties of the wire insulation layer are such that it will not affect the obtained thermal conductivity values. Adoption of computational techniques to assess variations of the transient hot wire method has also been considered for other measurement techniques. For instance, Rusconi et al. (2004) utilized computational fluid dynamics for refinement of thermal-convection effects in the thermal-lensing measurement technique.

No study could be found to describe the behavior and applicability of the transient methods of measuring thermal conductivity near the melting temperature of the medium. Therefore, computational modeling of the transient hot wire method and assessing its performance while melting occurs during the thermal conductivity measurement is attempted in this Chapter.

4.2 Problem Statement

Measuring thermal conductivity of solid phase change materials (PCM) versus temperature using the transient methods, i.e. transient plane source (TPS) and transient hot wire methods, many researchers have reported a sharp rise in thermal conductivity values as the measurement temperature approaches the melting point of the PCM. Recently, using the transient

hot wire method, Wang et al. (2008, 2009, 2010a, and 2010b) reported sharp rises in their experimentally-obtained thermal conductivity values for different phase change materials near their respective melting temperatures (Figures 4.1-4.4). No explanation for this unexpected observation is found in the literature. A simple model of these reported values of thermal conductivity that assume constant values away from the melting temperature is shown in Figure 4.5. As the temperature of the measurement sample approaches the melting temperature, a sharp rise in the thermal conductivity values is registered. In this chapter, preliminary results of numerical and analytical models of the operation of the THW technique near the melting temperature are reported. Operation of the THW technique under the non-equilibrium condition is not consistent with the idealized theory based on which the transient techniques of measuring thermal conductivity are designed to be applicable. Moreover, the THW technique is ideally-suited to measure the thermal conductivity of a homogenous medium. Therefore, once the assumptions break down and the solid PCM starts transforming into two separate phases, the resulting thermal conductivity quantities are not accurate any longer. In this chapter, an attempt is made to resolve the observed sharp rise issue through adopting analytical and computational methodologies.

The geometry of the model melting problem consists of a solid cylindrical block of radius b with a wire heat source of radius a positioned along the symmetry axis of the block. The idealized theories consider a block that extends to infinity and surrounds a zero-thickness wire as shown in Figure 4.6, whereas using a computational approach and the finite size of actual THW cells necessitates adoption of a finite block radius (b). The block is insulated on the top and bottom planes (z=constant), whereas the outer radial boundary of the medium remains at the initial temperature T_i (below the melting temperature by a very small amount $\varepsilon_T = T_m - T_i$)

(Figure 4.7). For time t>0, thermal energy is released within the highly conductive wire, thus raising its temperature rather evenly. Depending of the initial temperature and properties of the wire and material, a liquid layer might form next to the wire after a time delay. Under this condition, the instantaneous liquid-solid interface is at the radial coordinate s(t) that increases with time.

4.3 Governing Equations

It was assumed that the solid heating wire and the material surrounding it in solid and liquid phases are homogenous and isotropic, and 1-D transient melting process takes place under cylindrical axisymmetry that is governed by conduction. Densities of the liquid and solid phases of materials are generally not equal. However, in this thesis the density variation is ignored. The thermal energy equations for the two-phase medium which needs to be solved in order to obtain the temperature distributions in the liquid and solid phases are as follows.

For the liquid layer formed between the wire and the solid-liquid interface, $a \leq r < s(\mathrm{t}) \quad and \quad \mathrm{t} > 0$

$$(\rho C_p)_l \frac{\partial T_l}{\partial t} = k_l \left(\frac{1}{r} \frac{\partial T_l}{\partial r} + \frac{\partial^2 T_l}{\partial r^2} \right), \tag{4.1}$$

whereas for the solid layer, $s(t) < r < \mathrm{b} \quad and \quad \mathrm{t} > 0$

$$(\rho C_p)_s \frac{\partial T_s}{\partial t} = k_s \left(\frac{1}{r} \frac{\partial T_s}{\partial r} + \frac{\partial^2 T_s}{\partial r^2} \right). \tag{4.2}$$

The thermal energy equation for the wire, $0 < r \leq a \quad and \quad t > 0$, with the constant heat source of $q\left[\frac{w}{m}\right]$ is:

$$(\rho C_p)_w \frac{\partial T_w}{\partial t} = k_w \left(\frac{1}{r}\frac{\partial T_w}{\partial r} + \frac{\partial^2 T_w}{\partial r^2}\right) + \frac{q}{\pi a^2}, \tag{4.3}$$

where the symbols k, ρ and C_p denote the thermal conductivity, density and specific heat, respectively. Subscripts s, l and w stand for solid phase, liquid phase and wire, respectively. Relations 4.1-4.3 are analogous to those of Assael et al. (1998) except for the introduction of the conduction equation for the liquid phase.

At the liquid/solid interface, $r = s(t) \quad and \quad t > 0$,

$$k_s \frac{\partial T_s}{\partial r} - k_l \frac{\partial T_l}{\partial r} = \rho L \frac{ds(t)}{dt} \ . \tag{4.4}$$

in which L stands for the heat of fusion. The detailed procedure of deriving equation (4.4) is given in Appendix A.

These set of equations are subject to the initial and boundary conditions as follows:

For $t = 0$ at $r > 0$ $\qquad T_w = T_s = T_i$

For $t > 0$ at $r = 0$, due to symmetry, $\qquad \frac{\partial T_w}{\partial r} = 0$

For $t > 0$ at $r = b$, $\qquad T_s = T_i$

For $t > 0$ at $r = s(t)$, $\qquad T_s(r,t) = T_l(r,t) = T_m$

For $t > 0$ at $r = a$, $\qquad k_w \left(\frac{\partial T_w}{\partial r}\right)_{r=a} = k_l \left(\frac{\partial T_l}{\partial r}\right)_{r=a}$

and $T_w(a,t) = T_l(a,t)$. (4.5)

4.4 Computational Methodology

4.4.1 Modeling of the commonly-used THW technique using ANSYS® FLUENT

A 1-D transient axisymmetric computational model for the THW technique is considered in this chapter. The governing heat conduction equations in combination with a phase change enthalpy model were solved using the ANSYS® FLUENT software. A solid eicosane cylindrical block was chosen as a case study with a platinum wire heat source positioned along the symmetry axis of the block. The adopted thermo-physical properties of eicosane and platinum wire from literature are given in Table 4.1 and Table 4.2, respectively. The solution domain was insulated on the top and bottom planes, whereas the outer radial boundary of the medium remained at the initial temperature T_i. At $t = 0$, the solid block is at a uniform temperature T_i (below the melting temperature by a very small amount $\varepsilon_T = T_m - T_i$) (Figure 4.7). Thereafter, thermal energy is released within the wire at a constant heating power for a specific time period and thereafter the power supply is turned off (pulse function). The amount of heating power and the total heating time duration, i.e. 1 $\frac{W}{m}$ and 1 second, respectively, were chosen in accordance with the reported practices of actual THW experimental measurement conditions reported by Assael et al. (1998). At the end of the heating period, the thermal conductivity value of the PCM was extracted from the slope of a diagram in which the temperature rise on the surface of the wire ($\Delta T(a,t)$) is plotted against heating time on a logarithmic scale ($\ln t$), in

accordance with the following equation given by Carslaw and Jaeger (1959) for the idealized THW technique:

$$\Delta T(a,t) = \frac{q}{4\pi k} \ln\left(\frac{4\alpha t}{a^2 C}\right), \tag{4.6}$$

where α, k and a represent the thermal diffusivity of the PCM, thermal conductivity of the PCM and radius of the platinum wire, respectively. Furthermore, q is the constant heat source per unit length of the wire, $C = \exp(\gamma) = 1.7811$, and γ is the Euler's constant. The slope of the $\Delta T(a,t)$ versus $ln\, t$ curve is equal to $\frac{q}{4\pi k}$, allowing for extraction of the value of thermal conductivity. The procedure is explained extensively by de Groot et al. (1974), Healy et al. (1976) and Roder (1981).

An enthalpy method within version 13 of the commercial CFD code ANSYS® FLUENT was used to solve the governing equations. The total time of running the program was set to $1\ sec$ with the adopted time step equal to $10\ \mu s$. The adopted values of the under-relaxation factors for the liquid fraction and thermal energy were 0.9 and 1, respectively. In order to satisfy the convergence criteria (10^{-9} for thermal energy equation), the maximum number of iterations for each time step was set to 200. However, the required number of iterations to reach the convergence criteria at each time step was observed to be between 10 and 20. The wire and the solid medium were discretized in the radial direction. Considering the cylindrical coordinate system, the solution domain had a length of 6 mm along the radial direction and 1 mm height in the z-direction. Since the 1-D conduction problem was only studied here, the height of the domain had no influence on the results. The finite axial thickness was only chosen to allow for visual tracking of the liquid/solid interface movement during the simulation time period. The wire region of length 8 μm consists of 20 elements and the solid region of length $5.992\ mm$ was

divided into 230 elements, while the spacings of both groups of elements were non-uniform. The expansion ratios used for laying the non-uniform grids within the wire and solid medium were 1.1 and 1.02, respectively. The aim was to create denser meshes near the wire surface. In the z-direction, the height of both wire and solid domains was uniformly divided into 3 equal elements. The final generated 2-D mesh over the solution domain is shown in Figure 4.8.

4.4.1.1 Enthalpy method

In order to obtain the temperature rise value at each node at each time-step, the aforementioned transient energy equations were discretized through the first order implicit method offered by ANSYS® FLUENT. The enthalpy formulation which is used in this study is categorized under the continuum class of solution methods. The conventional methods of solving phase change problems involve separate energy equations for the solid and liquid domains along with a temperature coupling through the energy balance equation at the moving interface, as discussed in the previous section. This kind of problem formulation would be difficult to handle with the finite-difference solution algorithms. However, using the enthalpy formulation plus the temperature condition, a single energy equation will represent both the solid and liquid phases. As a result, any numerical procedure can readily be utilized such as the finite element method (FEM) or the finite-difference solution scheme. Shamsunder and Sparrow (1975) proved that the unique enthalpy formulation of the conduction energy equation:

$$\nabla \cdot (k \nabla T) = \rho \frac{\partial H(T)}{\partial t} \tag{4.7}$$

with $H(T)$, J/kg being the temperature-dependent enthalpy per unit mass, is equivalent to the conventional temperature-form with separate equations for each phase (Eqs. 4.1 and 4.2). The advantage is that both explicit and implicit finite-difference methods can be used for solving the phase change phenomenon with the aid of the enthalpy formulation. The implicit method was adopted in this study as suggested by Özişik (1993), due to its ability to operate with different time step values without any limitation of the stability criterion. In other words, the technique is always stable regardless of the time step size. Using the implicit scheme, the finite-difference approximation of the enthalpy formulation is:

$$k\frac{T_{i-1}^{n+1}-2T_i^{n+1}+T_{i+1}^{n+1}}{(\Delta r)^2}=\rho\frac{H_i^{n+1}-H_i^n}{\Delta t}\,, \tag{4.8}$$

with n and i representing indices denoting time and space-related discretized values, respectively. Concerning pure crystalline materials, e.g. water, eicosane, etc., the phase change phenomenon occurs at a distinct melting temperature T_m (Figure 4.9). Consequently, a sharp moving interface will separate the liquid and solid domains and there would be no two-phase (mushy) region in between.

Solid state of a material at temperature T holds sensible heat per unit mass $C_p(T-T_m)$, whereas in the liquid phase, the material includes a latent heat L per unit mass plus the aforementioned sensible heat. Therefore, the enthalpy function $H(T)$, J/kg , can be written as a function of temperature:

$$H_s(T)=(C_p)_s(T-T_m)\,, \qquad \text{for} \qquad T<T_m\,,$$

$$H_l(T)=(C_p)_l(T-T_m)+L\,, \qquad \text{for} \qquad T>T_m\,. \tag{4.9}$$

4.4.2 Exact solution of an ideal melting problem

An exact solution for melting of an infinite domain that contains a zero-thickness heating wire is derived and proposed by Paterson (1952), hereto called the Paterson Model. Formulation for this problem and its solution are given in Appendix B with the notations for the relevant quantities matching the related solidification (freezing) problem described by Özişik (1993). The pertinent equations are coded and solved with the aid of the MATLAB software, and the code is given in Appendix C. The objective was to verify the interface temperature outputs of the FLUENT model in the case that phase change occurs.

Having discussed the various analytical and numerical models, a summary of the various aspects of the models are given in Table 4.3.

4.5 Results and Discussions

4.5.1 Benchmarking of the utilized FLUENT model against the ideal THW theory (without phase change)

The mathematical formulation by Carslaw and Jaeger (1959), i.e. equation (4.6), for prediction of the temperature rise on the surface of the wire of the transient hot wire (THW) technique, assumes an ideal perfect wire conductor which is surrounded by an infinite medium. An attempt was made to verify the accuracy of the results of the adopted ANSYS® FLUENT model versus the ideal limiting-case model of Carslaw and Jaeger (1959). To achieve this, the value of thermal conductivity of the wire was set to a very large number, i.e. 1000 times bigger

than the thermal conductivity of platinum (71.7 W/mK, (Yaws, 1995)). For the next case study, the actual thermal conductivity value of platinum wire was assigned (Yaws, 1995). The ideal theory is only applicable for homogenous media in which phase transition does not occur during the temperature rise. That is why in both cases, the initial temperature was selected as $T_i = 306\,K$ to ensure that the final temperature will not reach the melting point of eicosane, i.e. $T_m = 310\,K$. The FLUENT-based temperature rise versus time results are compared to the predictions of the ideal Carslaw and Jaeger (1959) model in Figure 4.10. Comparing the temperature difference of each FLUENT case with the ideal model at t=1 s, there are 2.17% and 0.01% errors corresponding to wire thermal conductivities of 71.7 and 71700 W/mK, respectively. It also confirmed that as the adopted thermal conductivity value of the wire approaches infinity which theoretically is called a perfect conductor, the temperature rise behavior is very similar to the prediction based on the model of Carslaw and Jaeger (1959). It is observed that the average temperature rise within the wire is very close to the amount of temperature rise on the wire surface. Note that the theoretical temperature rise of 1.6 °C in Figure 4.10 is markedly lower than $\Delta T = \frac{Q}{\rho V C_p} = 1784.51\,°C$ that is the limiting case temperature rise for an insulated platinum wire. In this relation, Q, ρ, V and C_p stand for heating power, density, volume and specific heat of the wire, respectively.

4.5.2 Benchmarking of the utilized FLUENT model against the Paterson's melting problem

Paterson (1952) derived an exact solution for melting of an infinite domain due to a zero-thickness line heat source of strength $q, W/m$ positioned at $r = 0$. The solid body is initially at uniform temperature T_i lower than the melting point (T_m) of the medium. Thereafter, the heat

source is turned on to continuously release thermal energy. Consequently, melting begins at $r = 0$ and the liquid/solid interface starts to move in the radial direction (Figure 4.6). The analytical model of Paterson (1952) predicts the instantaneous temperatures for both liquid and solid domains and also the location of solid/liquid interface at any time instant (Appendix B). The solutions for the temperature distributions within the liquid and solid domains are:

$$T_l(r,t) = T_m + \frac{q}{4\pi k_l}\left[-Ei\left(-\frac{r^2}{4\alpha_l t}\right) + Ei(-\lambda^2)\right] \quad \text{for} \quad 0 < r < s(t), \tag{4.10}$$

$$T_s(r,t) = T_i - \frac{T_i - T_m}{Ei(-\lambda^2\alpha_l/\alpha_s)} Ei\left(-\frac{r^2}{4\alpha_s t}\right) \quad \text{for} \quad s(t) < r < \infty, \tag{4.11}$$

where the exponential-integral function is defined as (Abramowitz and Stegun, 1965):

$$-Ei(-x) \equiv E_1(x) = \int_x^\infty \frac{e^{-u}}{u} du = \int_1^\infty \frac{e^{-xt}}{t} dt \quad \text{for} \quad x > 0. \tag{4.12}$$

The location of the liquid/solid interface will be determined through:

$$s(t) = 2\lambda(\alpha_l t)^{1/2} \tag{4.13}$$

where λ is a positive constant that needs to be calculated by solving the following transcendental equation (Paterson, 1952):

$$\frac{q}{4\pi} e^{-\lambda^2} + \frac{k_s(T_m - T_i)}{Ei(-\lambda^2\alpha_l/\alpha_s)} e^{-\lambda^2\alpha_l/\alpha_s} = \lambda^2 \alpha_l \rho L \tag{4.14}$$

Once λ is obtained, the location of the liquid/solid interface can easily be tracked versus time using eq. (4.13). Furthermore, the temperature distribution functions for both liquid and solid regions will also be known through equations (4.10) and (4.11).

In this study, a line heat source of strength $q = 1\,W/m$ is used in accordance with operation of the commonly-used THW technique (Assael et al., 1998). The solution domain of interest is the same as that described for the FLUENT model, except that in this model the wire possesses a zero thickness. Solid eicosane is initially at uniform temperature $T_i = 309.9\,K$ that is a bit lower than its melting point ($T_m = 310\,K$). Figure 4.11 (a) exhibits variation of the transcendental function (eq. (4.14)) versus λ. Using the Newton-Raphson root-finding algorithm (Quarteroni et al., 2007) for solving the transcendental equation (4.14) (Appendix C), the pertinent value of λ is found. Knowing the value of λ, the location of the liquid/solid interface versus time based on Eq. (4.13) is shown in Figure 4.11 (b). The contour of temperature distributions within the liquid and solid domains versus the melting time period and location is exhibited in Figure 4.12 (a). The solid black line in the figure is the instantaneous location of the liquid/solid interface. In order to verify the accuracy of the FLUENT model against the analytical solution according to Paterson (1952) under phase change condition, a case study was run with the same initial and boundary conditions using ANSYS® FLUENT. The plots of the temperature rise on the surface of the wire which are obtained from both Paterson (1952) and FLUENT models versus heating time (i.e., $1\,sec$) are shown in Figure 4.12 (b). Since $r = 0$ is a singular point in the model of Paterson (1952), three other locations near $r = 0$, between $r = 2\ \mu m$ and $r = 3\,\mu m$ away from the wire, were chosen as the imaginary locations of the surface of the wire for obtaining the temperature rise data. The trends of the temperature rise curves predicted by both models are very similar and the observed deviations are less than 0.5%.

So far, the benchmarking of the adopted ANSYS® FLUENT model is performed under both conditions without and with phase change. The remaining part of this chapter is devoted to case studies for which the FLUENT model results are used for prediction of values of thermal

conductivity. In effect, the most general case involving various dimensionless groupings listed in the bottom row of Table 4.3 along with a finite-size wire and finite medium domain are considered.

4.5.3 Thermal conductivity predictions using the FLUENT model

4.5.3.1 Two benchmarking case studies without phase change

4.5.3.1.1 Thermal conductivity prediction in the solid phase

For this case, solid eicosane is initially at a uniform temperature $T_i = 306\,K$ which is lower than the melting temperature by four degrees and is then continuously heated for $1\,sec$. The initial temperature is selected such that the final temperature does not reach the melting point. The initially-assigned thermal conductivity value for eicosane in the solid phase is set to $k_s = 0.42\ \frac{W}{mK}$ (Stryker and Sparrow, 1990). The plot of the temperature rise (ΔT) on the wire surface versus $\ln t$ is shown in Figure 4.13. In plotting this figure, ten temperature rise data points on each of the two ends were eliminated, as suggested by de Groot et al. (1974). In effect, the temperature rise data did not begin at its initial value of zero. Discarding of these data points did not affect the value of the slope of the curve fit that is used to extract the value of thermal conductivity. Similar procedure was applied to all the subsequent temperature rise versus $\ln(t)$ plots that follow. Using Eq. (4.6) due to Carslaw and Jaeger (1959), the predicted thermal conductivity value based on the slope the least-squares curve fit to the FLUENT data of Figure

4.13 is equal to $(k_s)_{predicted} = 0.4242\ \frac{W}{mK}$. Therefore, the extracted thermal conductivity value based on the FLUENT model prediction is only off from the assigned value by 1%.

4.5.3.1.2 Thermal conductivity prediction in the liquid phase

In a similar case study, liquid eicosane is initially at a uniform temperature $T_i = 313\ K$ which is higher than the melting temperature by three degrees and is then heated for $1\ sec$. The initially-assigned thermal conductivity value for eicosane in the liquid state is set to $k_l = 0.148\ \frac{W}{mK}$ (Yaws, 1995). The plot of the temperature rise (ΔT) on the wire surface versus $\ln t$ is shown in Figure 4.14. Using Eq. (4.6), the predicted thermal conductivity value based on the slope least-squares curve fit of Figure 4.14 is equal to $(k_l)_{predicted} = 0.1468\ \frac{W}{mK}$. Therefore, the extracted thermal conductivity value based on the FLUENT model prediction deviates from the assigned value by only 0.81%.

Considering Figures 4.13 and 4.14, one might think that since the thermal conductivity of solid eicosane is higher than liquid phase (Table 4.1), the amount of temperature rise (ΔT) in solid phase (Figure 4.13) should be higher than that of liquid phase (Figure 4.14). However, it should be noted that ΔT curves presented in Figures 4.13 and 4.14 represent the temperature rise on the wire surface (r=a). Since thermal conductivity of eicosane in the liquid state is lower than that of solid state by a factor of three, released thermal wave from the wire cannot penetrate into the liquid medium as fast as in solid domain. Therefore, during the monitored heating time period (same as temperature recording period), a big portion of the total heat source will increase the temperature of the wire itself which is finally observed on the wire surface.

4.5.3.2 The effect of the initial solid state temperature on the predicted thermal conductivity value with phase change

As discussed in section (4.2), in using the transient hot wire, many researchers have observed a sharp rise in the thermal conductivity values as the temperature approaches the melting point of the PCM (e.g., Wang et al., 2008, 2009, 2010a, and 2010b) (Figures 4.1-4.4). In this section, it is aimed to possibly resolve the observed sharp rise issue through the adopted FLUENT model.

Five cases with different solid state initial temperatures are studied. The initial temperatures are selected in order to assure occurrence of phase transition during the heating time period (i.e. $1\,sec$). The selected solid state initial temperatures are equal to $T_i = 309, 309.5, 309.7, 309.8\ and\ 309.9\ K$, corresponding to $\varepsilon_T = 1, 0.5, 0.3, 0.2\ and\ 0.1\ °C$, respectively. Following the same procedure as discussed in the previous sections, the predicted thermal conductivity values are given in Table 4.4 and exhibited in Figure 4.15. Furthermore, the corresponding plots of the temperature rise (ΔT) on the wire surface versus $\ln t$ along with the respective least-squares curve fits are shown for these five cases in Figure 4.16-4.20. Depending on the initial temperature, the derived "effective thermal conductivity" values are lower than the assigned thermal conductivity of the solid state (0.42 W/mK) by 60.88-62.12%. The results also suggest that there is a monotonic dependence of the predicted thermal conductivity value on the initial temperature of the medium. To start with, there is a composite system that contains the wire and the solid PCM. Upon heating of the wire, a portion of the diffused thermal energy away from the wire is used to turn the solid layer (0.42 W/mK) next to the wire into liquid that has a lower thermal conductivity (0.148 W/mK). In effect, less heat diffuses in the radial direction through a less-conductive liquid layer, and a portion of total heat source fails to reach

the solid region. The effective thermal conductivity of the composite is observed to be a value between the thermal conductivity of the liquid and solid phases. It is observed that there is no sharp rise in thermal conductivity values as the temperature approaches the melting point of eicosane. All the estimated values are between the initially-assigned thermal conductivity values for the liquid and solid states.

Furthermore, variations of the temperature rise versus the heating time on the wire surface for two cases with and without the phase change with the initial temperature of T_i=309 K and T_i=306 K, are exhibited in Figure 4.21. Contrary to temperature rise versus $\ln t$ plots presented above, no data on both ends of the heating period were not discarded. Early on the temperature rise curves are nearly identical since the two systems are very similar in regard to the thermal conductivity of the medium surrounding the wire. For the case with the initial temperature of T_i=309 K, melting on the surface of the wire is sensed at about 0.02 seconds. This gives rise to a higher value of the surface temperature rise at subsequent time instants due to presence of a widening liquid layer surrounding the wire that possesses a lower thermal conductivity. In effect, after 1 second the temperature rise for the case in which melting occurs is higher than the solid eicosane case by about 1 ℃. Once a liquid region forms around the wire, due to its lower thermal conductivity, a great portion of total heat source fails to reach the nearby solid region and therefore a higher amount of temperature rise is observed on the wire surface.

4.6 Summary

With the aid of the ANSYS® FLUENT software, a 1-D transient conduction problem was formulated and solved over a finite cylindrical domain without and with phase transition. The ultimate goal was to model the performance of the THW technique near the melting temperature of the medium. The defined FLUENT model was first successfully verified against the ideal transient hot wire model of Carslaw and Jaeger (1959) for a perfect conductor with a 0.01% error in the values of monitored temperatures. Another benchmarking was performed against the analytical solution of Paterson (1952) for a model melting problem to verify the adopted enthalpy method in the FLUENT model. The registered error for the monitored temperatures was less than 0.5%.

Thereafter, focusing on the FLUENT model, thermal conductivity predictions in both liquid and solid phases were performed in the absence of phase change. The difference between the extracted thermal conductivity values and the initially-assigned values was less than 1% and 0.81% for solid and liquid phases, respectively. Finally, the effect of the initial solid state temperature on the predicted thermal conductivity with phase change was explored. Five cases were considered. The attempt was to study if any sharp rise in thermal conductivity values will occur near the melting point of the PCM. It was shown that there is no abrupt behavior as the temperature approaches the melting point of eicosane and all the predicted thermal conductivity values are between the assigned values of the liquid and solid states.

Table 4.1 Thermo-physical properties of eicosane ($C_{20}H_{42}$) adopted from literature

Property/Reference	**Value**
ρ (kg/m^3) **(Stryker and Sparrow, 1990)**	840
$(C_p)_s$ and $(C_p)_l$ (J/kgK) **(Humphries and Griggs, 1977)**	1,920 and 2,460
k_s and k_l (W/mK) **(Stryker and Sparrow, 1990)** **(Yaws, 1995)**	0.42 and 0.148
L (J/kg) **(Hale et al., 1971)**	247,000
T_m (K) **(Hale et al., 1971)**	310

Table 4.2 Thermo-physical properties of platinum (Pt) adopted from literature

Property/Reference	**Value**
ρ (kg/m^3) **(Grigoriev and Meilikhov, 1997)**	21,450
C_p (J/kgK) **(Goldsmith et al., 1961)**	130
k (W/mK) **(Yaws, 1995)**	71.7

Table 4.3 Specifications of the adopted analytical/computational methodologies

	Carslaw and Jaeger (1959)	***Paterson (1952)***	***FLUENT***
Material Domain	$a \to \infty$ (infinite)	$0 \to \infty$ (infinite)	$a \to b$ (finite)
Wire Diameter	$2a$	0	$2a$
No. of Phases	One Phase	Two Phases $\rho_s = \rho_l$	Two Phases $\rho_s = \rho_l$
Phase Change Applicability	No	Yes	Yes
Dimensionless Groups	$\frac{T_m - T_i}{T_i}$, $\frac{q}{kT_i}$	$\frac{T_m - T_i}{T_i}$, $\frac{q}{k_l T_i}$, $\frac{\alpha_l}{\alpha_s}$, Ste$\equiv \frac{(C_p)_l T_i}{L}$	$\frac{T_m - T_i}{T_i}$, $\frac{q}{k_l T_i}$, $\frac{\alpha_l}{\alpha_s}$, Ste$\equiv \frac{(C_p)_l T_i}{L}$, $\frac{a}{b}$, $\frac{k_s}{k_l}$, $\frac{\alpha_w}{\alpha_l}$, $\frac{k_w}{k_l}$

Table 4.4 Predicted thermal conductivity data versus initial solid state temperature of eicosane using the FLUENT model

T_i (K)	k_s (W/mK) (Stryker and Sparrow, 1990)	$(k_s)_{predicted}$ (W/mK) FLUENT
309	0.42	0.1591 (62.12% error)
309.5	0.42	0.1613 (61.60% error)
309.7	0.42	0.1624 (61.33% error)
309.8	0.42	0.1631 (61.17% error)
309.9	0.42	0.1643 (60.88% error)

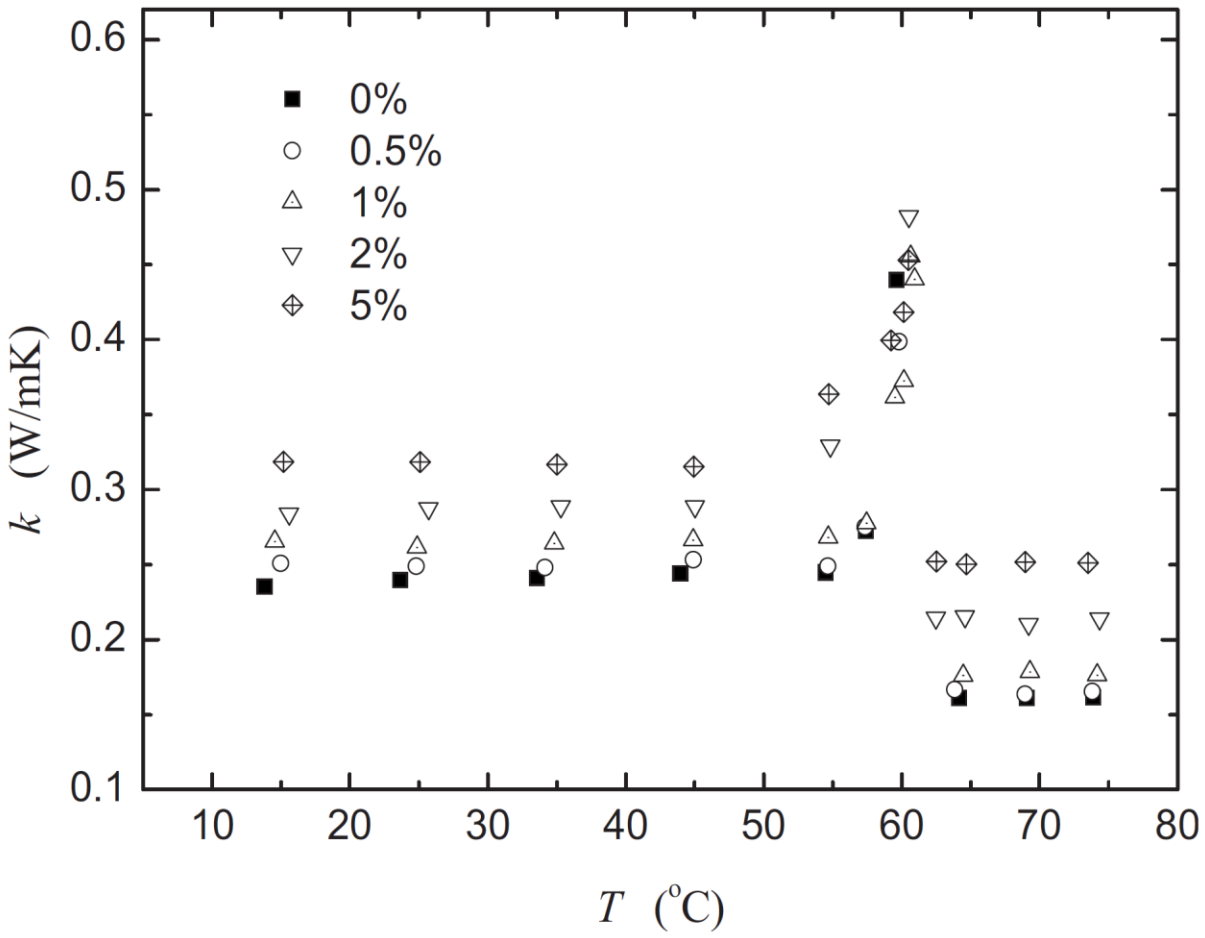

Figure 4.1 Measured thermal conductivity of palmitic acid (PA)/CNT colloids in both solid and liquid states versus temperature for different loadings of nanotubes; MT of PA is 62.5-64 ℃ (Wang et al., 2008)

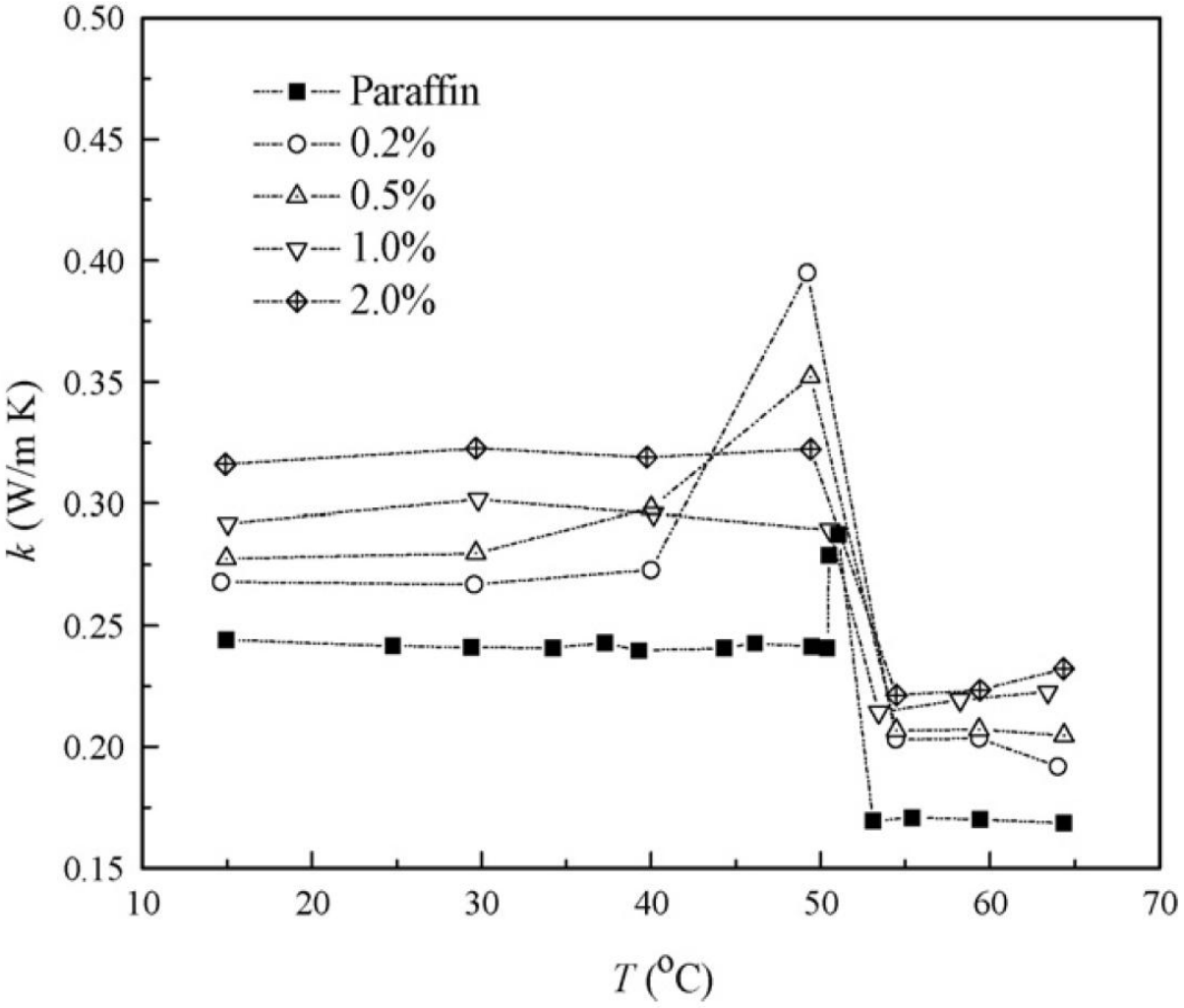

Figure 4.2 Thermal conductivity of multi-walled carbon nanotube-enhanced paraffin wax in both phases as a function of temperature and various loadings of nanotubes; MT of paraffin wax is 53 ℃ (Wang et al., 2009)

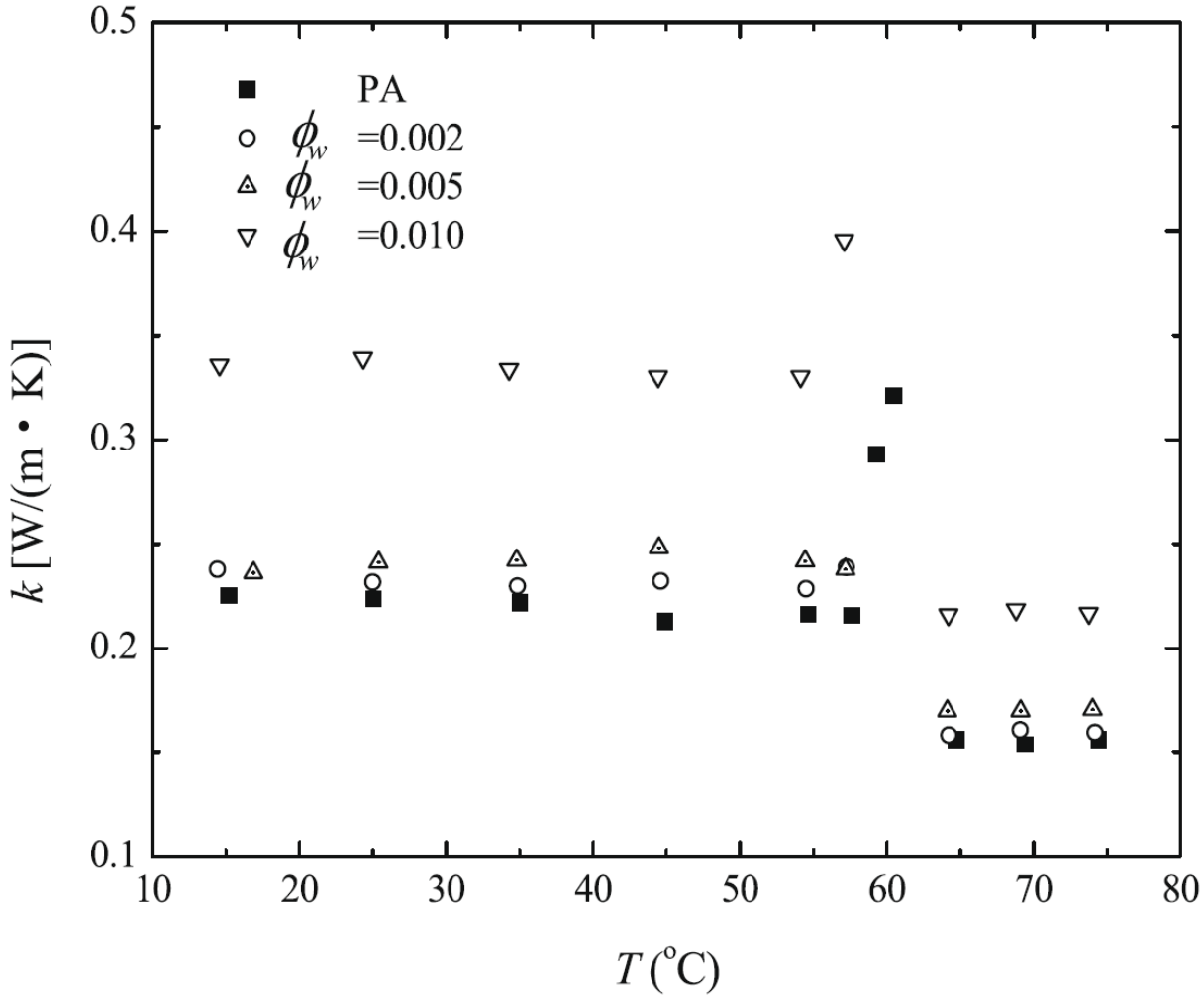

Figure 4.3 Thermal conductivity of palmitic acid (PA)/ treated CNTs (TCNTs) colloids in both phases a function of temperature and various loadings of nanotubes; MT of PA is 62.4 ℃ (Wang et al., 2010a)

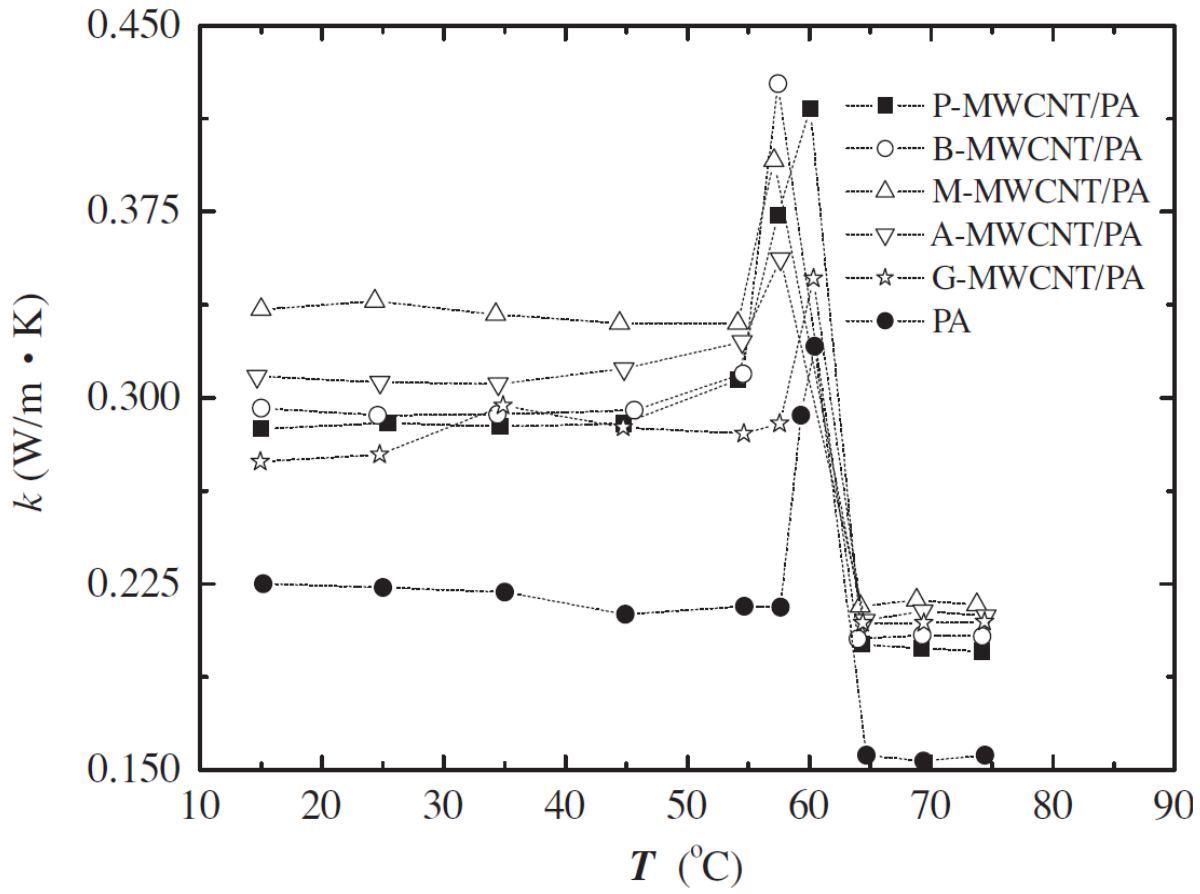

Figure 4.4 Measured thermal conductivity of 1 wt% palmitic acid (PA)/MWCNT composite in both solid and liquid states versus temperature for different types of treated MWCNT; MT of PA is 62.5-64 ℃ (Wang et al., 2010b)

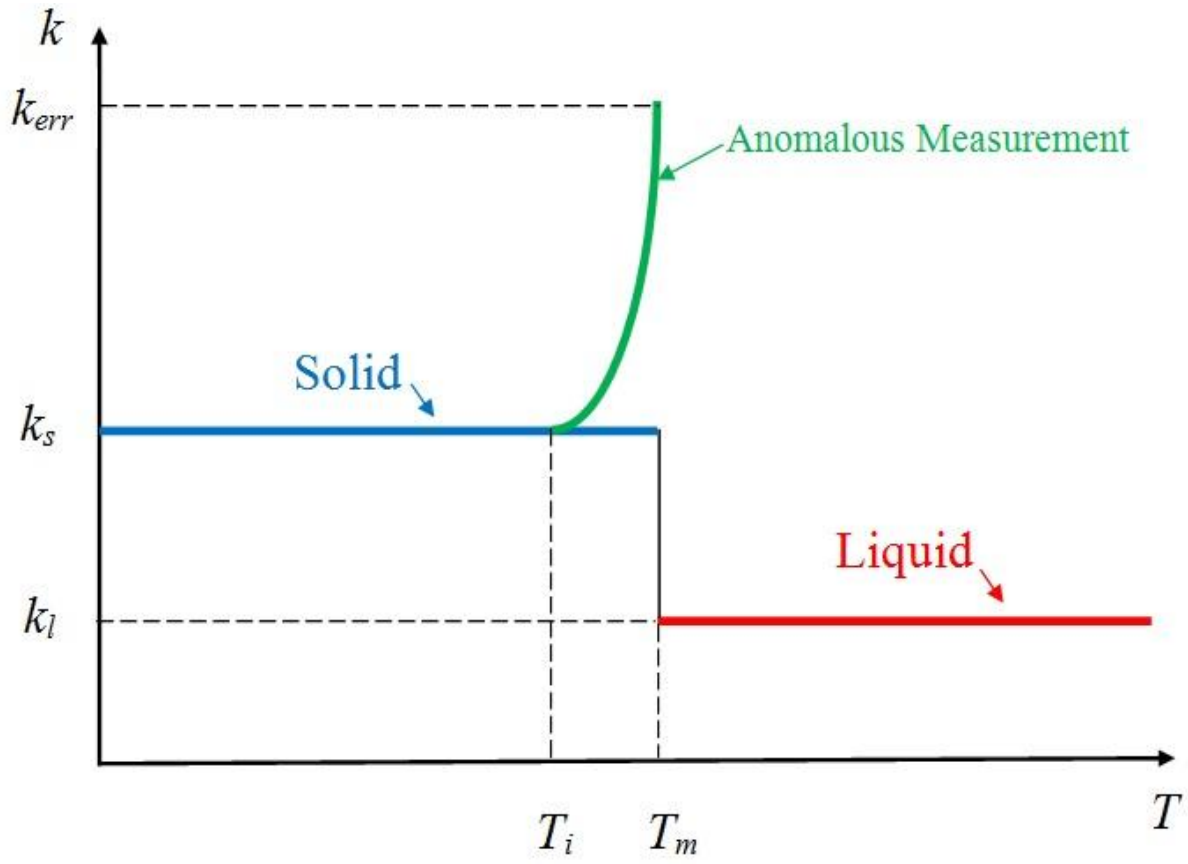

Figure 4.5 Schematic diagram of the anomalous experimental measurement of the thermal conductivity near the melting temperature using the transient methods

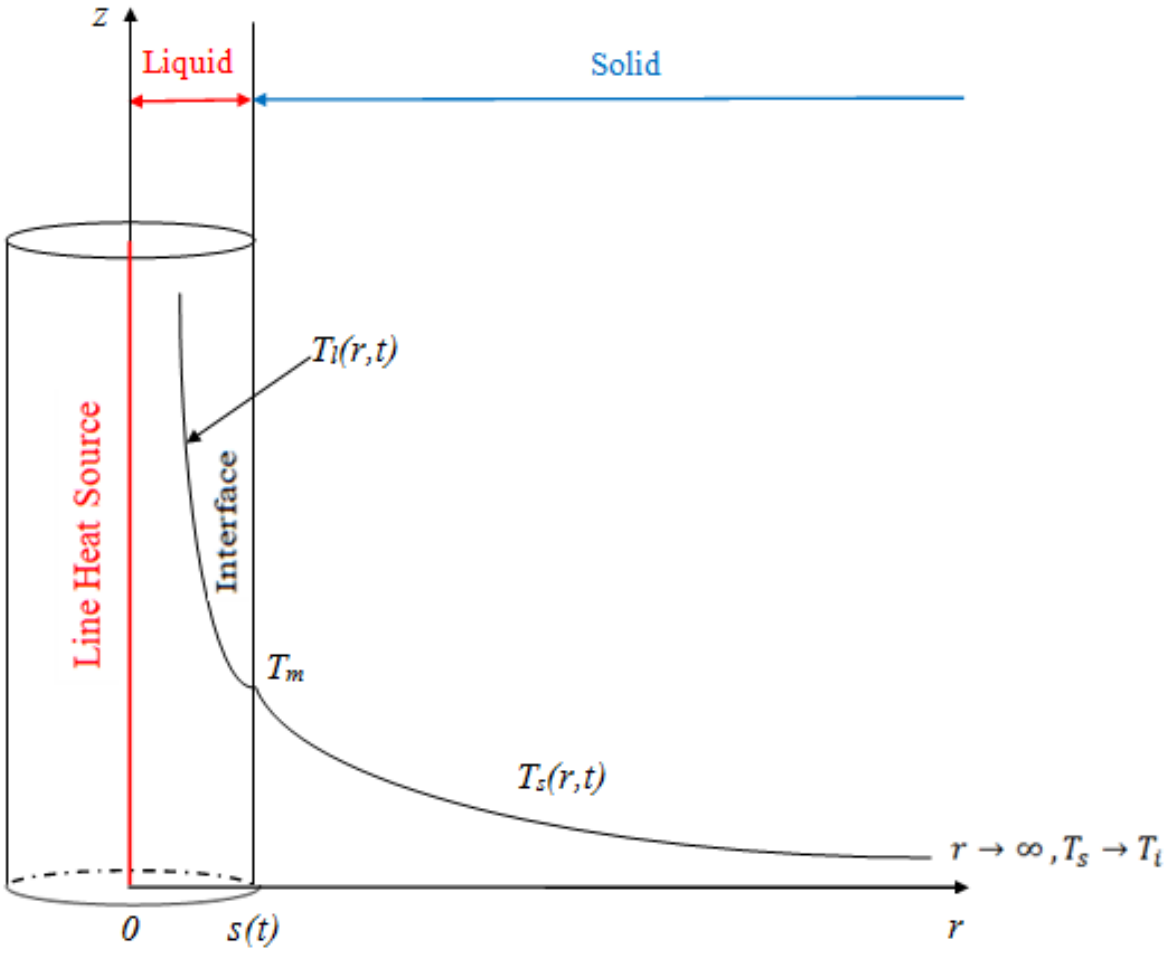

Figure 4.6 Schematic figure of melting of an infinite medium with a zero-thickness line heat source positioned along the symmetry axis (r=0)

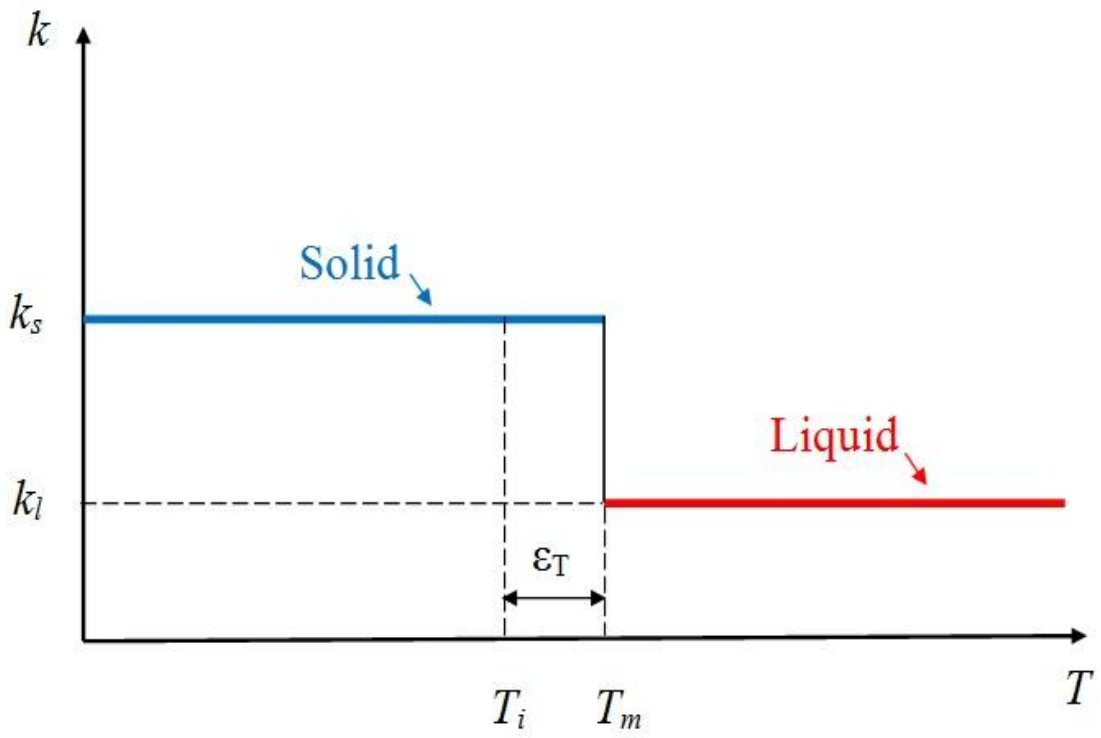

Figure 4.7 Schematic diagram of the assigned thermo-physical properties of the model material analyzed with the computational model of the THW technique

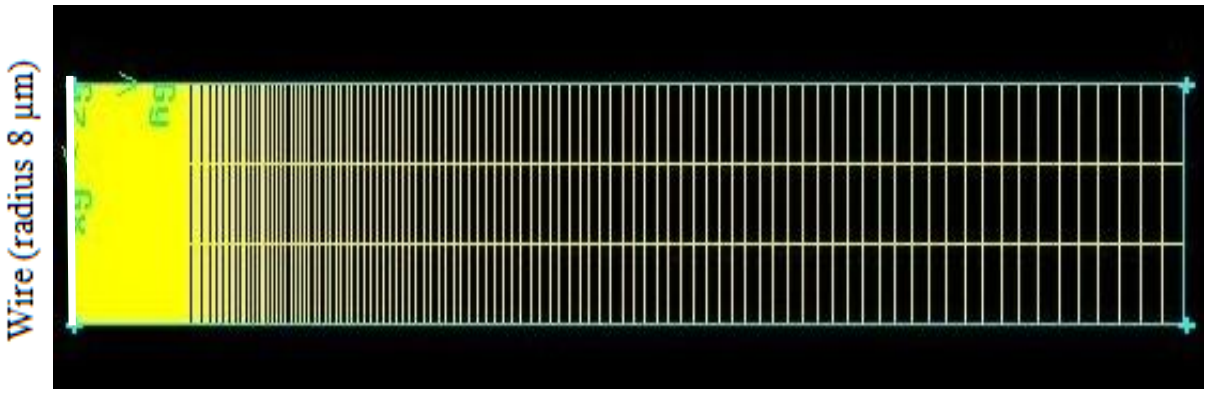

Figure 4.8 Generated 2-D mesh for the solution domain that consists of a thin wire of radius of 8 microns positioned along the vertical direction and the initially-solid material

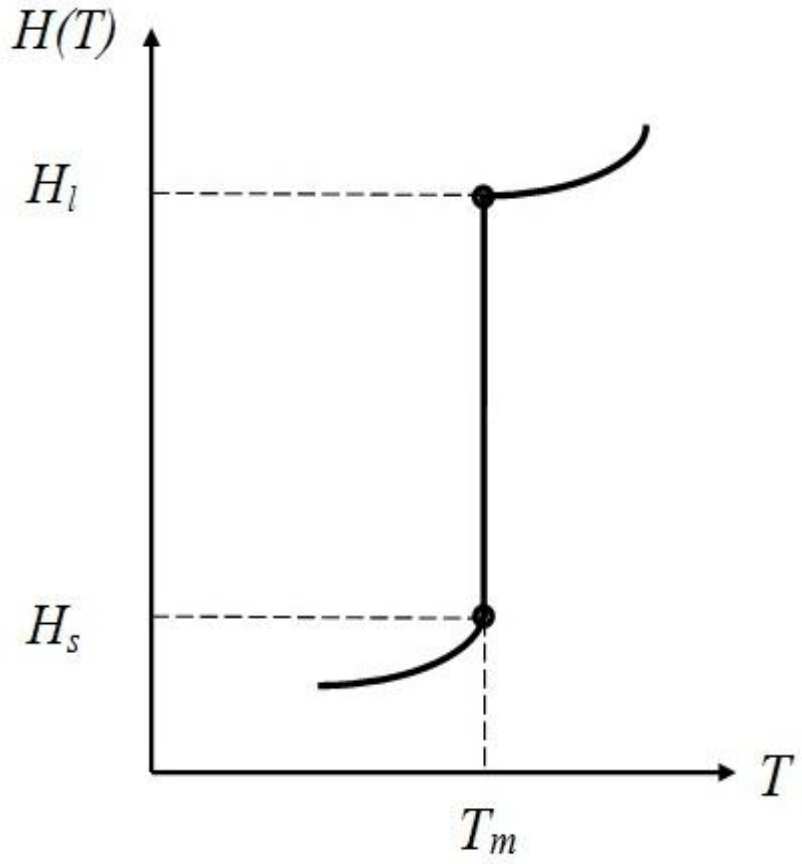

Figure 4.9 Enthalpy-temperature relationship for a pure material

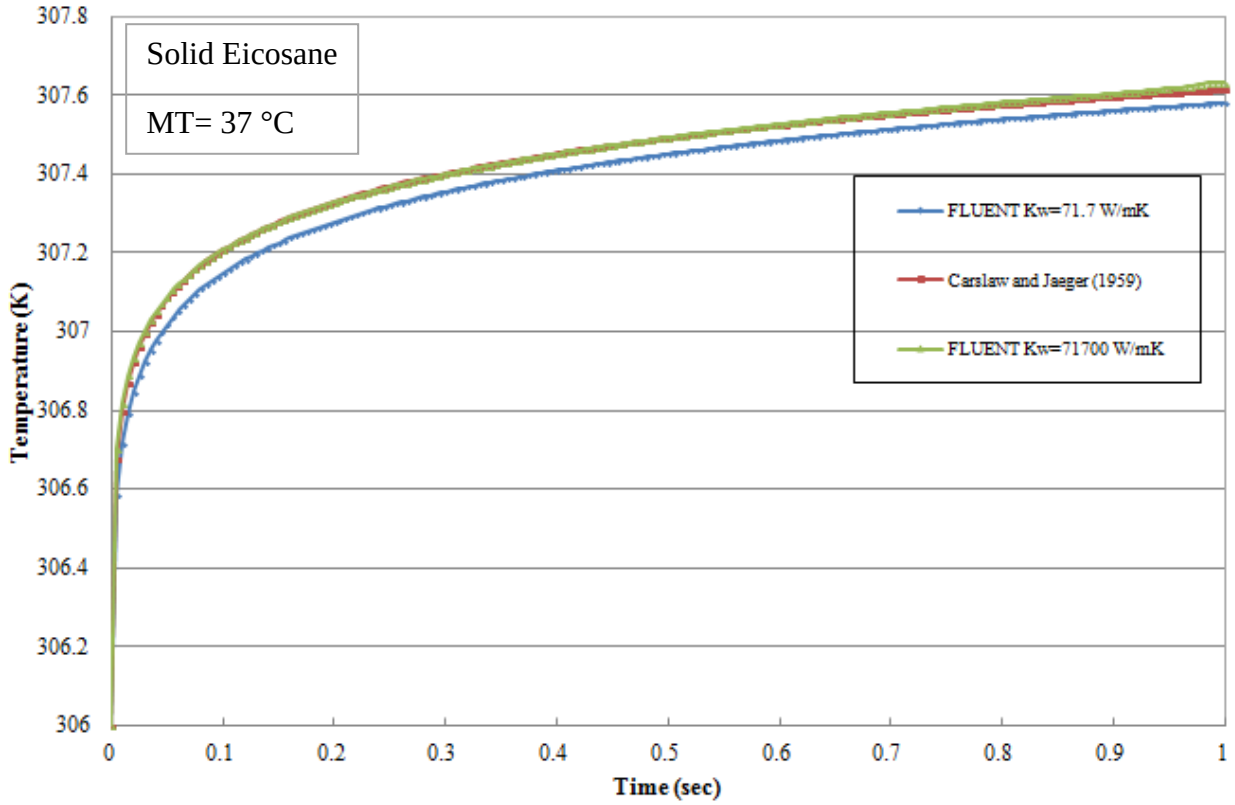

Figure 4.10 Transient temperature rise at the interface of the platinum wire-eicosane versus the heating time predicted by the FLUENT model and compared to the ideal THW theory by Carslaw and Jaeger (1959); Also shown are predictions of the FLUENT model with thermal conductivity of the wire set to 1000 times that of platinum

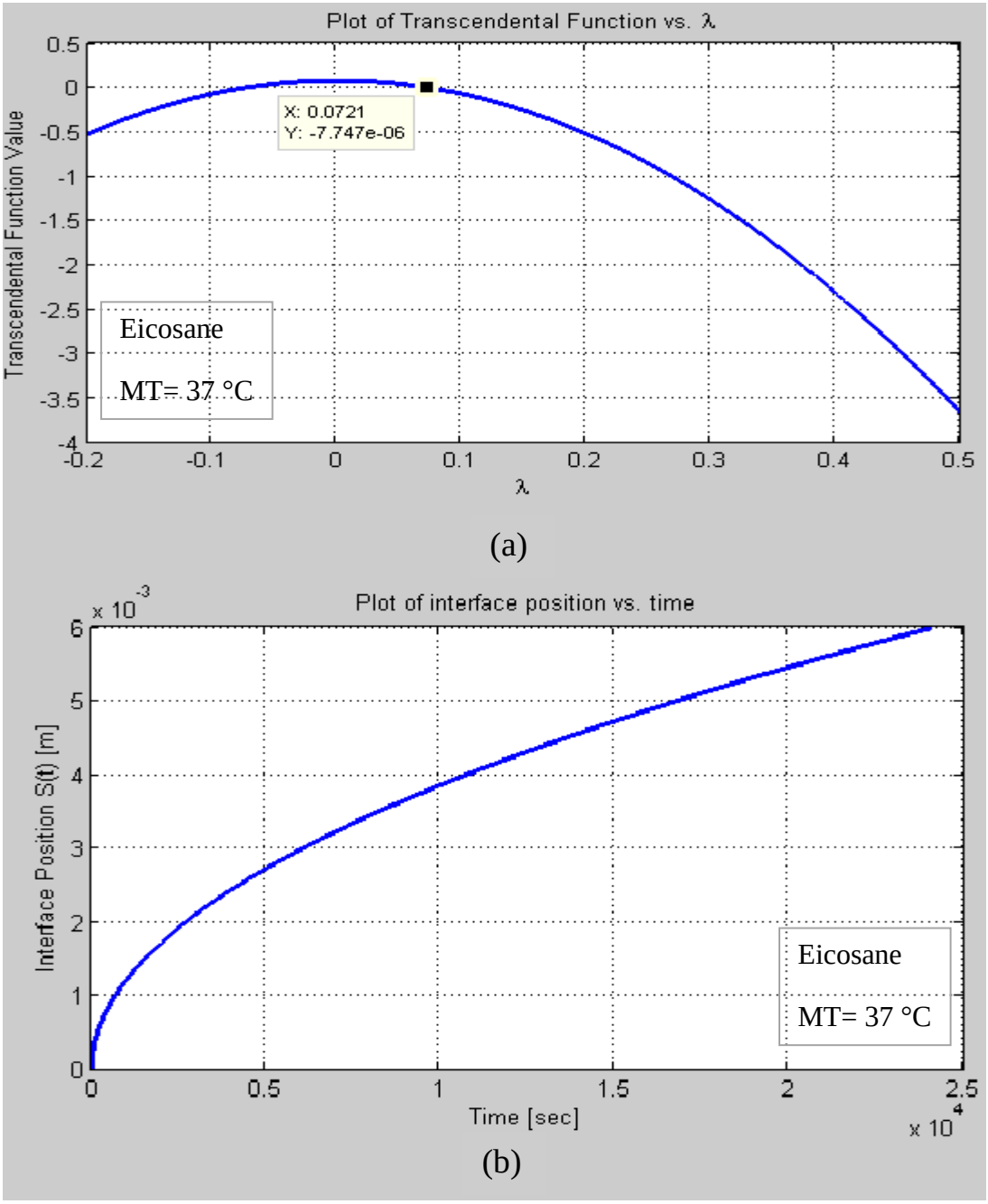

Figure 4.11 Plots of (a) the transcendental function (4.14) versus λ, and (b) the position of the liquid-solid interface versus time, corresponding to melting problem of Paterson (1952)

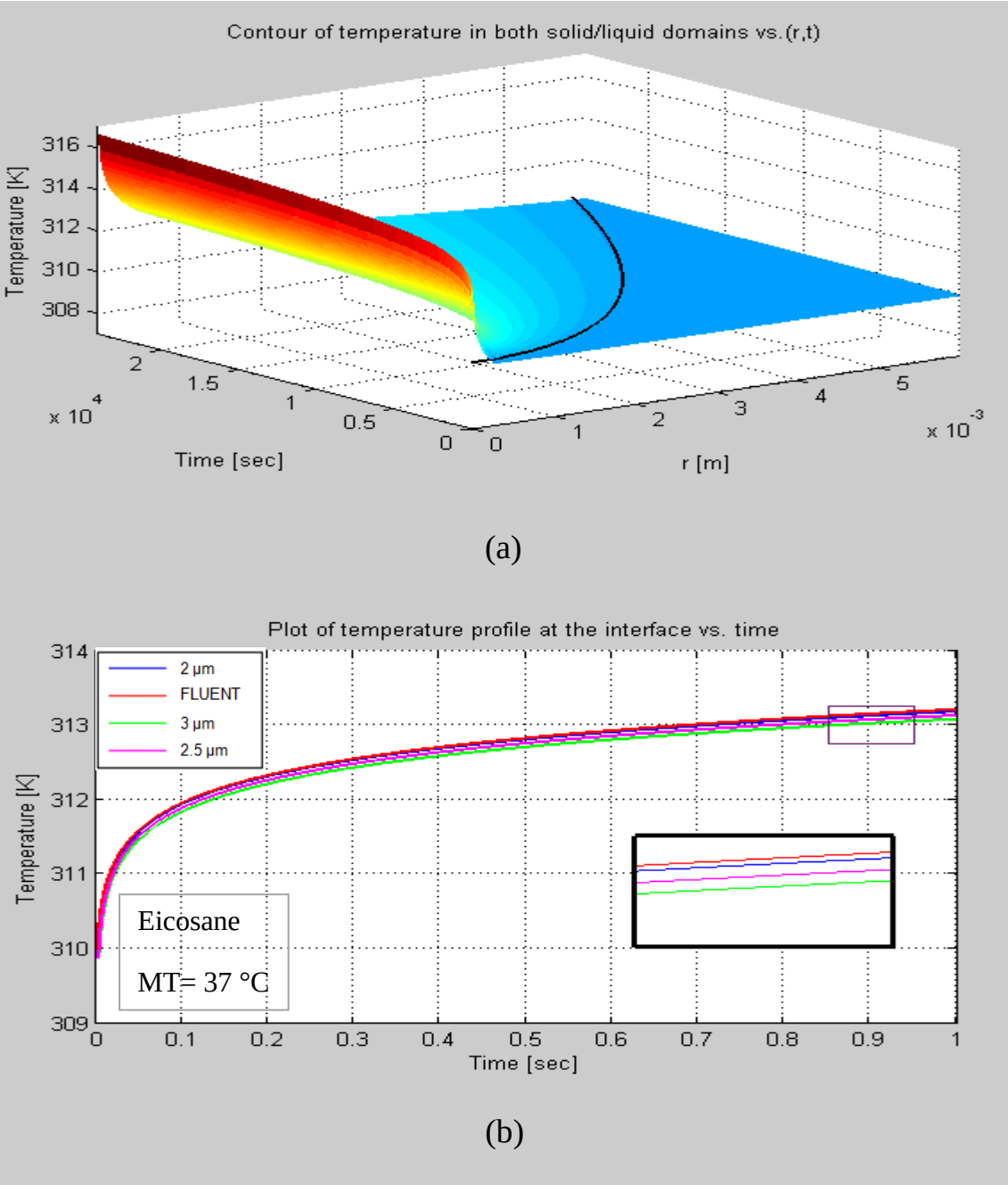

Figure 4.12 (a) Contours of temperature in both solid and liquid domains versus time and location, and (b) temperature rise curves on the wire surface versus time according to FLUENT along with temperature rise predictions near r=0 based on the model of Paterson (1952)

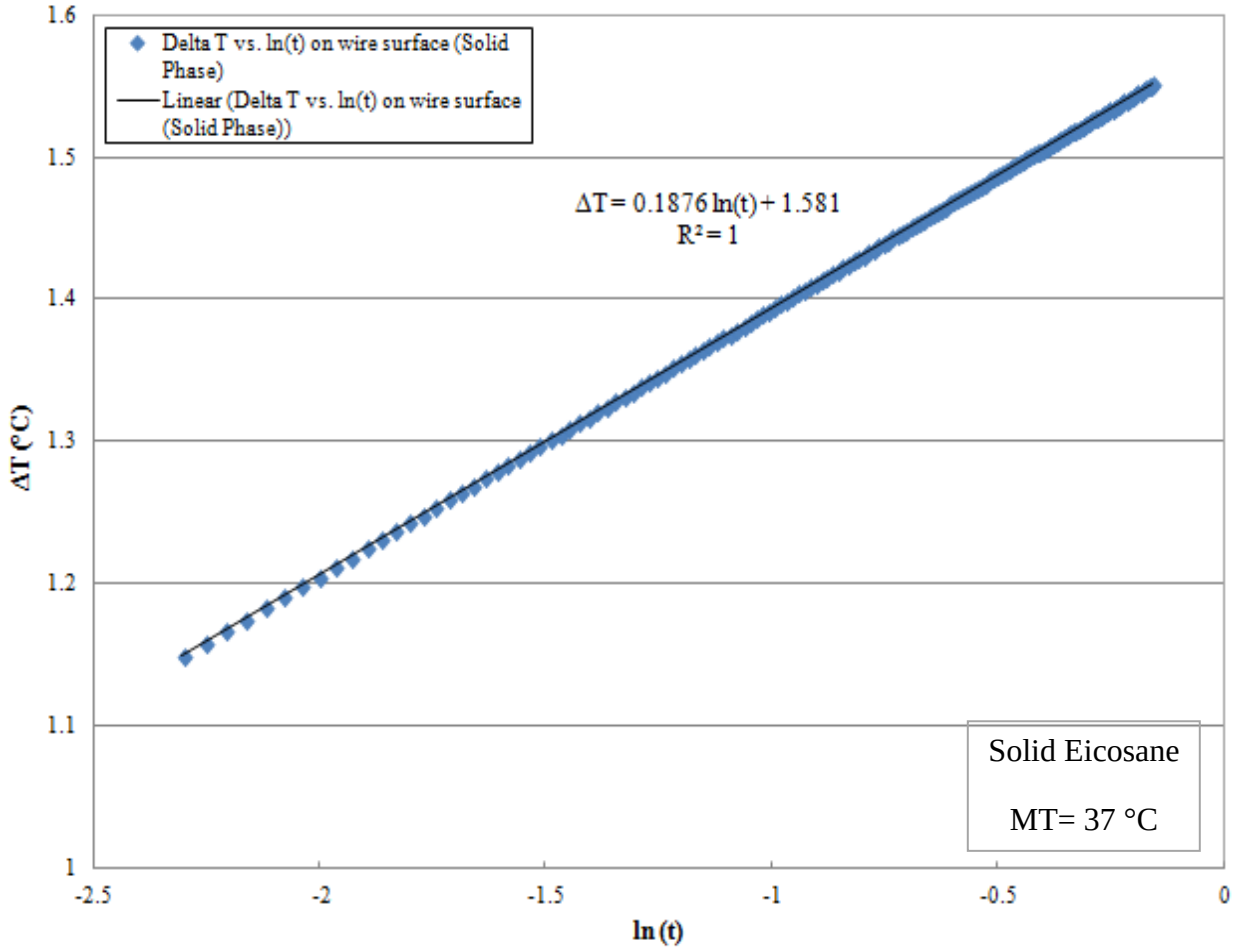

Figure 4.13 Plot of the solid phase eicosane temperature rise on the surface of the wire versus natural logarithm of time with an initial temperature of T_i=306 K using the FLUENT model

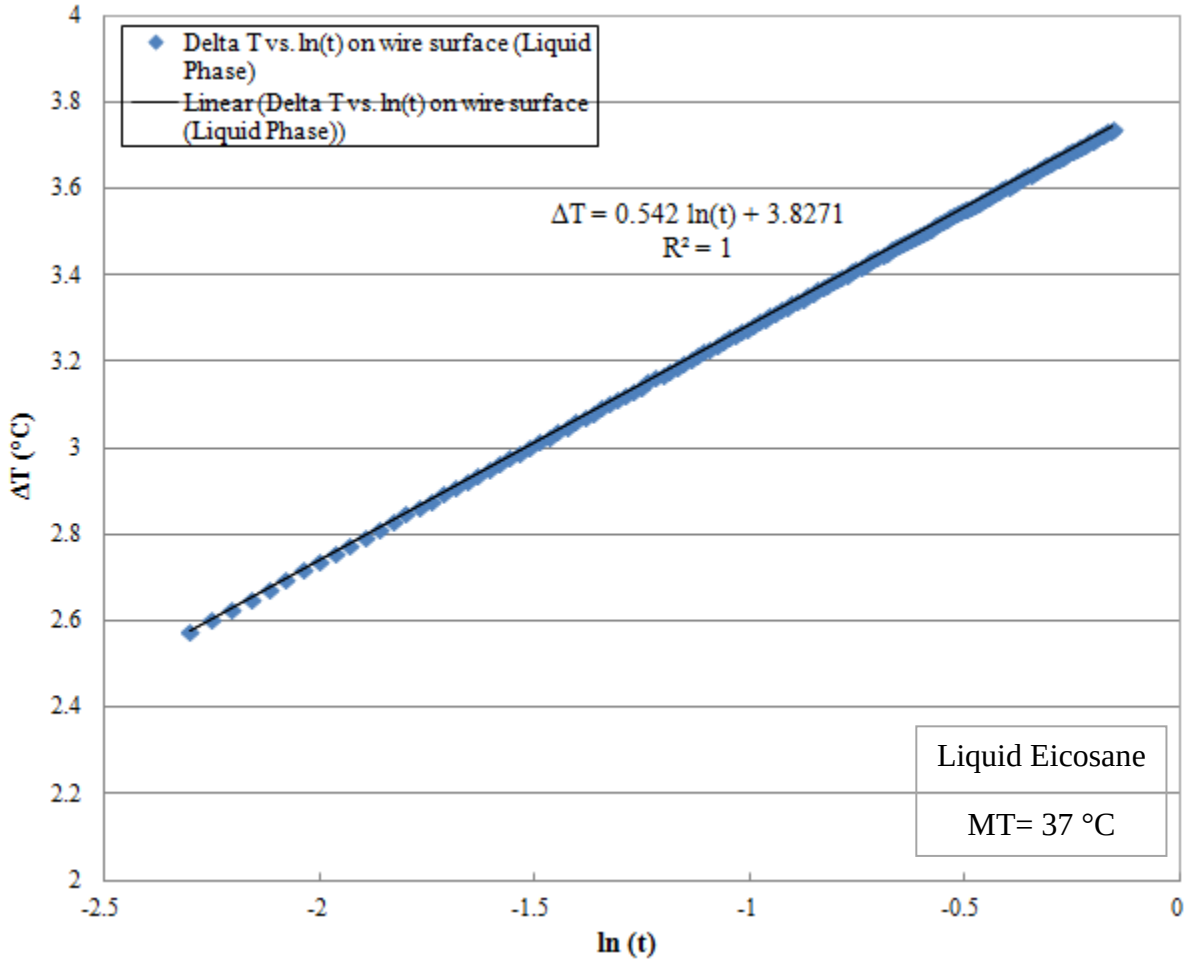

Figure 4.14 Plot of the liquid phase eicosane temperature rise on the surface of the wire versus natural logarithm of time with an initial temperature of T_i=313 K using the FLUENT model

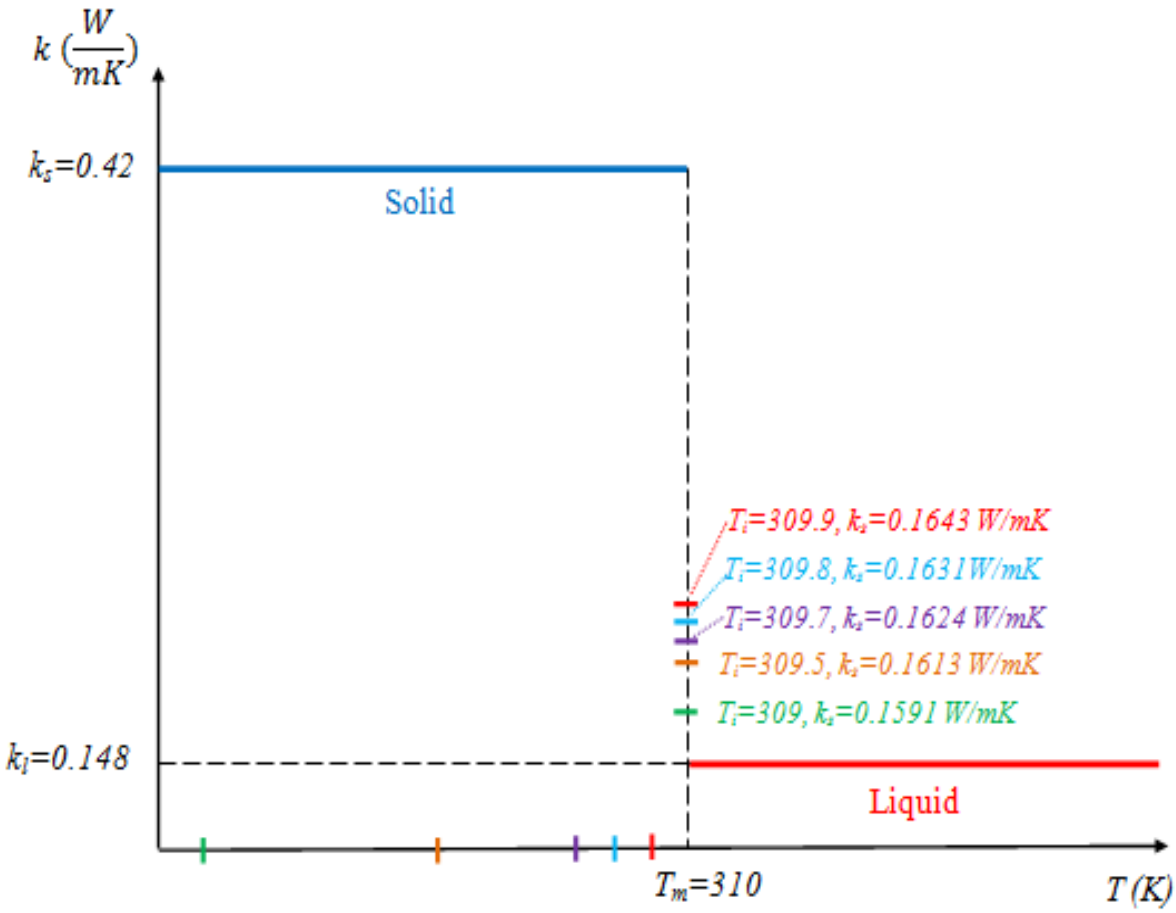

Figure 4.15 Predicted "effective" thermal conductivity values of eicosane as a function of the initial solid state temperature using the FLUENT model

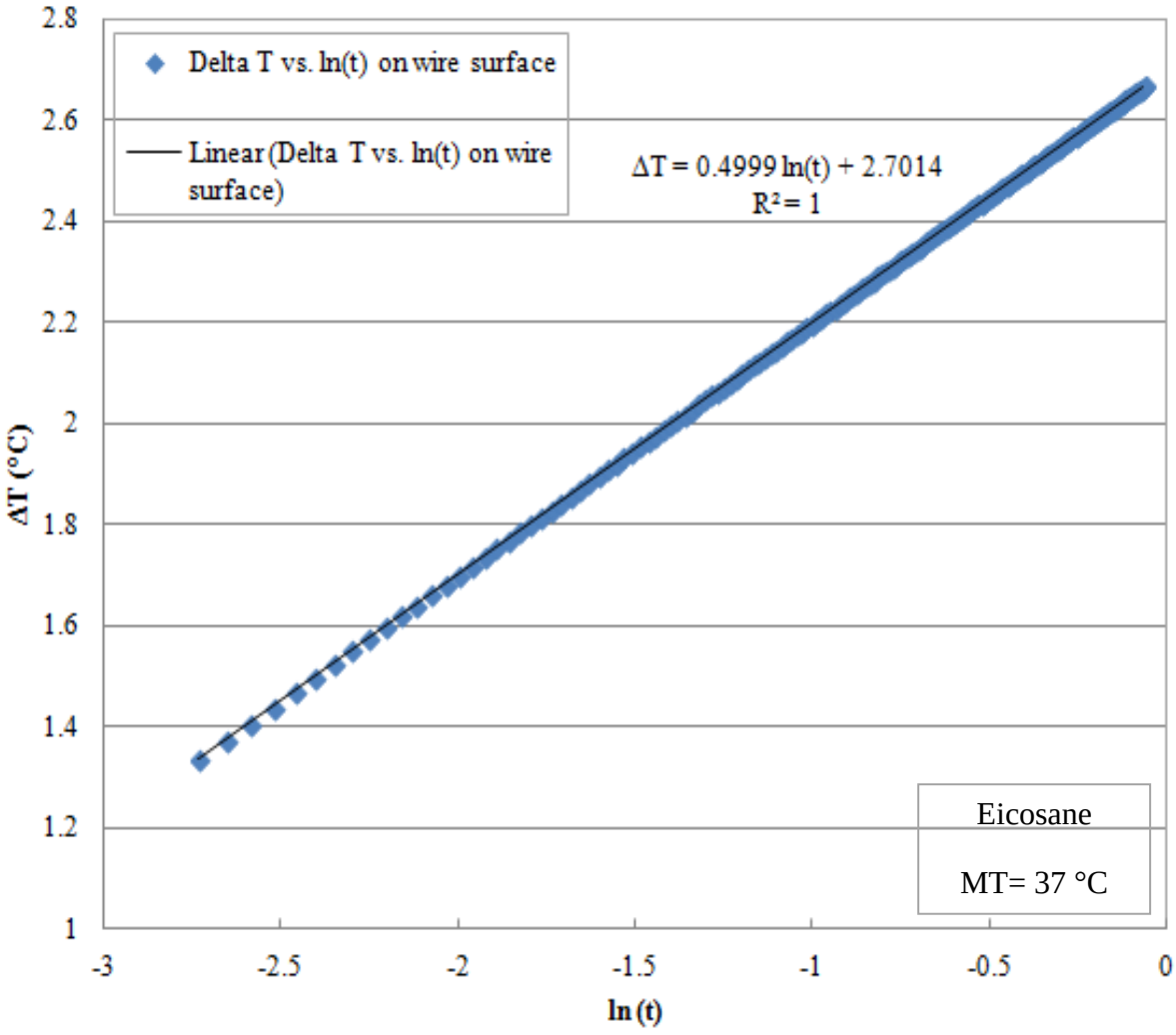

Figure 4.16 Plot of the solid phase eicosane temperature rise on the surface of the wire versus natural logarithm of time with an initial temperature of T_i=309 K using the FLUENT model

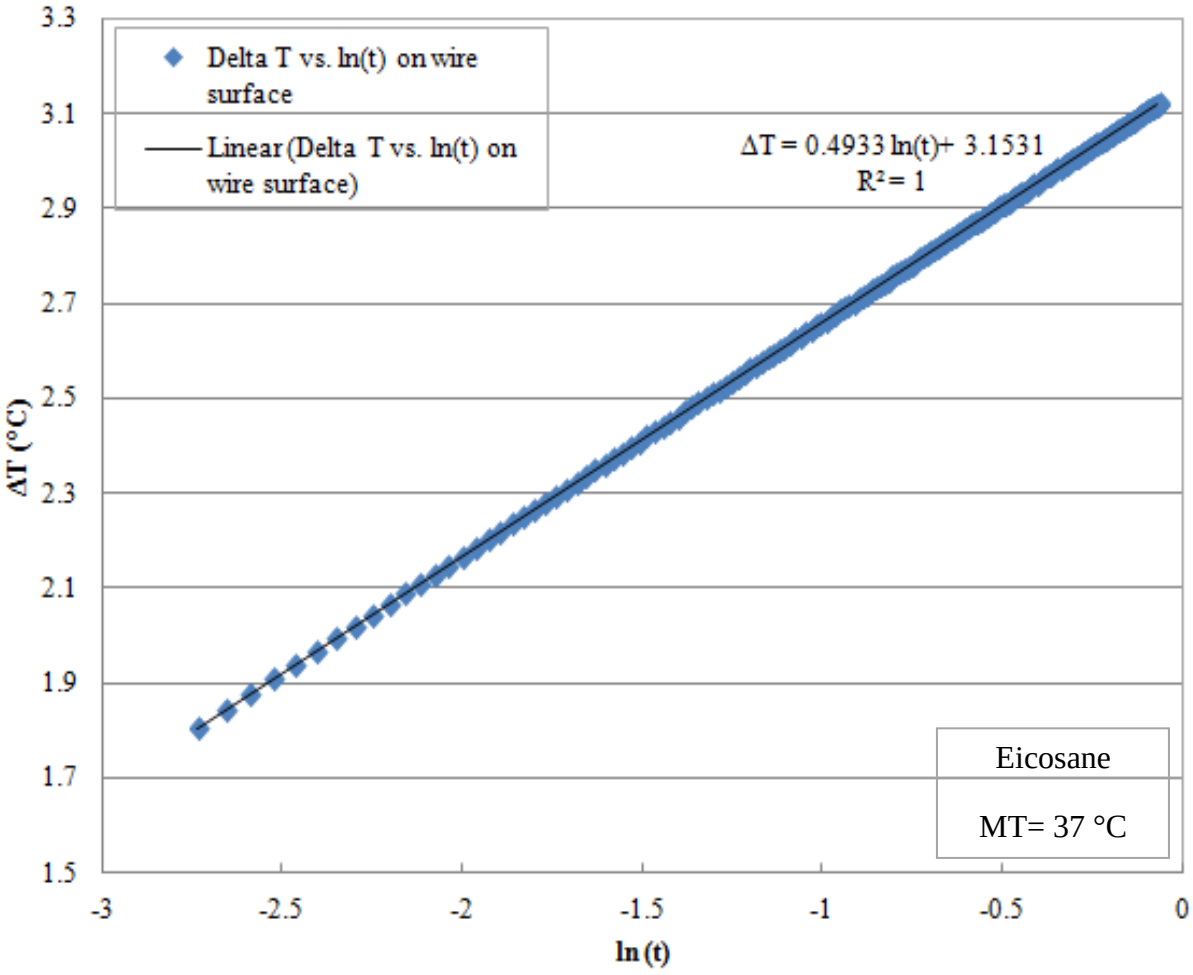

Figure 4.17 Plot of the solid phase eicosane temperature rise on the surface of the wire versus natural logarithm of time with an initial temperature of T_i=309.5 K using the FLUENT model

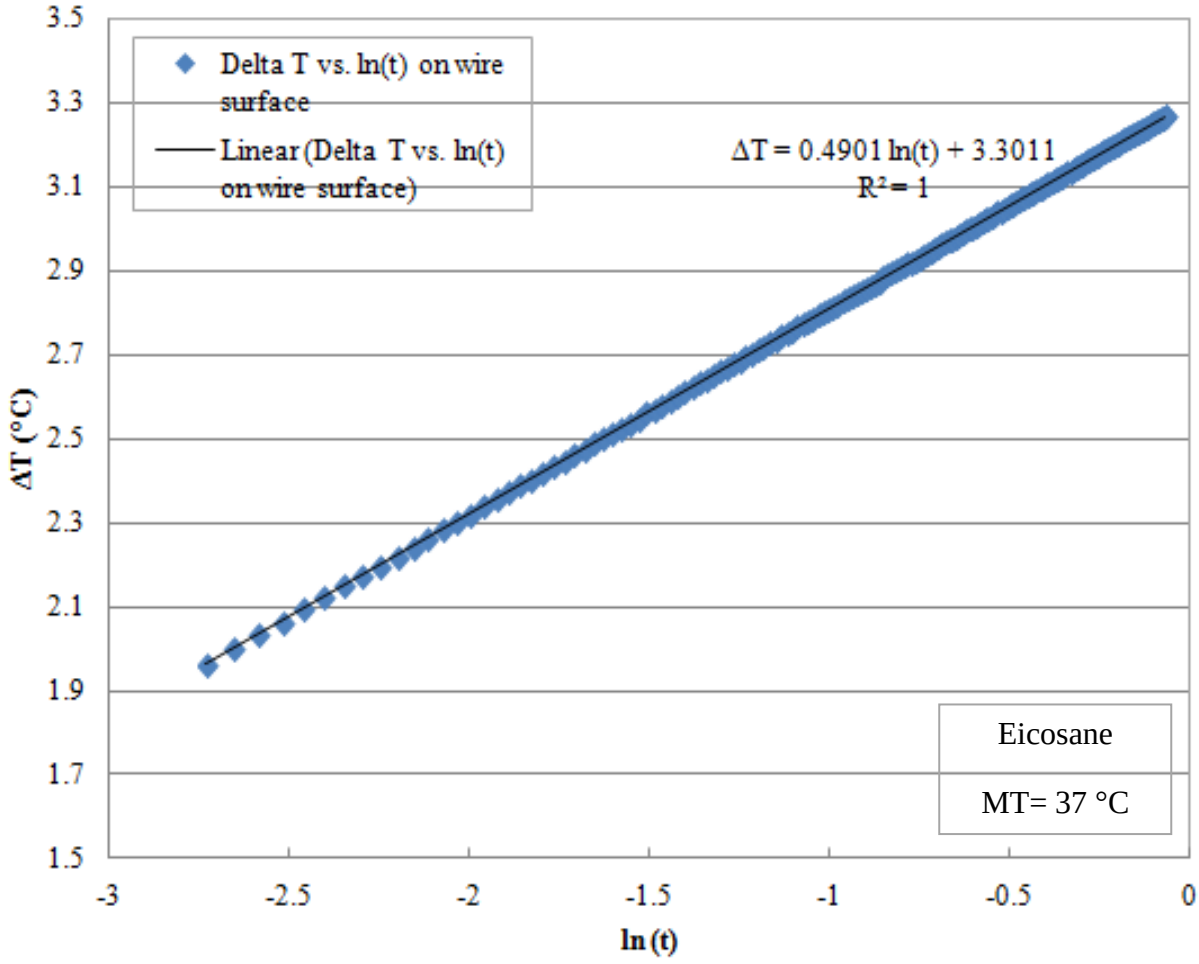

Figure 4.18 Plot of the solid phase eicosane temperature rise on the surface of the wire versus natural logarithm of time with an initial temperature of T_i=309.7 K using the FLUENT model

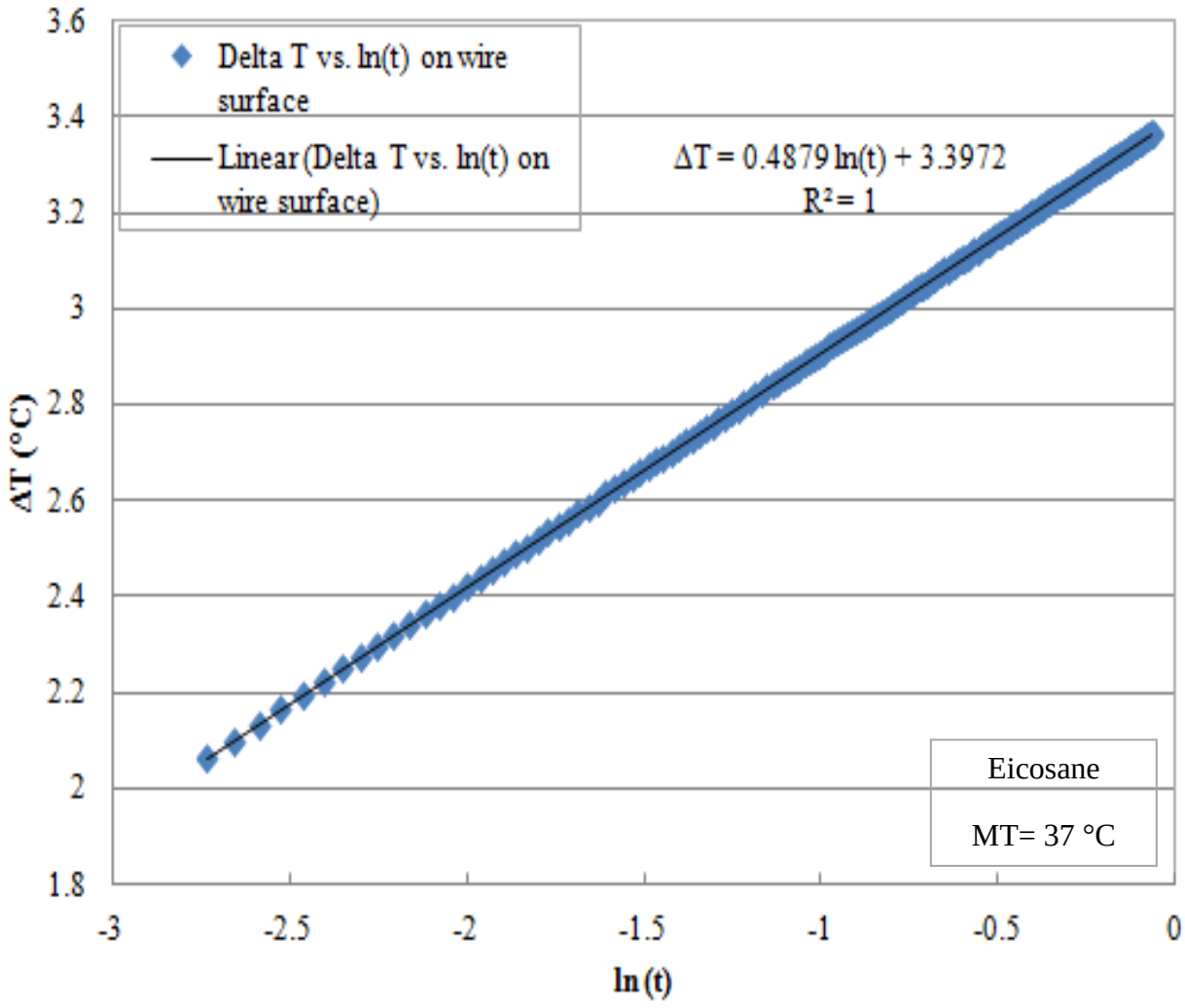

Figure 4.19 Plot of the solid phase eicosane temperature rise on the surface of the wire versus natural logarithm of time with an initial temperature of T_i=309.8 K using the FLUENT model

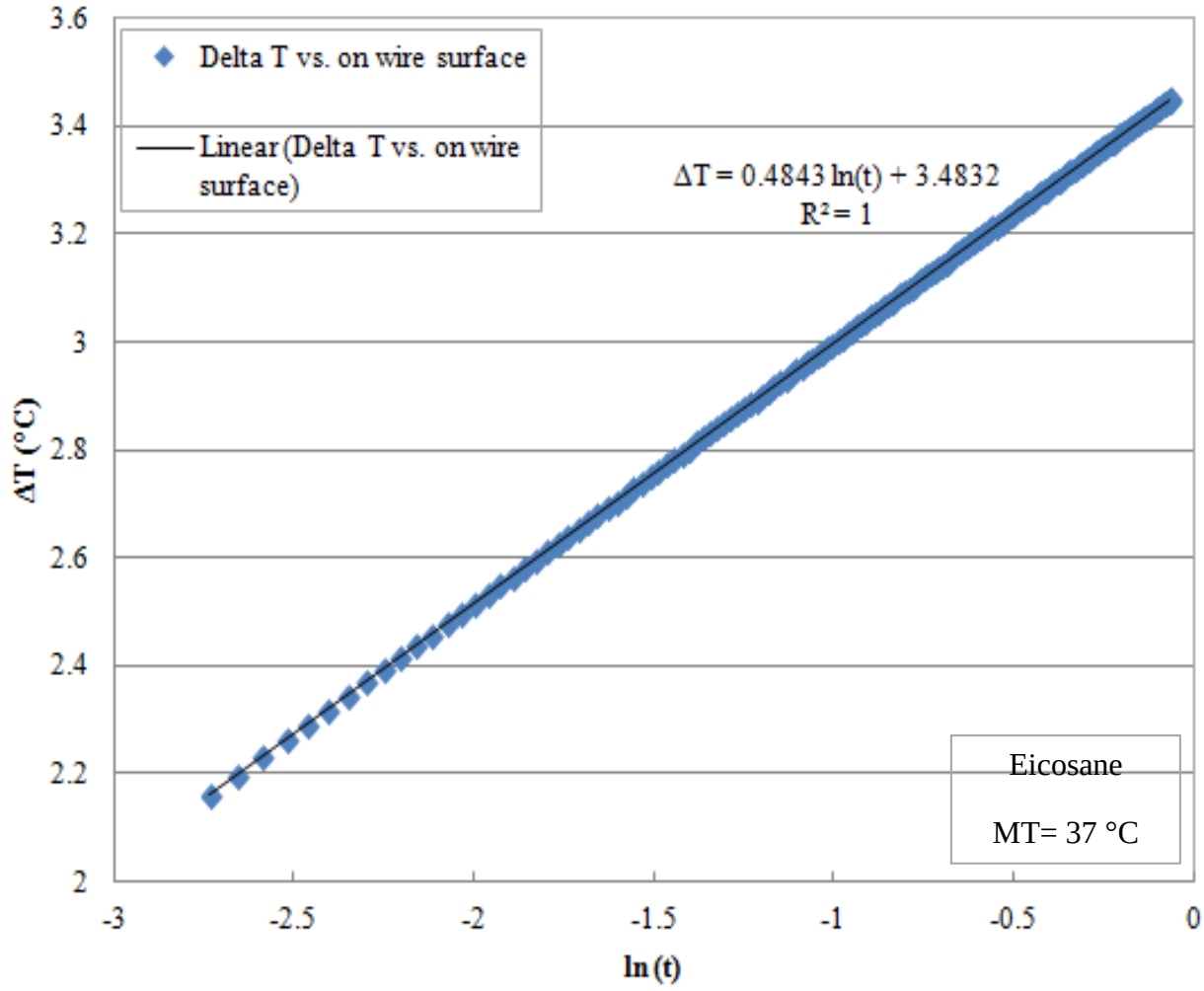

Figure 4.20 Plot of the solid phase eicosane temperature rise on the surface of the wire versus natural logarithm of time with an initial temperature of T_i=309.9 K using the FLUENT model

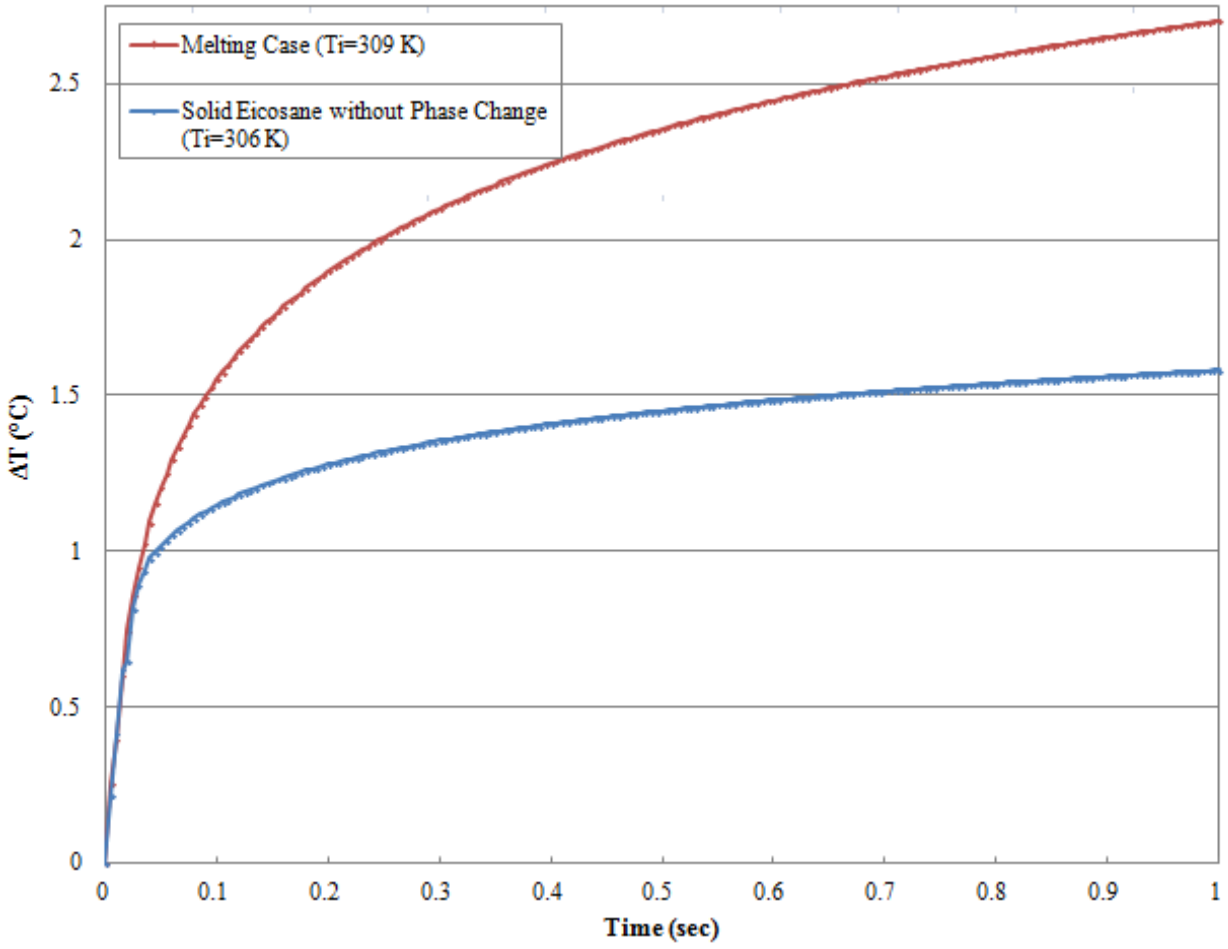

Figure 4.21 Plots of temperature rise on the surface of the wire for two cases with and without phase change with the initial temperatures of T_i=309 K and T_i=306 K, respectively

Chapter 5 Conclusions

In this chapter, conclusions and remarks about the experimental and numerical work which were discussed in the previous chapters are presented in an itemized manner as follows:

1) Eicosane-based NePCM colloids were prepared using copper (II) oxide (CuO) nanoparticles stabilized by sodium oleate acid ($C_{18}H_{33}O_2Na$) for eight different mass fractions of nanoparticles (0, 1, 2, 3.5, 5, 6.5, 8 and 10 wt%). No significant precipitation was visually observed, even for the most concentrated 10 wt% sample. Furthermore, desirable long-term stability of NePCM samples was successfully achieved.

2) Thermal conductivity measurements of the CuO-eicosane solid composites were found to be independent of the measurement temperature for a given particle loading regardless of the three solidification procedures (standard atmosphere, ice-bath and oven solidification) that were investigated.

3) Irrespective of the preparation/solidification scheme, as the melting temperature was approached, thermal conductivity of the composites rose sharply for all sets of solid disks.

4) The ice-water bath solidification route eicosane-CuO samples consistently exhibited lowest values of thermal conductivity, whereas the samples of oven solidification scheme

corresponded to the highest values. This behavior might be due to the greater void population of ice-water bath samples and/or crystal structure deviations due to processing routes.

5) Considering eicosane-CuO composites, for mass fractions greater than 2 wt%, a non-monotonic relation between the thermal conductivity and the mass fraction, independent of the temperature range studied, was exhibited.

6) Although no functionalization was performed on the MWCNT powders, the amount of thermal conductivity enhancement for 0.27 wt% eicosane-MWCNTs solid samples (~25-35%) was much higher than that of 1 wt% eicosane-CuO solid disks (~1-3%).

7) A 1-D transient conduction problem was successfully formulated and solved over a finite cylindrical domain with and without phase transition to model the behavior of a THW apparatus near the melting temperature of the medium. Numerical thermal conductivity predictions were obtained by employing an enthalpy method with the aid of ANSYS® FLUENT software.

8) An exact mathematical analysis for a similar melting problem was also adopted to verify the predictions of the FLUENT model under phase transition condition. The plots of temperature rise on the wire surface were nearly following the same trend with an error of less than 0.5%.

9) Using the FLUENT model, thermal conductivity predictions in both liquid and solid phases were performed in the absence of phase change phenomenon. The difference between the extracted thermal conductivity values and the initially-assigned values based on the literature was less than 1% and 0.81% for the solid and liquid phases, respectively.

10) The effect of the initial solid state temperature on the predicted thermal conductivity values under the presence of melting was also explored. Five different cases were considered to study if any sharp rise in thermal conductivity values will occur near the melting point of the PCM. It was shown that there is no abrupt behavior as temperature approaches the melting point of eicosane and all the predicted thermal conductivity values are between the assigned values of the liquid and solid states.

Bibliography

Abramowitz, M., and Stegun, I. A., 1964, *Handbook of Mathematical Functions*, National Bureau of Standards (NBS) Applied Mathematic Series, 55, U.S. Government Printing Office, Washington, D.C., USA, pp. 228-229.

Ai, D., Su, L., Gao, Z., Deng, C., and Dai, X., 2010, "Study of ZrO_2 Nanopowders Based Stearic Acid Phase Change Materials," *Particuology*, 8, pp. 394-397.

Assael, M. J., Antoniadis, K. D., and Wakeham, W. A., 2010, "Historical Evolution of the Transient Hot-Wire Technique," *International Journal of Thermophysics*, 31, pp. 1051-1072.

Assael, M. J., Karagiannidis, L., and Malamataris, N., and Wakeham, W. A., 1998, "The Transient Hot-Wire Technique: A Numerical Approach," *International Journal of Thermophysics*, 19, pp. 379-389.

Bayramoglu, E.C., 2011, "Thermal Properties and Stability of n-Octadecane Based Composites Containing Multiwalled Carbon Nanotubes," *Polymer Composites*, 32, pp. 904-909.

Carslaw, H. S., and Jaeger, J. C., 1959, *Conduction of Heat in Solids*, 2nd edition, Oxford University Press, London, UK.

Clary, D. R. and Mills, G., 2011, "Preparation and Thermal Properties of CuO Particles," *The Journal of Physical Chemistry C*, 115, pp. 1767-1775.

Das, S. K., Choi, S. U. S., Yu, W. and Pradeep, R., 2008, *Nanofluids: Science and Technology*, John Wiley & Sons, Inc., Hoboken, New Jersey.

de Groot, J. J., Kestin, J., and Sookiazian, H., 1974, "Instrument to Measure the Thermal Conductivity of Gases," *Physica*, 75, pp. 454-482.

Duluc, M-C, Xin, S., and Le Quere, P., 2003, "Transient Natural Convection and Conjugate Transients around a Line Heat Source," *International Journal of Heat and Mass Transfer*, 46, pp. 341-354.

Fan, Liwu, 2011, Enhanced Thermal Conductivity and Expedited Freezing of Nanoparticle Suspensions Utilized as Novel Phase Change Materials, PhD Thesis, Mechanical Engineering Department, Auburn University, Alabama, USA, http://etd.auburn.edu/etd/bitstream/handle/10415/2707/Dissertation_Fan_0717.pdf?sequence=2.

Gao, J. W., Zheng, R. T., Ohtani, H., Zhu, D. S., and Chen, G., 2009, "Experimental Investigation of Heat Conduction Mechanisms in Nanofluids. Clue on Clustering," *Nano Letters*, 9, pp. 4128-4132.

Goldsmith, A., Waterman, T. E., and Hirschhorn, H. J., 1961, *Handbook of Thermophysical properties of Solid Materials, volume 1: Elements*, The MacMillan Company, New York, NY, USA.

Grigoriev, I. S., and Meilikhov, E. Z., 1997, *Handbook of Physical Quantities*, CRC-Press LLC, Boca Raton, FL, USA.

Gustafsson, S. E., 1991, "Transient Plane Source Technique for Thermal Conductivity and Thermal Diffusivity Measurements of Solid Materials," *Review of Scientific Instruments,* 62, pp. 797-804.

Hale, D. V., Hoover, M. J., and O'Neill, M. J., 1971, *Phase Change Materials Handbook,* National Aeronautics and Space Administration (NASA), Huntsville, AL, USA.

Harikrishnan, S., and Kalaiselvam, S., 2012, "Preparation and Thermal Characteristics of Cuo-Oleic Acid Nanofluids as a Phase Change Material," *Thermochimica Acta,* 533, pp. 46-55.

He, Q., Zeng, S., Yin, S., and Wang, S., 2012, "Experimental Investigation on Nucleation Supercooling Degree of TiO_2-H_2O Nanofluids for Cool Storage," *Advanced Materials Research,* 550-553, pp. 2723-2727.

Healy, J. J., de Groot, J. J., and Kestin, J., 1976, "The Theory of the Transient Hot-Wire Method for Measuring Thermal Conductivity," *Physica,* 82C, pp. 392-408.

Ho, C. J. and Gao, J. Y., 2009, "Preparation and Thermophysical Properties of Nanoparticle-in-Paraffin Emulsion as Phase Change Material," *International Communications in Heat and Mass Transfer,* 36, pp. 467-470.

Hu, P., Lu, D-J, Fan, X-Y, Zhou, X., and Chen, Z-S, 2011, "Phase Change Performance of Sodium Acetate Trihydrate with AIN Nanoparticles and CMC," *Solar Energy Materials & Solar Cells,* 95, pp. 2645-2649.

Humphries, W. R., and Griggs, E. I., 1977, *A Design Handbook for Phase Change Thermal Control and Energy Storage Devices,* National Aeronautics and Space Administration (NASA), Huntsville, AL, USA.

Jang, S. P. and Choi, S. U. S., 2007, "Effects of Various Parameters on Nanofluid Thermal Conductivity," *Journal of Heat Transfer,* 129, pp. 617-623.

Jesumathy, S., Udayakumar, M., and Suresh, S., 2012, "Experimental Study of Enhanced Heat Transfer by Addition of Cuo Nanoparticle," *Heat and Mass Transfer,* 48, pp. 965-978.

Kalaiselvam, S., Parameshwaran, R., and Harikrishnan, S., 2012, "Analytical and Experimental Investigations of Nanoparticles Embedded Phase Change Materials for Cooling Application in Modern Buildings," *Renewable Energy*, 39, pp. 375-387.

Khodadadi, J. M., Fan, Liwu, and Babaei, H., 2013, "Thermal Conductivity Enhancement of Nanostructure-Based Colloidal Suspensions Utilized as Phase Change Materials for Thermal Energy Storage: A Review," *Renewable and Sustainable Energy Reviews*, 24, pp. 418-444.

Khodadadi, J. M. and Hosseinizadeh, S. F., 2007, "Nanoparticle-Enhanced Phase Change Materials (NEPCM) with Great Potential for Improved Thermal Energy Storage," *International Communications in Heat and Mass Transfer,* 34, pp. 534-543.

Kumaresan, V., Velraj, R., and Das, S. K., 2012, "The Effect of Carbon Nanotubes in Enhancing the Thermal Transport Properties of PCM during Solidification," *Heat and Mass Transfer,* 48, pp. 1345-1355.

Mare, T., Sow, O., Halelfadl, S., Lebourlout, S., and Nguyen, C. T., 2012, "Experimental Study of the Freezing Point of γ-Al_2O_3/Water Nanofluid," *Advances in Mechanical Engineering*, 2012, 7 pages.

Maxwell, J. C., 1873, *A Treatise on Electricity and Magnetism,* Clarendon Press, Oxford, UK.

Nagasaka, Y., and Nagashima, A., 1981, "Absolute Measurement of the Thermal Conductivity of Electrically Conducting Liquids by the Transient Hot-Wire Method," *Journal of Physics E: Scientific Instruments*, 14, pp. 1435-1440.

Özişik, M. N., 1993, *Heat Conduction*, John Wiley & Sons Inc., New York, NY, USA.

Paterson, S., 1952, "Propagation of a Boundary of Fusion," *Proceedings of the Glasgow Mathematical Association*, 1, pp. 42-47.

Rathod, M. K., and Banerjee, J., 2013, "Thermal Stability of Phase Change Materials used in Latent Heat Energy Storage Systems: A Review," *Renewable and Sustainable Energy Reviews*, 18, pp. 246-258.

Roder, H. M., 1981, "A Transient Hot Wire Thermal Conductivity Apparatus for Fluids," *Journal of Research of the National Bureau of Standards*, 86, pp. 457-493.

Rusconi, R., Isa, L., and Piazza, R., 2004, "Thermal-lensing Measurement of Particle Thermophoresis in Aqueous Dispersions," *Journal of the Optical Society of America B*, 21(3), pp. 605-616.

Rusconi, R., Williams, W. C., Buongiorno, J., Piazza, R., and Hu, L-W, 2007, "Numerical Analysis of Convective Instabilities in A Transient Short-Hot-Wire Setup for Measurement of Liquid Thermal Conductivity," *International Journal of Thermophysics*, 28(4), DOI: 10.1007/s10765-007-0202-2, pp. 1131-1146.

Sanusi, O., Warzoha, R., and Fleischer, A. S., 2011, "Energy Storage and Solidification of Paraffin Phase Change Material Embedded with Graphite Nanofibers," *International Journal of Heat and Mass Transfer*, 54, pp. 4429-4436.

Shaikh, S., and Lafdi, K., 2010, "C/C Composite, Carbon Nanotube and Paraffin Wax Hybrid Systems for the Thermal Control of Pulsed Power in Electronics," *Carbon*, 48, pp. 813-824.

Shamsunder, N., and Sparrow, E. M., 1975, "Analysis of Multidimensional Conduction Phase Change via the Enthalpy Model," *Journal of Heat Transfer*, 97C, pp. 333-340.

Sharma, A., Tyagi, V. V., Chen, C. R. and Buddhi, D., 2009, "Review on Thermal Energy Storage with Phase Change Materials and Applications," *Renewable and Sustainable Energy Reviews*, 13, pp. 318-345.

Shi, J-N, Ger, M-D, Liu, Y-M, Fan, Y-C, Wen, N-T, Lin, C-K, and Pu, N-W, 2013, "Improving the Thermal Conductivity and Shape-Stabilization of Phase Change Materials using Nanographite Additives," *Carbon*, 51, pp. 365-372.

Stryker, P. C., and Sparrow, E. M., 1990, "Application of a Spherical Thermal Conductivity Cell to Solid n-Eicosane Paraffin," *International Journal of Heat and Mass Transfer*, 33, pp. 1781-1793.

Teng, T-P, Cheng, C-M, and Cheng, C-P, 2013, "Performance Assessment of Heat Storage by Phase Change Materials Containing MWCNTs and Graphite," *Applied Thermal Engineering*, 50, pp. 637-644.

Teng, T-P, Lin, B-G, and Yeh, Y-Y, 2011, "Characterization of Heat Storage by Nanocomposite-Enhanced Phase Change Materials," *Advanced Materials Research*, 287-290, pp. 1448-1455.

Wakeham, W. A., and Assael, M. J., 1999, "Thermal Conductivity Measurement" in *Mechanical Variables Measurement - Solid, Fluid, and Thermal*, edited by Webster, J. G., CRC Press.

Wang, J., Xie, H., Li, Y., and Xin, Z., 2010a, "PW Based Phase Change Nanocomposites Containing $\gamma - Al_2O_3$," *Journal of Thermal Analysis and Calorimetry*, 102(2), pp. 709-713.

Wang, J., Xie, H., and Xin, Z., 2008, "Thermal Properties of Heat Storage Composites Containing Multiwalled Carbon Nanotubes," *Journal of Applied Physics*, 104, 113537, 5 pages.

Wang, J., Xie, H., and Xin, Z., 2009, "Thermal Properties of Paraffin Based Composites Containing Multi-Walled Carbon Nanotubes," *Thermochimica Acta*, 488, pp. 39-42.

Wang, J., Xie, H., and Xin, Z., 2011, "Preparation and Thermal Properties of Grafted CNTs Composites," *Journal of Materials Science & Technology*, 27, pp. 233-238.

Wang, J., Xie, H., Xin, Z., and Li, Y., 2010c, "Increasing the Thermal Conductivity of Palmitic Acid by the Addition of Carbon Nanotubes," *Carbon*, 48, pp. 3979-3986.

Wang, J., Xie, H., Xin, Z., Li, Y., and Chen, L., 2010b, "Enhancing Thermal Conductivity of Palmitic Acid Based Phase Change Materials with Carbon Nanotubes as Fillers," *Solar Energy*, 84, pp. 339-344.

Wu, S., Zhu, D., Zhang, X. and Huang, J., 2010, "Preparation and Melting/Freezing Characteristics of Cu/Paraffin Nanofluid as Phase-Change Material (PCM)," *Energy and Fuels*, 24, pp. 1894-1898.

Wu, S. Y., Wang, H., Xiao, S., and Zhu, D. S., 2011, "An Investigation of Melting/Freezing Characteristics of Nanoparticle-Enhanced Phase Change Materials," *Journal of Thermal Analysis and Calorimetry*, 102, pp. 709-713.

Yarbrough, D. W., and Kuan, C-N, 1981, "The Thermal Conductivity of Solid N-Eicosane, N-Octadecane, N-Heptadecane, N-Pentadecane, and N-Tetradecane" *Proceedings of the 17th International Thermal Conductivity Conference (ITCC)*, Plenum Press, New York, Ed. J.G. Hust (1983), pp. 265-274.

Yaws, C. L., 1994, *Handbook of Viscosity, Volume 3: Organic Compounds C_8 to C_{28}*, Gulf Professional Publishing, Houston, TX, USA.

Yaws, C. L., 1995, *Handbook of Thermal Conductivity, Volume 3: Organic Compounds C_8 to C_{28}*, Gulf Professional Publishing, Houston, TX, USA.

Yu, W., France, D. M., Routbort, J. L. and Choi, S. U. S., 2009, "Review and Comparison of Nanofluid Thermal Conductivity and Heat Transfer Enhancements," *Heat Transfer Engineering*, 29, pp. 432-460.

Yu, Z-T, Fang, X., Fan, L-W, Wang, X., Xiao, Y-Q, Zeng, Y., Xu, X., Hu, Y-C, and Cen, K-F, 2013, "Increased Thermal Conductivity of Liquid Paraffin-Based Suspensions in the presence of Carbon Nano-additives of various Sizes and Shapes," *Carbon*, 53, pp. 277-285.

Zalba, B., Marin, J. M., Cabeza, L. F., and Mehling, H., 2003, "Review on Thermal Energy Storage with Phase Change: Materials, Heat Transfer Analysis and Applications," *Applied Thermal Engineering*, 23, pp. 251-283.

Zeng, J. L., Sun, L. X., Xu, F., Tan, Z. C., Zhang, Z. H., Zhang, J. and Zhang, T., 2007, "Study of a PCM Based Energy Storage System Containing Ag Nanoparticles," *Journal of Thermal Analysis and Calorimetry*, 87, pp. 369-373.

Zeng, J-L, Zhu, F-R, Yu, S-B, Zhu, L., Cao, Z., Sun, L-X, Deng, G-R, Yan, W-P, and Zhang, L., 2012, "Effect of Copper Nanowires on the Properties of an Organic Phase Change Material," *Solar Energy Materials & Solar Cells*, 105, pp. 174-178.

Zheng, R. T., Gao, J. W., Wang, J. J., and Chen, G., 2011, "Reversible Temperature Regulation of Electrical and Thermal Conductivity using Liquid-Solid Transitions," *Nature Communications*, 2, pp. 28901-28906.

Appendix A Interface Conditions for Phase Change Problems

In this appendix, the pertinent continuity and thermal energy balance equations at the moving interface separating the solid and liquid phases during the 1-D transient solidification/melting of a pure material are derived. It is assumed that the values of the density for the liquid and solid phases are different. In turn, the difference between these two quantities will promote motion in the liquid phase.

A.1. Solidification

The model problem and the adopted coordinate system for 1-D solidification of a semi-infinite medium are shown in Figure A.1 (Özişik, 1993). The medium being a pure material that is initially at temperature T_i extends from x=0 to x=∞. For t>0, the medium is cooled at x=0 and a vertical interface that is at the freezing temperature (T_m) sweeps into the liquid zone with velocity V_x. In effect, a solid layer is formed between x=0 and the instantaneous position of the interface, s(t). Note that V_x is equal to ds/dt. Assuming the density of the solid phase to be greater than the liquid density (true for materials except water, bismuth and antimony), liquid motion toward the interface is expected as indicated by vector V_l in Figure A.1. Due to the moving nature of the interface as viewed by an observer standing at x=const. (Figure A.2.a), the

problem is formulated as a steady one by considering it as viewed by an observer that is fixed to the interface (Figure A.2.b). Now consider an extremely thin control volume with its two faces positioned on the two sides of interface. With ρ and V standing for density and velocity, and subscripts s and l refering to the solid and liquid phases, respectively, the steady form of the continuity relation at the interface implies:

$$-\dot{m}_{in} + \dot{m}_{out} = 0, \tag{A.1}$$

$$-\rho_l (V_x - V_l) + \rho_s V_x = 0 , \tag{A.2}$$

$$V_x(\rho_l - \rho_s) = \rho_l V_l , \tag{A.3}$$

The derived relation (A.3) matches equation (11-7a) of Özişik (1993). Note that under these conditions, the two velocities in relation (A.3) have opposite signs. If the densities of the two phases are the same, melt flow will not occur.

The steady thermal energy balance equation at the interface for the same control volume is:

$$q_s - q_l = -\rho_l(V_x - V_l)H_l + \rho_s V_x H_s, \tag{A.4}$$

$$q_s - q_l = -(\rho_l H_l - \rho_s H_s)V_x + \rho_l H_l V_l, \tag{A.5}$$

where H stands for enthalpy per unit mass and the conductive heat fluxes on the two sides of the control volume are:

$$q_l = -k_l \frac{dT_l}{dx} , \qquad \text{and} \qquad q_s = -k_s \frac{dT_s}{dx} . \tag{A.6}$$

Substitution of relation (A.6) into equation (A.5) gives:

$$-k_s \frac{dT_s}{dx} + k_l \frac{dT_l}{dx} = -(\rho_l H_l - \rho_s H_s)V_x + \rho_l H_l V_l. \tag{A.7}$$

Upon elimination of V_l from relation (A.7) by using equation (A.3), the energy equation takes the form:

$$k_s \frac{dT_s}{dx} - k_l \frac{dT_l}{dx} = \rho_s L V_x \,, \tag{A.8}$$

in which $L = H_l - H_s$, represents the latent heat of fusion. Again, relation (A.8) matches equation (11-8a) of Özişik (1993) and equation (6.4) of Jiji (2009) which verifies the derivation above.

A.2. Melting

The model problem and the adopted coordinate system for 1-D melting of a semi-infinite medium are shown in Figure A.3 (Özişik, 1993). The medium being a pure material that is initially at temperature T_i extends from x=0 to x=∞. For t>0, the medium is heated at x=0 and a vertical interface that is at the melting temperature (T_m) sweeps into the solid zone with velocity V_x. In effect, a liquid layer is formed between x=0 and the instantaneous position of the interface, s(t). Note that V_x is equal to ds/dt. Assuming the density of the solid phase to be greater than the liquid density (true for materials except water, bismuth and antimony), liquid motion away from the interface is expected as indicated by vector V_l in Figure A.3. Due to the moving nature of the interface as viewed by an observer standing at x=const. (Figure A.4.a), the problem is formulated as a steady one by considering it as viewed by an observer that is fixed to the interface (Figure A.4.b). Now consider an extremely thin control volume with its two faces positioned on the two sides of interface. With ρ and V standing for density and velocity, and

subscripts s and l refering to the solid and liquid phases, respectively, the steady form of the continuity relation at the interface implies:

$$-\dot{m}_{in} + \dot{m}_{out} = 0, \tag{A.9}$$

$$-\rho_s V_x + \rho_l (V_x - V_l) = 0, \tag{A.10}$$

$$\rho_l (V_x - V_l) = \rho_s V_x \,, \tag{A.11}$$

Note that under these conditions, the two velocities in relation (A.11) have opposite signs. If the densities of the two phases are the same, melt flow will not occur.

The steady thermal energy balance equation at the interface for the same control volume is:

$$q_l - q_s = -\rho_s H_s V_x + \rho_l H_l (V_x - V_l) \,, \tag{A.12}$$

where H stands for enthalpy per unit mass and the conductive heat fluxes on the two sides of the control volume are:

$$q_l = -k_l \frac{dT_l}{dx} \,, \qquad \text{and} \qquad q_s = -k_s \frac{dT_s}{dx} \,. \tag{A.13}$$

Substitution of relation (A.13) into equation (A.12) gives:

$$k_s \frac{dT_s}{dx} - k_l \frac{dT_l}{dx} = -\rho_s H_s V_x + \rho_l H_l (V_x - V_l) \,, \tag{A.14}$$

Upon elimination of $(V_x - V_l)$ from relation (A.14) by using equation (A.11), the energy equation takes the form:

$$k_s \frac{dT_s}{dx} - k_l \frac{dT_l}{dx} = \rho_s L V_x \,. \tag{A.15}$$

in which $L = H_l - H_s$, represents the latent heat of fusion. Relation (A.15) matches equation (2c) of Yao and Prusa (1989) which verifies the derivation above. Also note that relations (A.8) and (A.15) that correspond to the model freezing and melting problems, respectively, are identical.

Finally, if the pure material under consideration was denser in its liquid phase (water, bismuth and antimony), similar derivations need to be performed.

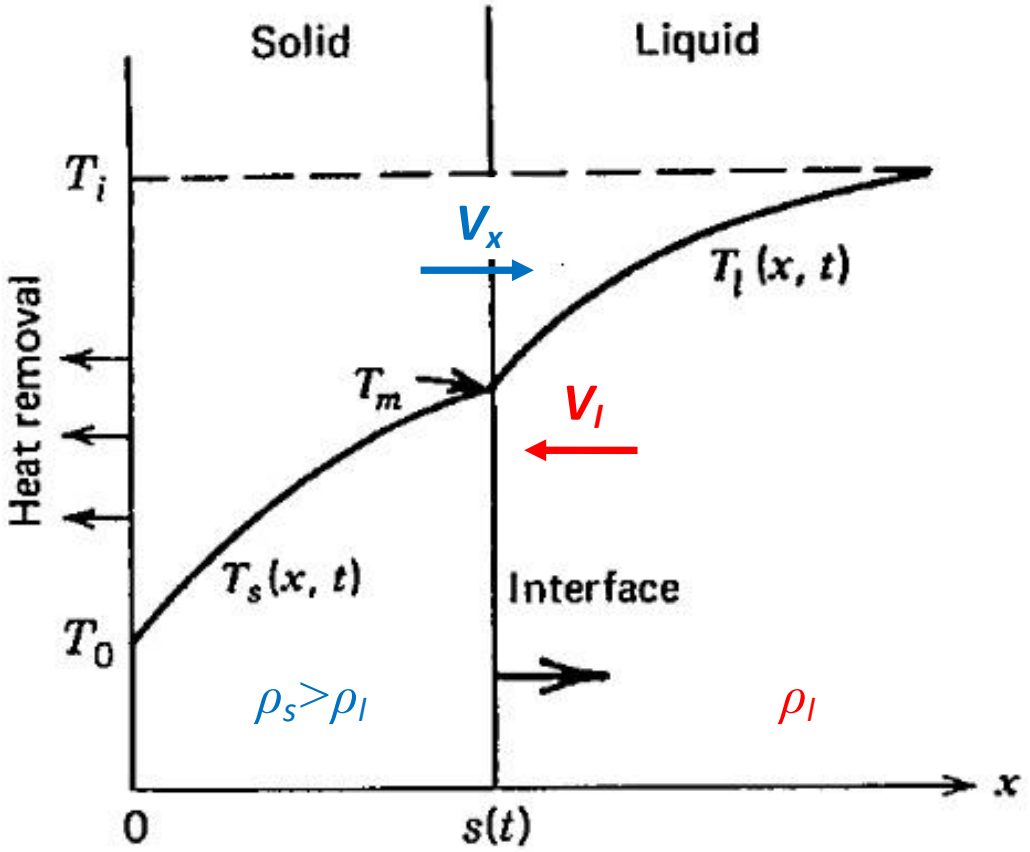

Figure A.1 Schematic diagram of the geometry for 1-D solidification problem (Özişik, 1993)

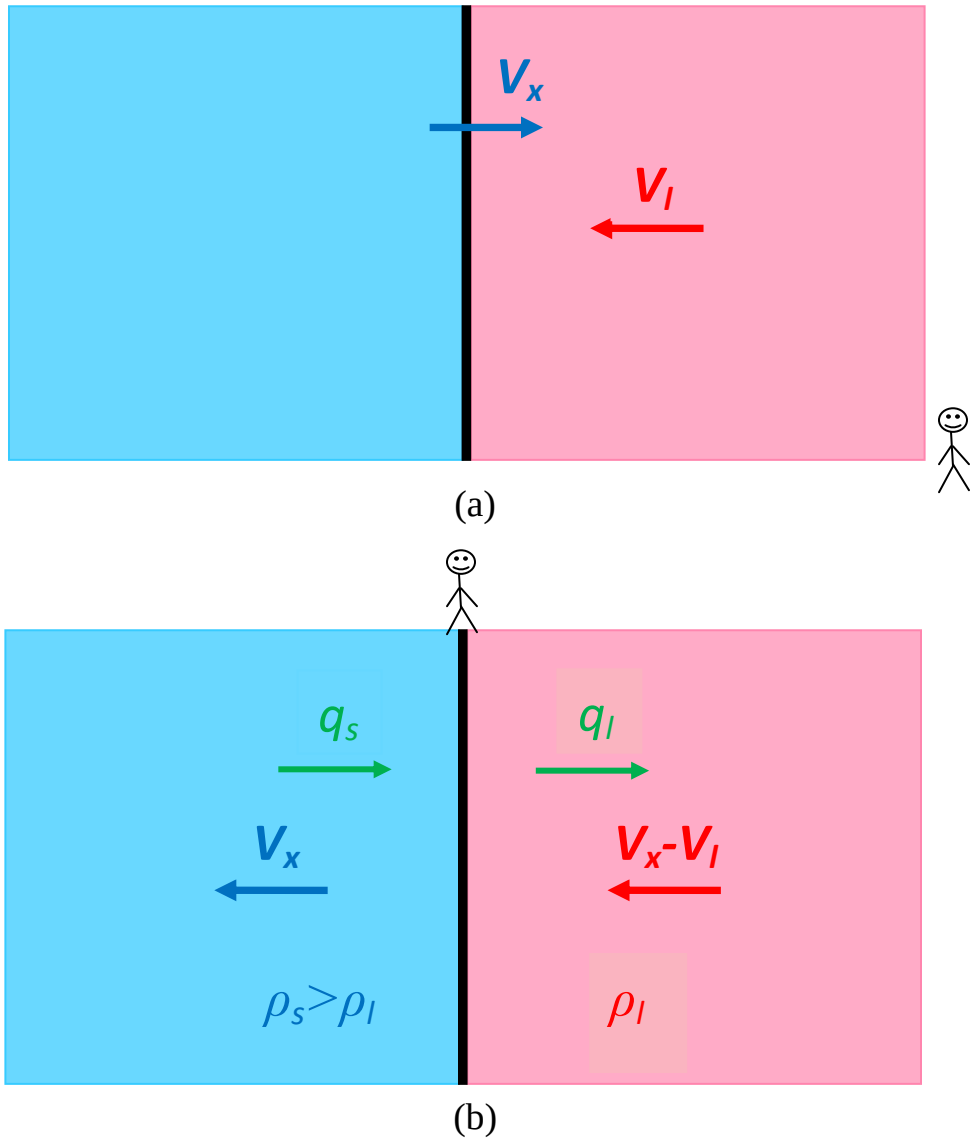

Figure A.2 (a) Solidification as viewed by an observer positioned at x=const. showing the interface moving to the right into the liquid phase and (b) the steady-state version of the problem viewed by an observer that is riding with the interface

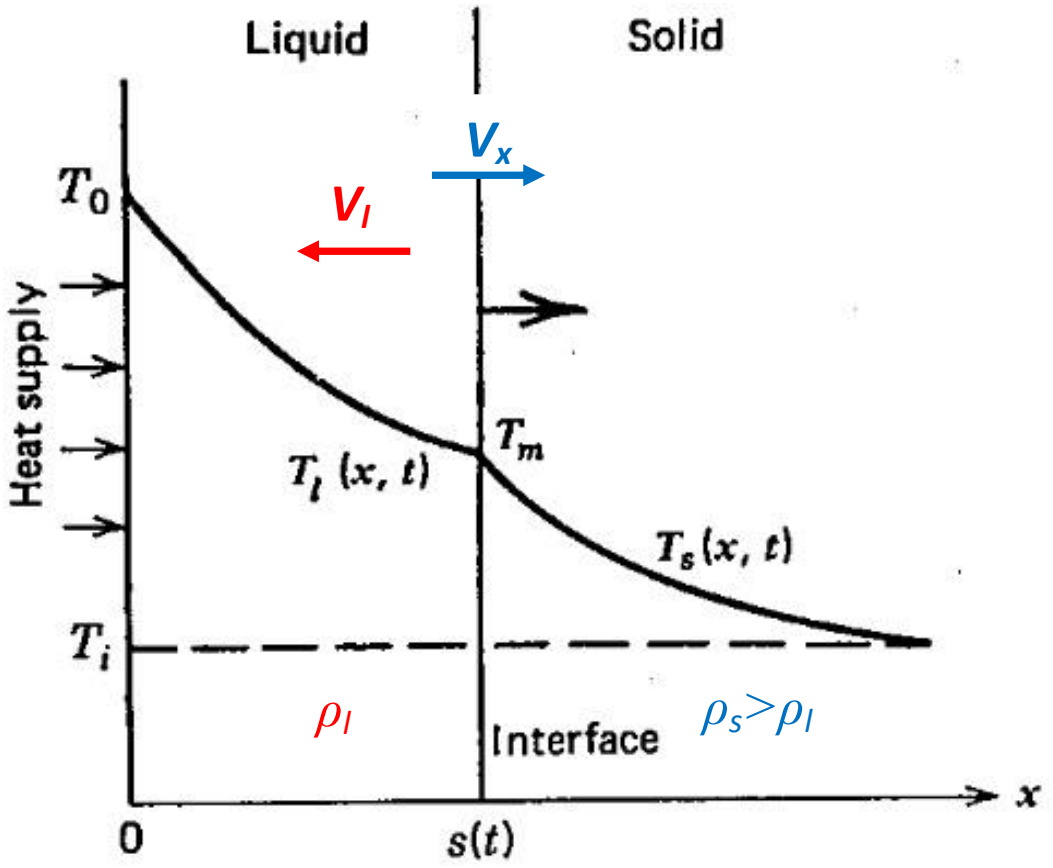

Figure A.3 Schematic diagram of the geometry for 1-D melting problem (Özişik, 1993)

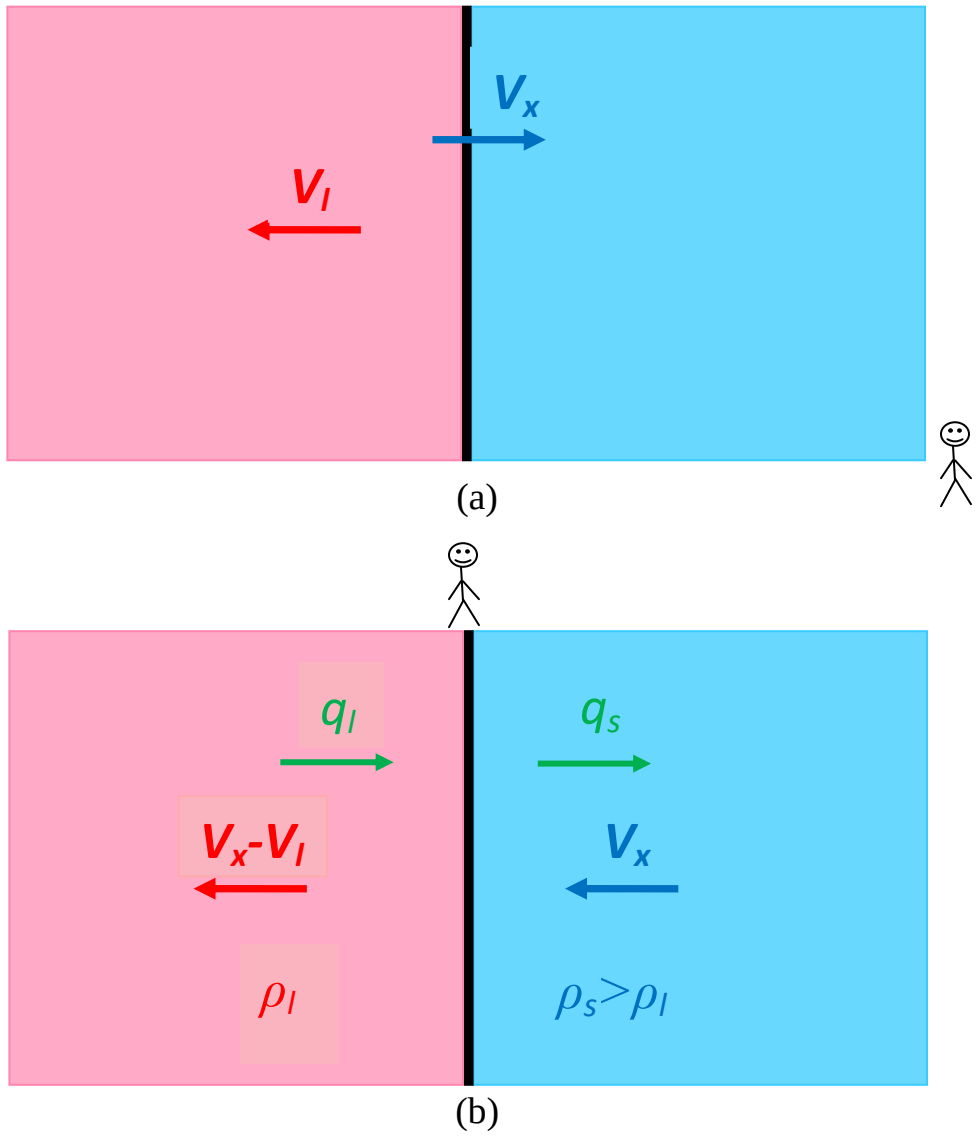

Figure A.4 (a) Melting as viewed by an observer positioned at x=const. showing the interface moving to the right into the solid phase and (b) the steady-state version of the problem viewed by an observer that is riding with the interface

Appendix B Formulation of A Two-Phase Melting Limiting Case Problem Analogous to the Operation of the Transient Hot Wire Method

In this appendix, the problem formulation and its exact solution for melting of an infinite domain that contains a zero-thickness heated wire is presented. The notations match Özişik (1993) who reported the reverse solidification (freezing) problem. The melting problem, which is presented here, was originally proposed and solved by Paterson (1952) using different mathematical notations.

Melting of an infinite medium with cylindrical symmetry is due to a zero-thickness line heat source of strength $Q, \frac{W}{m}$ located at $r = 0$. The geometry of the problem is shown in Figure B.1. The infinite solid block is initially at temperature T_i lower than the melting temperature of the medium (T_m). The heat source is turned on at $t = 0$ and continuously releases heat for $t > 0$. Consequently, melting starts at $r = 0$ and the liquid-solid interface moves in the r-direction, with $s(t)$ standing for the instantaneous position of the liquid-solid interface as a function of time. Using subscripts *l* and *s* to denote the liquid and solid phases, respectively, and assuming identical densities for the two phases, the energy equation governing conduction of heat within the liquid layer (valid for $0 < r < s(\mathrm{t}) \quad and \quad \mathrm{t} > 0$) is:

$$\frac{1}{r}\frac{\partial}{\partial r}\left(r\frac{\partial T_l}{\partial r}\right) = \frac{1}{\alpha_l}\frac{\partial T_l(r,t)}{\partial t}, \tag{B.1}$$

whereas for the solid phase ($s(t) < r < \infty \;\; and \;\; \mathrm{t} > 0$),

$$\frac{1}{r}\frac{\partial}{\partial r}\left(r\frac{\partial T_s}{\partial r}\right) = \frac{1}{\alpha_s}\frac{\partial T_s(r,t)}{\partial t}, \tag{B.2}$$

At the liquid/solid interface, $r = s(t) \;\; and \;\; t > 0$,

$$T_s(r,t) = T_l(r,t) = T_m \, , \tag{B.3}$$

$$k_s \frac{\partial T_s}{\partial r} - k_l \frac{\partial T_l}{\partial r} = \rho L \frac{ds(t)}{dt} \; . \tag{B.4}$$

Relation (B.4) matches relation (A.15) subject to the densities of the two phases being identical in this Appendix.

The initial and boundary conditions are as follows:

For $t = 0$ at $r > 0$, $\qquad T_s(r,t) = T_i$ (B.5)

For $r \to \infty$ and $t > 0$, $\qquad T_s(r,t) \to T_i$ (B.6)

Paterson (1952) proposed the solutions to the temperatures for the liquid and solid domains as follow:

$$T_l(r,t) = A - BEi\left(\frac{-r^2}{4\alpha_l t}\right), \qquad \text{for} \qquad 0 < r < s(\mathrm{t}) \tag{B.7}$$

$$T_s(r,t) = T_i - CEi\left(\frac{-r^2}{4\alpha_s t}\right), \qquad \text{for} \qquad s(t) < r < \infty \tag{B.8}$$

where the exponential-integral function is defined as (Abramowitz and Stegun, 1965):

$$-Ei(-x) \equiv E_1(x) = \int_x^\infty \frac{e^{-u}}{u}du = \int_1^\infty \frac{e^{-xt}}{t}dt \qquad \text{for} \qquad x > 0. \tag{B.9}$$

The partial derivates of equations (B.7) and (B.8) with respect to r take the form:

$$\frac{\partial T_l(r,t)}{\partial r} = -\frac{2B}{r} e^{-r^2/4\alpha_l t} \,, \tag{B.10}$$

$$\frac{\partial T_s(r,t)}{\partial r} = -\frac{2C}{r} e^{-r^2/4\alpha_s t} \,. \tag{B.11}$$

The solution (B.7) satisfies equation (B.1) for the liquid phase and solution (B.8) satisfies equation (B.2) for the solid domain. The energy balance equation around the heat source is of the form:

$$\lim_{r\to 0} \left[-2\pi r k_l \frac{\partial T_l}{\partial r}\right] = Q \,. \tag{B.12}$$

By replacing equation (B.10) into equation (B.12), we obtain

$$B = +\frac{Q}{4\pi k_l} \,. \tag{B.13}$$

Introducing equations (B.7), (B.8), and (B.13) into equation (B.3),

$$A - \frac{Q}{4\pi k_l} Ei(-\lambda^2) = T_i - CEi\left(\frac{-\lambda^2 \alpha_l}{\alpha_s}\right) = T_m \,, \tag{B.14}$$

where λ is a positive constant which is defined as:

$$\lambda = \frac{s(t)}{2(\alpha_l t)^{1/2}} \,. \tag{B.15}$$

By solving equation (B.14), the coefficients A and C are found as:

$$A = T_m + \frac{Q}{4\pi k_l} Ei(-\lambda^2) \,, \tag{B.16}$$

$$C = \frac{T_i - T_m}{Ei(-\lambda^2 \alpha_l/\alpha_s)} \,. \tag{B.17}$$

Using equation (B.15), the derivative of $s(t)$ takes the form:

$$\frac{ds(t)}{dt} = \frac{2\alpha_l \lambda^2}{s}\,. \tag{B.18}$$

By introducing equations (B.16) and (B.17) into equations (B.7) and (B.8), the solutions for the temperature distributions within the liquid and solid domains are:

$$T_l(r,t) = T_m + \frac{Q}{4\pi k_l}\left[-Ei\left(-\frac{r^2}{4\alpha_l t}\right) + Ei(-\lambda^2)\right] \quad \text{for} \quad 0 < r < s(t), \tag{B.19}$$

$$T_s(r,t) = T_i - \frac{T_i - T_m}{Ei(-\lambda^2\alpha_l/\alpha_s)}\,Ei\left(-\frac{r^2}{4\alpha_s t}\right) \quad \text{for} \quad s(t) < r < \infty. \tag{B.20}$$

The location of the liquid/solid interface will be determined through:

$$s(t) = 2\lambda(\alpha_l t)^{1/2} \tag{B.21}$$

where λ needs to be calculated by solving the following transcendental equation:

$$\frac{Q}{4\pi}e^{-\lambda^2} + \frac{k_s(T_m - T_i)}{Ei(-\lambda^2\alpha_l/\alpha_s)}e^{-\lambda^2\alpha_l/\alpha_s} = \lambda^2\alpha_l\rho L \tag{B.22}$$

Once λ is obtained, the location of the liquid/solid interface can easily be tracked versus time using equation (B.21). Furthermore, the temperature distributions for both liquid and solid regions will also be known through equations (B.19) and (B.20).

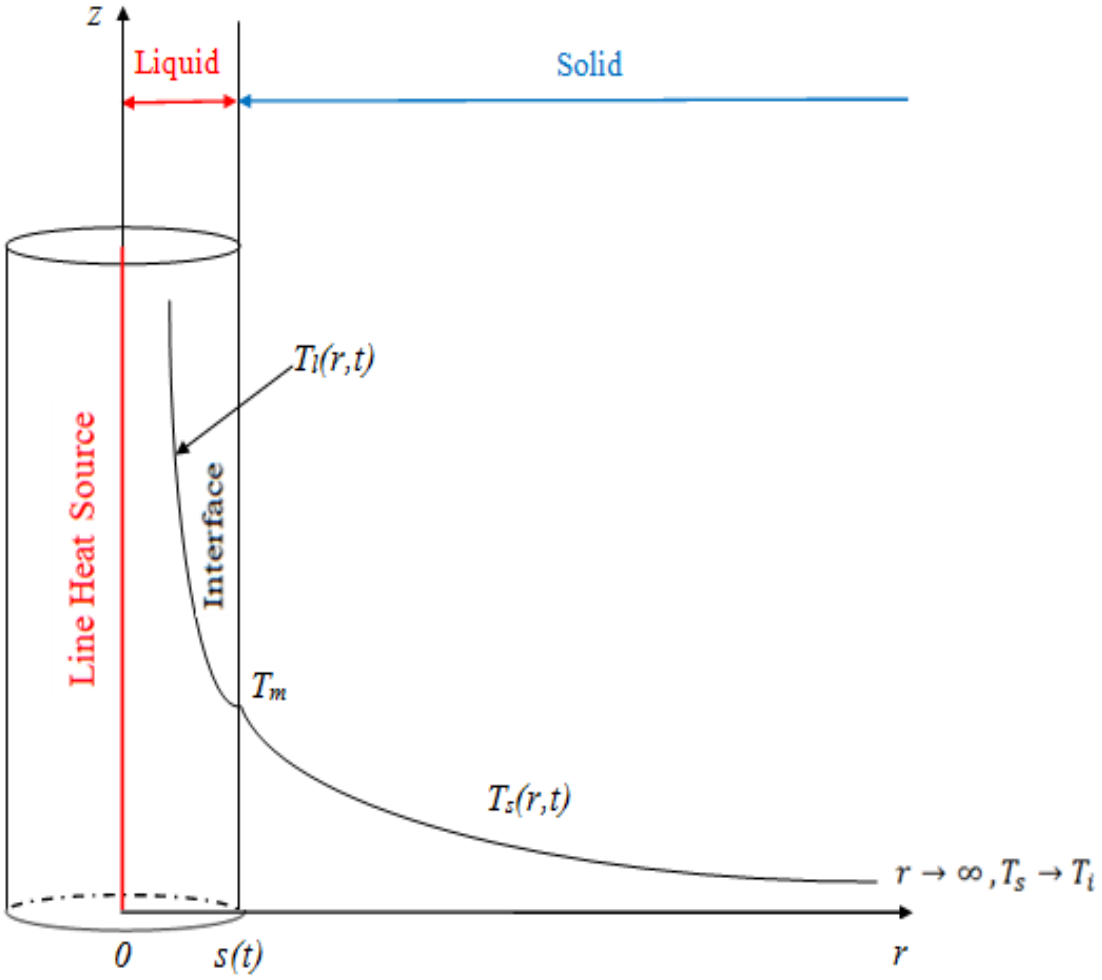

Figure B.1 Schematic figure of melting of an infinite medium with a zero-thickness line heat source positioned along the symmetry axis (r=0)

Appendix C MATLAB Code for Numerical Root-Finding Algorithm

Using the MATLAB software and based on the Newton-Raphson root-finding algorithm, a numerical routine was developed and coded to in order to solve for λ in equation (4.14). The properties specified in section (4.5.2) and Table 4.1 are used for the specific case of eicosane ($C_{20}H_{42}$) as the selected PCM in this study.

```
% Eicosane (C20H42) is selected as the PCM
% Thermal properties:
clc
close all
kl=0.148; ks=0.42;          % Thermal conductivity of fluid
[W/mK]
kw=71.7;                    % Thermal conductivity of wire
[W/mK]
r=840;                      % Density [kg/m^3]
cl=2460; cs=1920;           % Constant pressure specific heat
[J/kgK]
al=kl/r/cl; as=ks/r/cs;     % Thermal diffusivity [m^2/s]
Tf=310;                     % Freezing temperature [K]
L=247000;                   % Latent heat of fusion [J/kg]
q=1;                        % Line heat sink generated power
[W/m]

% Initial and boundary conditions:
```

```
Ti=309.9;          % Initial temperature [K]
T0=309.9;          % Temperature condition at outer boundary [K]
b=0.005992;        % Length of the PCM domain [m]

% Dimensionless parameters:
A=as/al;                    % Dimensionless thermal diffusivity
S=(cs.*q)./(kw.*L);         % Stefan number
laml=[-0.2:0.0001:0.5];     % Initialize the lambda

% To find an approximate guess for lambda:
y=eq444(laml,ks,Ti,Tf,A,al,r,L);
subplot(2,2,1)
plot(laml,y,'b','Linewidth',2)
axis([-0.2 0.5 -4 0.5])
xlabel('\lambda');ylabel('Transcendental Function Value');
title('Plot of Transcendental Function vs. \lambda');
grid on;

% Newton-Raphson root finding method:
lam=[];
lam=input('Please specify an initial guess for lambda:\n');
nmax=1000; tole=0.00000001; dx=0.00000001;
format long

% The previous section was set to get a proper initial value for
% lambda in order to avoid divergence
for i=1:nmax
    lam(i+1)=lam(i)-
2*dx.*eq444(lam(i),ks,Ti,Tf,A,al,r,L)./(eq444((lam(i)+dx),ks,Ti,
Tf,A,al,r,L)-eq444((lam(i)-dx),ks,Ti,Tf,A,al,r,L));
    if abs(lam(i+1)-lam(i))<tole; break; end
end
```

```
fprintf('The exact value for lambda is equal to %
f.\n',lam(i+1))
lambda=lam(i+1);                  % The exact solution of lambda

% Plotting the interface position function s(t):
tmax=(b.^2)./(al.*(4.*(lambda.^2)));       % Total time [sec] by
which the interface will reach the other boundary
tp=[0:1:tmax];
tm=tmax./60;
t=[0:50:tmax];
st=2.*lambda.*sqrt(al.*t);
subplot(2,2,2)
plot(t,st,'b','LineWidth',2)
xlabel('Time [sec]');
ylabel('Interface Position S(t) [m]');
title('Plot of interface position vs. time');
grid on;
[st1,st1]=meshgrid(st);
st=st1;

% The temperature profiles in both solid and liquid domains
x1=[0:b/456:b];
t1=[0:tmax/456:tmax];
[x1,t1]=meshgrid (x1,t1);
i=1;
for i=1:457
    for j=1:457
    ste=st(i,j);
    x11=x1(i,j);
    t11=t1(i,j);
    if (x11>=0)&&(x11<=ste)
```

```
T(i,j)=Tf+((q./(4.*pi.*kl)).*((expint((x11.^2)./(4.*al.*t11))-
expint(lambda.^2))));
    elseif (x11>=ste)
    T(i,j)=Ti-(((Ti-Tf)./(-expint((lambda.^2).*(1./A)))).*(-
expint((x11.^2)./(4.*as.*t11))));
    end
    end
end

for i=1:457
    for j=1:457
        ste2(i,j)=st(i,j);
        T4(i,j)=310;
   end
end

subplot(2,2,3)
mesh(x1,t1,T)
xlabel('r [m]'); ylabel('Time [sec]');
zlabel('Temperature [K]');
title('Contour of temperature in both solid/liquid domains
vs.(r,t)');
axis([0 b 0 tmax 307 317])
grid on;
hold on;
plot3(ste2,t1,T4,'k','Linewidth',1.5)

% The temperature profile at the wire interface
x2=linspace(0.000002,0.000002,457);
t2=linspace(0,1,457);
[x2,t2]=meshgrid (x2,t2);
```

```
i=1;
for i=1:457
for j=1:457
    ste=st(i,j);
    x22=x2(i,j);
    t22=t2(i,j);
    if (x22>=0)&&(x22<=ste)

T2(i,j)=Tf+((q./(4.*pi.*kl)).*((expint((x22.^2)./(4.*al.*t22))-
expint(lambda.^2))));
    elseif (x22>=ste)
    T2(i,j)=Ti-(((Ti-Tf)./(-expint((lambda.^2).*(1./A)))).*(-
expint((x22.^2)./(4.*as.*t22))));
    end
   end
end

x3=linspace(0.0000025,0.0000025,457);
t2=linspace(0,1,457);
[x3,t2]=meshgrid (x3,t2);
i=1;
for i=1:457
for j=1:457
    ste=st(i,j);
    x33=x3(i,j);
    t22=t2(i,j);
    if (x33>=0)&&(x33<=ste)

T8(i,j)=Tf+((q./(4.*pi.*kl)).*((expint((x33.^2)./(4.*al.*t22))-
expint(lambda.^2))));
    elseif (x33>=ste)
```

```
    T8(i,j)=Ti-(((Ti-Tf)./(-expint((lambda.^2).*(1./A)))).*(-
expint((x33.^2)./(4.*as.*t22))));
    end
   end
end

x4=linspace(0.000003,0.000003,457);
t2=linspace(0,1,457);
[x4,t2]=meshgrid (x4,t2);
i=1;
for i=1:457
for j=1:457
    ste=st(i,j);
    x44=x4(i,j);
    t22=t2(i,j);
    if (x44>=0)&&(x44<=ste)

T9(i,j)=Tf+((q./(4.*pi.*kl)).*((expint((x44.^2)./(4.*al.*t22))-
expint(lambda.^2))));
    elseif (x44>=ste)
    T9(i,j)=Ti-(((Ti-Tf)./(-expint((lambda.^2).*(1./A)))).*(-
expint((x44.^2)./(4.*as.*t22))));
    end
   end
end
T7=xlsread('matlab.xlsx','G1:G457');
subplot(2,2,4)
plot(t2,T2,'b',t2,T7,'r',t2,T8,'m',t2,T9,'g','LineWidth',1.5)
axis([0,1,309,314])
xlabel('Time [sec]');
ylabel('Temperature [K]');
title('Plot of temperature profile at the interface vs. time');
```

```
grid on;

% The position of the rectangle
xt = 0.9; yt = 313; wt =0.1; ht = 0.5;
rectangle('Position', [xt-wt/2, yt-ht/2, wt, ht], ...
          'EdgeColor', [0.4, 0.1, 0.4]);
% The position of the axis
xq = 0.78; yq = 0.18; wq = 0.1; hq = 0.1;
ax = axes('Units', 'Normalized', ...
          'Position', [xq, yq, wq, hq], ...
          'XTick', [], ...
          'YTick', [], ...
          'Box', 'on', ...
          'LineWidth', 2, ...
          'Color', [1, 1, 1]);
hold on;
plot(t2,T2,'b',t2,T7,'r',t2,T8,'g',t2,T9,'m');
axis([xt-wt/2, xt+wt/2, yt-ht/2, yt+ht/2]);
```

The subroutine function “eq444” which is called in the main code, is defined as:

```
% y returns the function value and x stands for lambda
% k1=ks, k2=Ti, k3=Tf, k4=A, k5=al, k6=r, k7=L
function y=eq444(x,k1,k2,k3,k4,k5,k6,k7)
y=((1./(4.*pi))*(exp(-x.^2)))+((((((k1).*(k3-k2))./(-
expint((x.^2).*(1./k4)))).*((exp(-x.^2)).*(1./k4))))-
((x.^2).*k5.*k6.*k7);
```